ESTIMATING THE ALTITUDES OF CLOUDS AT THE MARS SCIENCE LABORATORY LANDING SITE

CHARISSA L. CAMPBELL

A THESIS SUBMITTED TO
THE FACULTY OF GRADUATE STUDIES
IN PARTIAL FULFILMENT OF THE REQUIREMENTS
FOR THE DEGREE OF

MASTER OF SCIENCE

GRADUATE PROGRAM IN PHYSICS & ASTRONOMY
YORK UNIVERSITY
TORONTO, ONTARIO

October 2018

Abstract

Using the Navigation Camera, the Mars Science Laboratory (Curiosity) Rover images the atmosphere to capture clouds. A Zenith Movie (ZM) consists of eight upward-pointing images taken over five minutes. The angular distance and wind direction are measurable, but without a lidar the altitude is not. Instead, parameters are compared with results modelled by the Mars Regional Atmospheric Modelling System (MRAMS). An altitude is estimated with the half-normal probability distribution to evaluate the probability MRAMS has similar conditions to observational values.

Throughout a sol, clouds were predicted below the crater rim and planetary boundary layer, but higher altitude clouds were primarily predicted in the morning. Results are compared to ice extinction data from the Mars Climate Sounder (MCS) and shadow movement across Aeolis Mons through a Cloud Height Movie (CHM). Pairing a ZM with a CHM allows direct measurement of the altitude of clouds for the first time from the surface.

Table of Contents

List of Tables

List of Figures

1 Introduction

For the past few decades, the Martian atmosphere has been a topic of study for both planetary and atmospheric scientists. Its atmosphere is composed of 95% CO_2, 2.7% N_2 and 1.6% O_2 and has a varying surface pressure between 4.0 and 8.7 mb depending on season and geographical location (Williams, 2016). At the mean radius of 3389.5 km, the pressure is 6.36 mb; equivalent to 0.6% of Earth's surface pressure (Williams, 2016). The obliquity and rotational period are 25.2° and 24.66 hours respectively (Williams, 2016). A Martian day is known as a sol and is only 39 minutes longer than a day on Earth. A Martian Year (MY) corresponds to 686.98 sols, which is equivalent to 1.88 Earth years (Williams, 2016). The first MY started April 11, 1955 where the current MY is 34 (Clancy et al., 2000).

Having a similar obliquity as Earth, Mars exhibits seasonal behaviour throughout its orbit. Another factor affecting the seasonal variation is the eccentricity (ε). With $\varepsilon = 0.09$, Mars's eccentricity is the second highest in our solar system, after Mercury (Williams, 2016). This is 5.6 times higher than Earth's eccentricity. The eccentricity controls the aphelion and perihelion points of the orbit. Aphelion is the furthest orbital point from the Sun while perihelion is the closest, ranging 1.66 AU to 1.38 AU respectively for Mars. This significant range in orbital distance allows a wider variation in temperatures. These seasons can be described by solar longitude (L_s). Solar longitude outlines Mars' orbit with respect to the equator and Sun. Shown in Figure 1.1, L_s is measured in degrees and starts at the vernal equinox. The seasons on Mars correspond to $L_s = 0°$ (Northern spring/Southern fall), $L_s = 90°$ (Northern summer/Southern winter), $L_s = 180°$ (Northern fall/Southern spring), and $L_s = 270°$ (Northern winter/Southern summer). In terms of orbit, aphelion occurs at $L_s = 71°$ and perihelion at $L_s = 251°$.

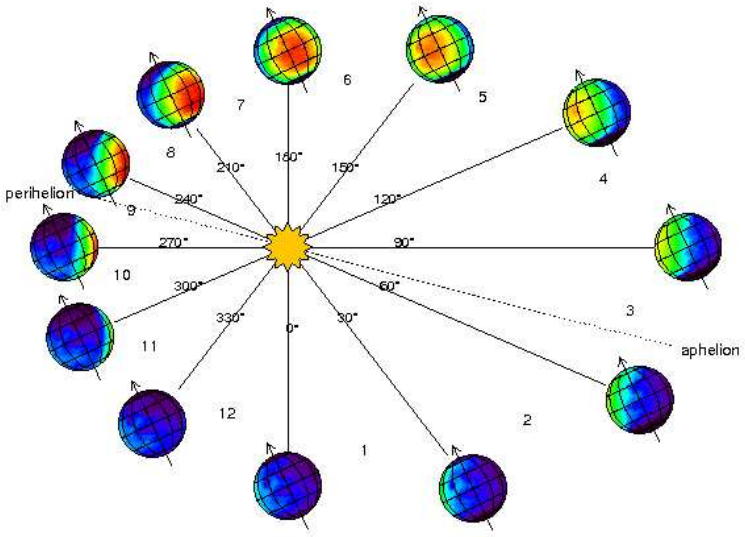

Figure 1.1: Diagram describing the solar longitude L_s (Laboratoire de Meteorologie Dynamique, 2008). A MY consists of 12 Martian months that span 30° individually for a total of 360°. The difference between aphelion and perihelion from the highly elliptical orbit is also evident.

1.1 Martian Water-Ice Clouds

Water-ice clouds have been viewed from both the surface and orbit for the past few decades. Smith and Smith (1972) used telescopic blue light photographs and observations from Mariner 6 and 7 to classify two types of seasonal varying "white clouds". Type I clouds peak in northern mid-summer while Type II peak in northern mid-winter (Smith and Smith, 1972). Additionally, Type I clouds showed a diurnal cycle with peaks in late morning and early afternoon while Type II showed no diurnal trend over the course of a sol (Smith and Smith, 1972). The diurnal cycle of Type I indicate their composition of water-ice and Type II are more likely to be composed with CO_2 (Smith and Smith, 1972). Peale (1973) suggested that Martian clouds were formed from the circulation of water between the surface and atmosphere, especially around high-elevated areas. Orographic clouds form near high-elevated surface features such as mountains or volcanoes. Discussed by (Sagan et al., 1971), Martian clouds that form at high-elevated areas could be caused by orographic winds. Cloud activity at high-elevated areas was confirmed by Pearl et al. (2001) through TES

observations. Opacities ranged up to 0.6 and clouds showed possible wave structure, indicating orographic winds (Pearl et al., 2001). Pearl et al. (2001) also confirmed two Martian seasons, aphelion showing clouds and perihelion showing major dust storms.

The Aphelion Cloud Belt (ACB) describes the equatorial clouds that form every MY during the aphelion season. Clancy et al. (1996) first noticed correlations between visual Hubble images, National Radio Astronomy Observatory (NRAO) millimeter-wave microwave CO spectra and Viking temperature measurements during the aphelion season. These images showed a belt of clouds covering 10°S-30°N with opacities ranging from 0.2-0.6 (Clancy et al., 1996). This annual feature is consistent with Mars's highly elliptical orbit that causes atmospheric temperatures between 0-60 km to fluctuate by 20 K between aphelion and perihelion (Clancy et al., 1996). In terms of solar longitude, the ACB occurs every Mars year starting around L_s 45° and ending around L_s 150°. The origin of this cloud belt comes from the condensation of water vapor through Hadley circulation (Clancy et al., 1996). Similar to Earth, Mars exhibits two Hadley cells, one in each hemisphere along the equator Haberle (1986). Hadley cells are responsible for the circulation of warmer air from the equator towards the poles. This air cools, falls to the ground and returns to the tropics. Easterly winds are caused by the Coriolis force deflecting air from the Hadley cell (Haberle, 1986). Between the aphelion and perihelion sesason, Haberle et al. (1993) noticed a twofold difference in Hadley cell intensity in Ames General Circulation Model simulations. At solstices, a single cross-equatorial Hadley cell existed, while at equinoxes there were two symmetric Hadley cells in each hemisphere (Haberle et al., 1993). An example of Hadley cells on Mars is shown in Figure 1.2. The ACB season was also seen by Wolff et al. (1999) through HST images and Pathfinder, confirming results from Clancy et al. (1996).

It was widely believed that Martian water-ice clouds were not important to the global transport of water due to the low water column abundance measured by Jakosky and Farmer (1982). Using the Mars Atmospheric Water Detectors (MAWD) on the Viking orbiter, the water vapour column abundance varied between 0 and 100 precipitable microns (Jakosky and Farmer, 1982). This indicates that if all of the water on the atmosphere was to condense onto the surface covering the entire planet, it would be 100 microns thick. Even with low water column abundance, Clancy et al. (1996) argue that low-altitude clouds during

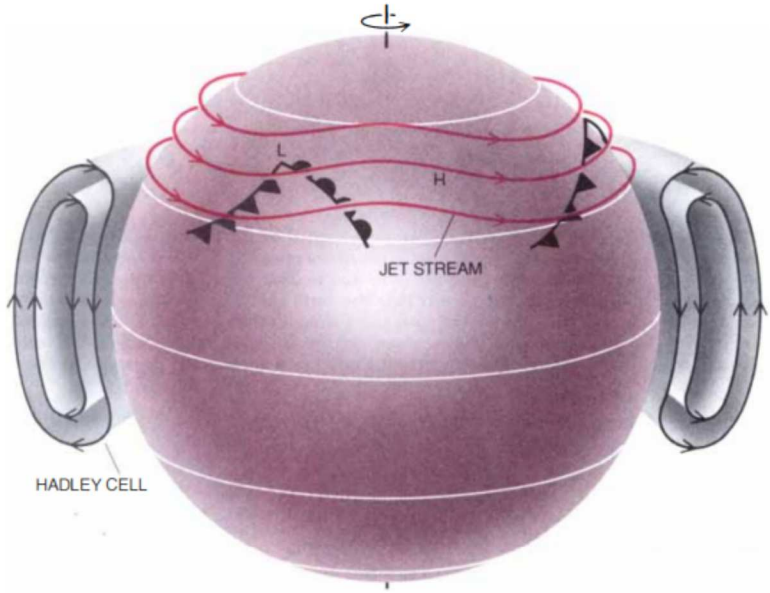

Figure 1.2: Hadley circulation during the Northern winter (Haberle, 1986). The two Hadley cells that existed in Northern fall became a cross-equatorial Hadley cell because of more pronounced winds during seasonal changes (Haberle, 1986). Haberle (1986) argue jets through the Hadley cell are stronger at solstices because of the larger temperature gradient.

aphelion play a bigger part in transportation of water with Hadley cells. Jakosky and Farmer (1982) showed an asymmetry in water-vapour between the north and south hemisphere, where the northern hemisphere contained up to twice as much vapour. The ACB could be the explanation of water movement from the north to south as argued by Clancy et al. (1996) and seen by Smith (2004) in results from the Thermal Emission Spectrometer (TES) on the Mars Global Surveyor (MGS).

Thermal infrared spectra was measured by TES to understand atmospheric thermal structure, optical depth of dust and water-ice and water vapour column abundance (Smith, 2004). Data received by MGS showed repeated annual patterns, with two distinct seasons. During perihelion (L_s 180°-360°), Mars is relatively warm with dusty conditions while during aphelion (L_s 0°-180°) Mars is cooler, free of dust and shows clouds (Smith, 2004). Infrared spectra also showed water vapour moving from the north to the south pole during the aphelion season (Smith, 2004), confirming Clancy et al. (1996). Figure 1.3 shows the daytime

aerosol optical depth and water vapour column over a period of two MYs.

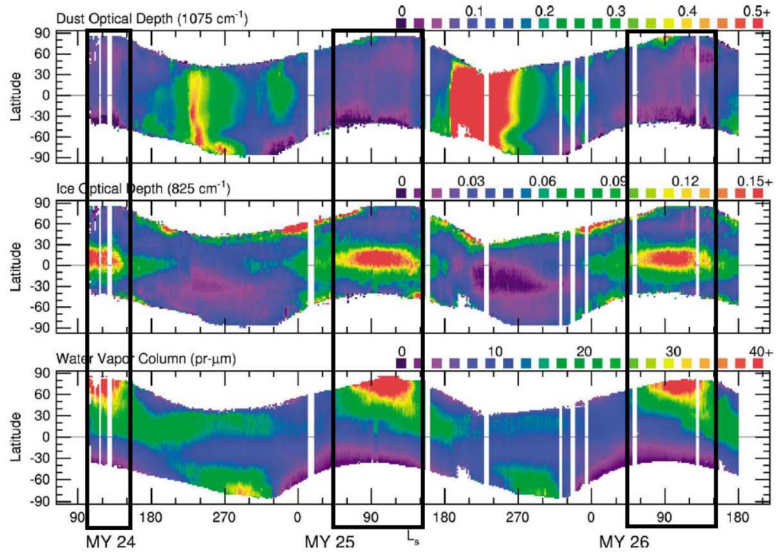

Figure 1.3: Aerosol optical depth and water vapor abundance as measured by TES at 14:00 local time shown as a function of latitude and season (Smith, 2004). Aphelion is shown in the black box. Dust optical depth (top) is at its lowest while both ice optical depth (middle) is at its peak. Water vapour column (bottom) shows a peak at the north pole and migrates to the south pole between L_s 90° and 270°. Clancy et al. (1996) argue that this migration is from the ACB.

Several aspects compose the atmospheric structure of Mars, including temperature and pressure. In general, Mars does not have a stratosphere due to no ozone layer or other strong absorbers in the atmosphere (Smith et al., 2017). Shown in Figure 1.4, the atmosphere of Mars is represented by three sections: lower, middle and upper.

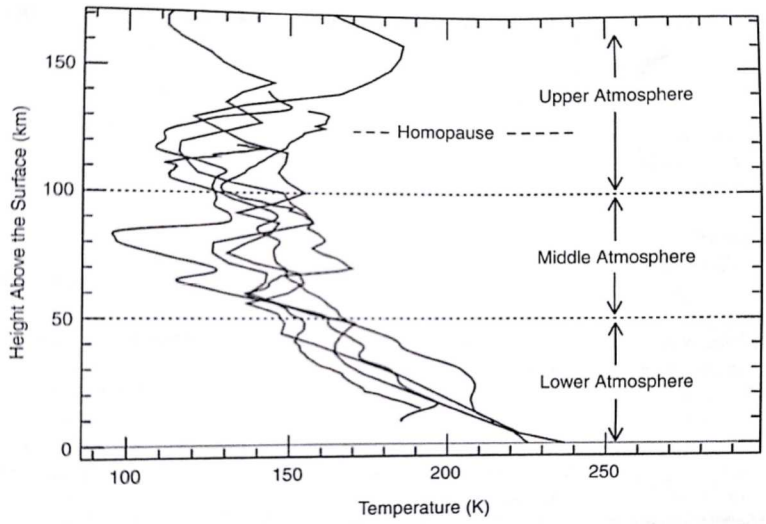

Figure 1.4: Mars atmospheric thermal structure that defines the lower, middle and upper part of the atmosphere. These temperature profiles are calculated from accelerometer observations of landed spacecraft (Smith et al., 2017).

The lower atmosphere is defined below 50 km (2 Pa) where temperatures decrease with height (Smith et al., 2017). The middle atmosphere is located between 50 km and 100 km where temperature is heavily dependent on thermal tides (Smith et al., 2017). Lastly, the upper atmosphere is located above 100 km. At this level, temperatures increase with height due to absorption of solar UV (Smith et al., 2017). Figure 1.5 is an example of atmospheric profiles from accelerometer observations of surface spacecraft as they landed. This figure also shows a closer look at the low and middle atmosphere.

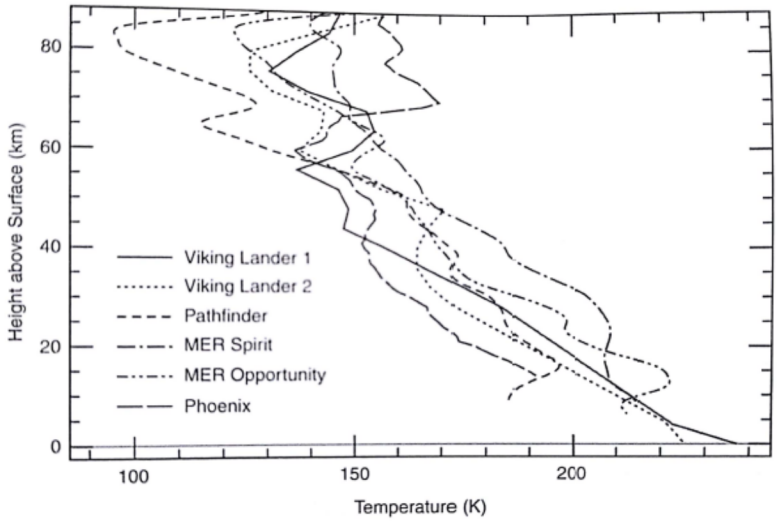

Figure 1.5: Inferred from landed spacecraft as they travelled through the atmosphere, these temperature profiles show the lower to middle Martian atmosphere (Smith et al., 2017). A legend indicates which lander/rover measured which temperature profile.

Other examples for retrieving atmospheric temperature profiles include nadir or limb viewing orbiting spacecraft or radio and stellar occultation observations. For orbiting spacecraft, the temperature can be retrieved using the CO2 molecule strong absorption band for the Martian atmosphere (Smith et al., 2017). Occultation measurements occur when a signal passes through the atmosphere as the object passes behind Mars. While a spacecraft passes behind Mars, sending a radio signal through the limb atmosphere produces a doppler shift. This doppler shift provides frequency which can be converted to temperature (Smith et al.,

2017). Stellar occultation uses a similar technique but with a star passing behind the limb.

Clouds form from water-ice condensing on dust grains in the air, effectively removing the dust (Clancy et al., 1996). This removal causes cooling in the atmosphere allowing water vapour saturation to appear at lower altitudes in the atmosphere, revealing clouds (Wolff et al., 1999). Supersaturation is explored as a cause of water-ice clouds in the Martian atmosphere. Maltagliati et al. (2011) argue that supersaturation exists on Mars when there is an insufficient quantity of Cloud Condensing Nuclei (CCN), such as dust, in the atmosphere for the water-ice to condense on. To measure supersaturation on Mars, the Spectroscopy for Investigation of Characteristics of the Atmosphere of Mars (SPICAM) instrument on Mars Express measured water vapour profiles through solar occultation observations (Maltagliati et al., 2011). Maltagliati et al. (2011) divided the water vapour partial pressure by the phase equilibrium pressure provided through the Goff-Gratch equation to find saturation ratio. Figure 1.6 shows the saturation ratio for all orbits during the aphelion season (Maltagliati et al., 2011).

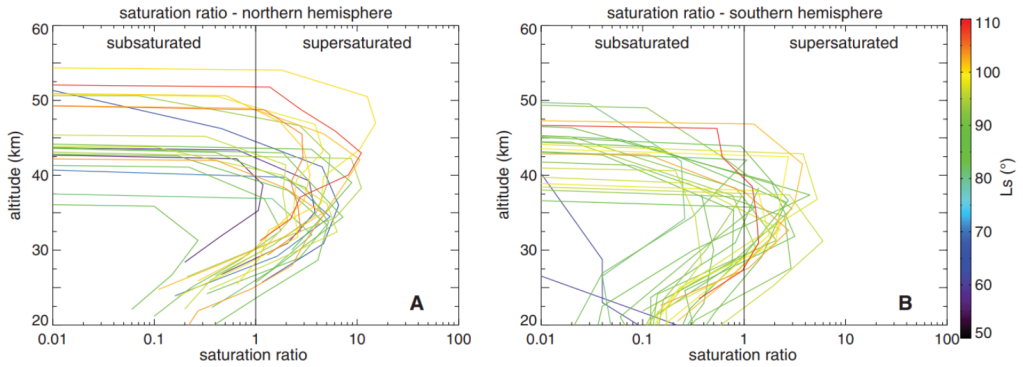

Figure 1.6: Saturation values calculated for orbits from SPICAM (Maltagliati et al., 2011). A saturation ratio of 1 (black vertical line) is the saturated state when water vapour becomes clouds (Maltagliati et al., 2011). The northern hemisphere (left) showed higher supersaturation, in some cases hitting 10. The southern hemisphere (right) showed less, indicating a drier hemisphere.

During the ACB season, Martian water-ice clouds also exhibit diurnal patterns. The Mars Orbiter Camera (MOC) on MGS provides low-resolution maps of the entire surface daily which shows diurnal cloud patterns

Table 1.1: Cloud heights calculated by Benson et al. (2003) for five Martian volcanoes. Observations were made in the afternoon, between 13:00-15:00 local time (Benson et al., 2003).

Surface Feature	L_s	**Cloud top height (km)**
Olympus Mons	54°-147°	19.0-21.0
Ascaeus Mons	50°-143°	15.0-18.0
Pavonis Mons	72°-181°	12.0-14.0
Arsia Mons	83°-182°	16.0-17.4
Alba Patera	47°-138°	5.5-6.5

around high topographical locations such as Olympus Mons (Benson et al., 2003). Orographic clouds were present in this region because of the highly elevated surface features (Benson et al., 2003). Between L_s 110° and 205° clouds were found to intensify as the day progressed and peaked in mid to late afternoon (Benson et al., 2003). Tamppari et al. (2003) used Viking data to discover a diurnal pattern of decreasing extent from morning to midday and an increase from midday to afternoon. This increased extent of clouds in the afternoon is attributed to uplifting dust from hotter midday temperatures, acting as CCN (Tamppari et al., 2003). Clouds were also seen at all times of a sol at high topographic features, as seen by Benson et al. (2003). Wang and Ingersoll (2002) also confirmed through MOC measurements the general behaviour seen through Viking data by Tamppari et al. (2003).

Benson et al. (2003) also used data from the Mars Orbiter Laser Altitumeter (MOLA) on MGS to determine the altitude of clouds above five Martian volcanoes. Altitudes were determined by finding the highest point of contact between the cloud and volcano in contour MOLA maps (Benson et al., 2003). Results for the five volcanoes are shown in Table 1.1. Higher altitudes peaked in the afternoon where cloud height varied 1-2 km in altitude depending on local time (Benson et al., 2003).

From the surface, several rovers have captured water-ice clouds during the ACB season. Opportunity captured images of clouds through regular sky monitoring using the Navigation Camera (Navcam) onboard.

No clouds were detected outside L_s 20°-136°, with peak activity at L_s 50° and 115° (Lemmon et al., 2015). Atmospheric movies taken by the Surface Stereo Imager (SSI) on Phoenix showed cirrus-like clouds and dense, low cumulus-like clouds. Diurnally, clouds at the Phoenix landing site peaked near 10:00 local true solar time (LTST), which Moores et al. (2010) use to argue that the cloud builds overnight with peak optical depth in the early morning and dissipates in the afternoon. Cloud formation at night within the Planetary Boundary Layer (PBL) was detected with lidar and observed the same pattern as Moores et al. (2010) with the clouds dissipating in the afternoon (Whiteway et al., 2009).

Currently, Curiosity searches for clouds at Gale Crater every 2-3 sols using similar atmospheric movies to Phoenix. These movies consist of 8 consecutive images where a Zenith Movie (ZM) is pointed vertically while a Suprahorizon Movie (SHM) is pointed just above the crater rim. Unlike Phoenix, Curiosity uses the Navcam which boasts a 45° × 45° FOV (field of view) versus the SSI 13.8° × 13.8° FOV (Moores et al., 2015b). This increase in FOV allows a larger area of the sky to be viewed, but also hinders timing to minimize exposure from the sun. The difference in latitude between Green Valley (Phoenix) and Gale Crater (Curiosity) as shown in Figure 1.7, means that the sun's path during a sol is higher in the sky at Gale crater. To avoid having the sun within the frames, a ZM cannot be taken within ±2.5 hours from local noon. A SHM does not have this constraint because of its lower elevation angle. Over the course of Curiosity's continued operations, over 400 atmospheric movies have been acquired to characterize their properties, including altitude.

1.2 Observing Martian Water-Ice Clouds from the Surface

In total, there are currently six orbiters and two rovers still continuing operations today (Martínez et al., 2017). The Mars Science Laboratory (MSL, Curiosity) studies geology and atmospheric properties in Gale Crater and is discussed in section 1.3. Opportunity continues to study dust and atmospheric optical depth at Meridiani Planum. Analyzing Martian water-ice clouds from the surface allows a different perspective on water content in the atmosphere. Either through direct imaging or instruments, studying from the surface allows surface processes to be viewed and can verify model parameters. Locations of every spacecraft to the

surface is shown in Figure 1.7.

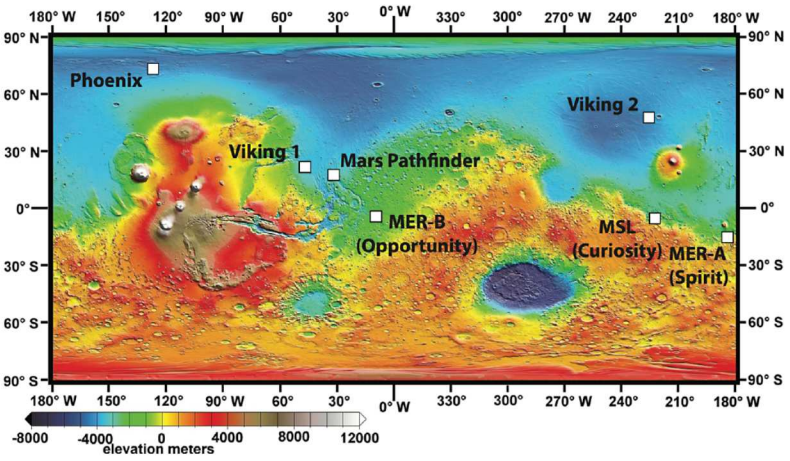

Figure 1.7: Map of Mars with the location of rovers. Includes both previous and current missions, but not future missions (Martínez et al., 2017).

1.2.1 Pathfinder

Landing in 1997, Pathfinder was a base station that included the first rover (Sojourner) to traverse the Martian surface. and help investigate surface properties. with three science instruments. Operating for 3 months, Sojourner navigated 200 m^2 of the surface around the lander studying the local geology and atmosphere (Golombek et al., 1999). The three science instruments onboard Pathfinder included: the Alpha Proton X-ray Spectrometer (APXS) for rock and soil chemical analysis, the Imager for Mars Pathfinder (IMP) for close-up and spectral imaging and the Atmospheric Structures Investigation/Meterology (ASI/MET) for environment monitoring (Golombek et al., 1999). The ASI/MET package measured pressure, temperature and wind velocity from the surface to 160 km (Schofield et al., 1997).

Using the Imager for the Mars Pathfinder (IMP), clouds were seen in images before sunrise, but dissolved rapidly (Schofield et al., 1997). On sol 39, clouds were observed 100 minutes before sunrise, but dissipated by 35 minutes before sunrise (Smith et al., 1997). Figure 1.8 shows sol 39 clouds that are believed to be at an altitude of 10-15 km based on the illumination path of the sun (Lemmon, 2018).

Figure 1.8: Image using the IMP to capture wispy blue clouds on sol 39 (Lemmon, 2018). Taken 40 minutes before sunrise, the bottom clouds are 10° above the horizon and are believed to be 10-15 km about the surface (Lemmon, 2018).

Temperature data taken during entry was used in the Ames Mars General Circulation Model (MGCM) to try to reproduce characteristics of clouds observed at the Pathfinder landing site (Colaprete et al., 1999). When using a diurnal temperature profile, a primary cloud formed between 20-40 km that was present throughout the sol (Colaprete et al., 1999).

Overall, results from Pathfinder showed consistent atmospheric structure and weather, as originally seen by the Viking 1 lander(Schofield et al., 1997). As measured by Pathfinder, differences from Viking 1 lander results include cooler nighttime upper atmosphere temperatures and near-surface atmospheric temperatures being 10-12 K warmer (Schofield et al., 1997).

1.2.2 Mars Exploration Rover (MER)

The Mars Exploration Rover (MER) mission included two twin rovers carrying the Athena science payload used to explore environmental conditions and if water was once present on the surface (Squyres et al., 2003). Landing in 2004 during Southern autumn, MER-A (Spirit) operated for over 2000 sols, while MER-B (Opportunity) is still functional today after 5000 sols (Martínez et al., 2017). They landed on opposite sides of the planet, at Gusev Crater (14.57°S, 175.48°E) and Meridiani Planum (1.95°S, 354.47°E) respectively.

The different instruments are shown in Figure 1.9.

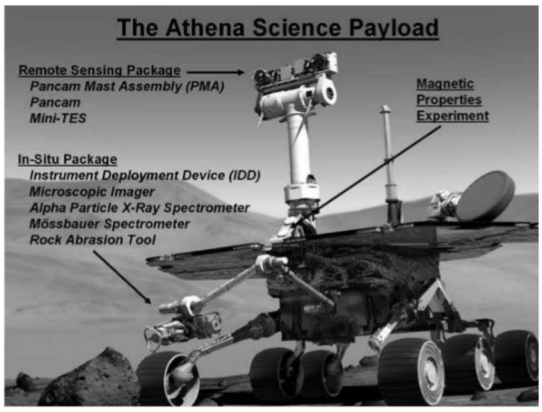

Figure 1.9: Payload for the MER rovers included both a remote sensing and in-situ package to assess conditions environmentally and geologically (Squyres et al., 2003). A magnetic properties experiment was also included that removed any magnetic particles from nearby soil allowing composition to be measured for these magnetic materials (Squyres et al., 2003).

For environmental monitoring, the Miniature Thermal Emission Spectrometer (Mini-TES) and any cameras such as the Panoramic Camera (Pancam) or Navigation Camera (Navcam) are the most useful. Mini-TES is a Fourier Transform IR Spectrometer and is a smaller version of TES onboard MGS (Christensen et al., 2003). Collecting high resolution infrared spectra, scientific goals included constraining mineralogy of rocks/soil and environmental monitoring of temperature, dust and water-ice opacity for the bottom 2 km of the atmosphere (Smith et al., 2006). The Pancam is a multispectral imaging system containing two digital cameras on the mast located 1.5 meters above the surface (Bell et al., 2003). The mast is moveable by 360° azimuth and 90° elevation allowing both ground and sky observations (Bell et al., 2003). The FOV of the Pancam is $16° \times 16°$ with an image size of 1024×1024 pixels (Bell et al., 2003). Unlike the Pancam, the Navcam has a $45° \times 45°$ FOV, allowing a wider range of the atmosphere or surface to be seen (Maki et al., 2003). The Navcam is discussed more in depth in Section 2.1.1.

Mini-TES results from the first MY showed null results for water-ice clouds (Smith et al., 2006). Orbital cloud observations showed a peak optical depth of 0.1 during that aphelion season for both sites, where the

clouds may be too high in the atmosphere to be detected by Mini-TES (Smith et al., 2006). Wolff et al. (2006) argue that TES limb-derived observations show a cloud layer above 35 km, which is too high for Mini-TES to observe. Seeing little water-ice in Mini-TES suggests that clouds exist higher in the atmosphere at both landing sites (Smith et al., 2006).

Another method used to find atmospheric properties with MER was direct imaging of the Sun with the Pancam. These mast-mounted cameras have independent filter wheels including solar filters at 440 and 880 nm (Lemmon et al., 2004). The first 5 MY of the MER mission showed consistent low dust from L_s 0°-135°, equivalent to the ACB season, while larger amounts were present in the other seasons (Lemmon et al., 2015). Water-ice clouds were also seen at the Opportunity site over L_s 20°-136°, but not significantly at Spirit (Lemmon et al., 2015). Figure 1.10 is an example of clouds at Meridiani Planum observed by Opportunity through the Navcam.

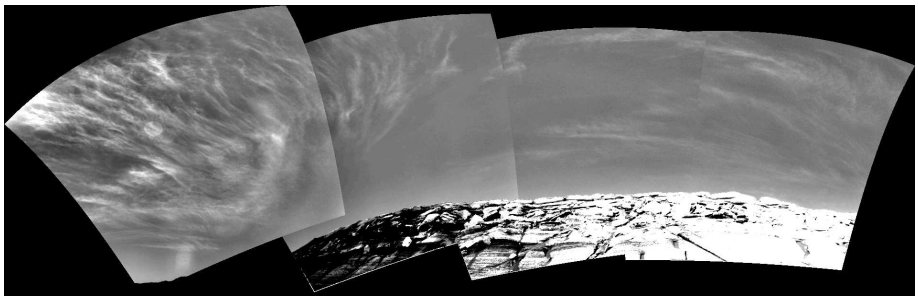

Figure 1.10: Clouds captured through the Navcam on Opportunity on sol 290 at 09:30 (NASA/JPL-Caltech, 2004). An imaging technique was used to pull out the thin clouds in the frames including reducing glare from the sun and geometrical distortion (NASA/JPL-Caltech, 2004).

1.2.3 Phoenix

In 2008, the Phoenix mission landed in the Martian arctic at a site named Green Valley (68°N, 233°E) (Smith et al., 2008). Subsurface water-ice was predicted to exist in the Martian arctic and Phoenix as designed to verify this hypothesis (Smith et al., 2009). Lasting for 151 sols, the mission exceeded the 90 sol life-time. For characterizing clouds, a Light Detection and Ranging (lidar) instrument and the Surface Stereo Imager

(SSI) are used.

The Phoenix lidar instrument emitted pulses of laser light into the atmosphere to detect backscatter from clouds resolving their internal structure (Whiteway et al., 2009). This backscattered light can be recorded as a function of time, which can be converted to distance (Whiteway et al., 2008). The lidar on Phoenix used a 532 nm wavelength pulsed light laser to measure dust and ice at altitudes ranging from 200 m to 20 km (Whiteway et al., 2008). An example of this is shown in Figure 1.11. Peak values of 1 mg/m^3 were observed at 6 am, where cloud formation started around midnight and dissipated before midday (Dickinson et al., 2010). Fall streaks were also observed within the Planetary Boundary Layer (PBL) through backscatter contour plots as seen in Figure 1.12.

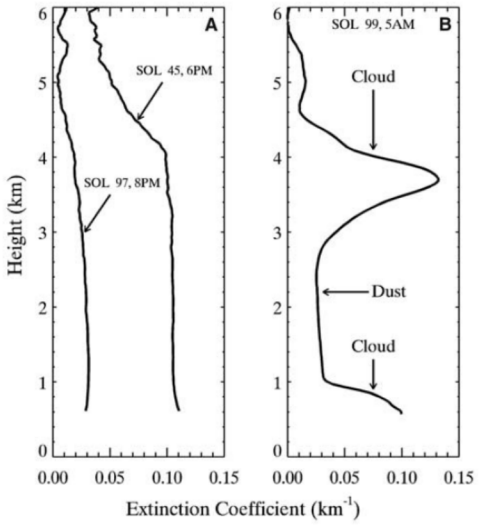

Figure 1.11: Optical extinction coefficients found from lidar backscatter at wavelength 532 nm (Whiteway et al., 2009). Sols 45 (L_s 97°), 97 (L_s 121°) and 99 (L_s 122°) are represented. Clouds can be easily defined by their larger extinction coefficient from the larger particle size compared to dust.

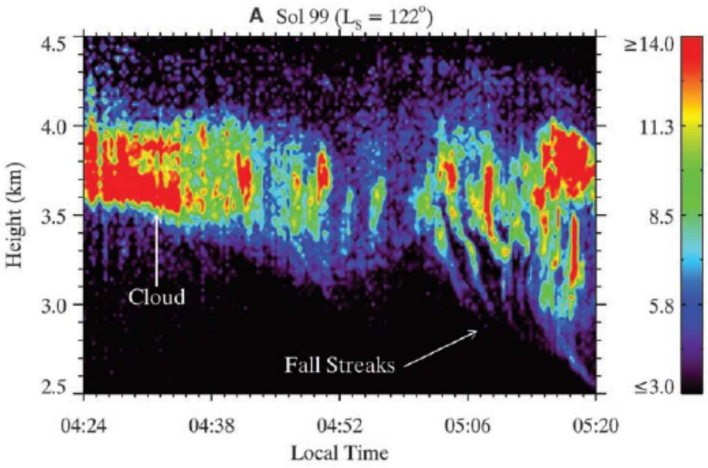

Figure 1.12: Contour plot of backscatter coefficient from 532 nm lidar measurements on sol 99 (L_s 122°) (Whiteway et al., 2009). Clouds are visible at 3.5-4.0 km, but fall towards 2.5 km after 05:00 LTST, showing features consistent with fall streaks seen in Terrestrial clouds (Whiteway et al., 2009).

Water-ice optical depth over the entire Phoenix mission is shown in Figure 1.13. A repeating diurnal pattern is shown with peak column ice-water content between 05:00 and 06:00 LTST (Dickinson et al., 2010). Lidar measurements showed clouds within the 8-10 km high PBL (Whiteway et al., 2009), (Dickinson et al., 2010).

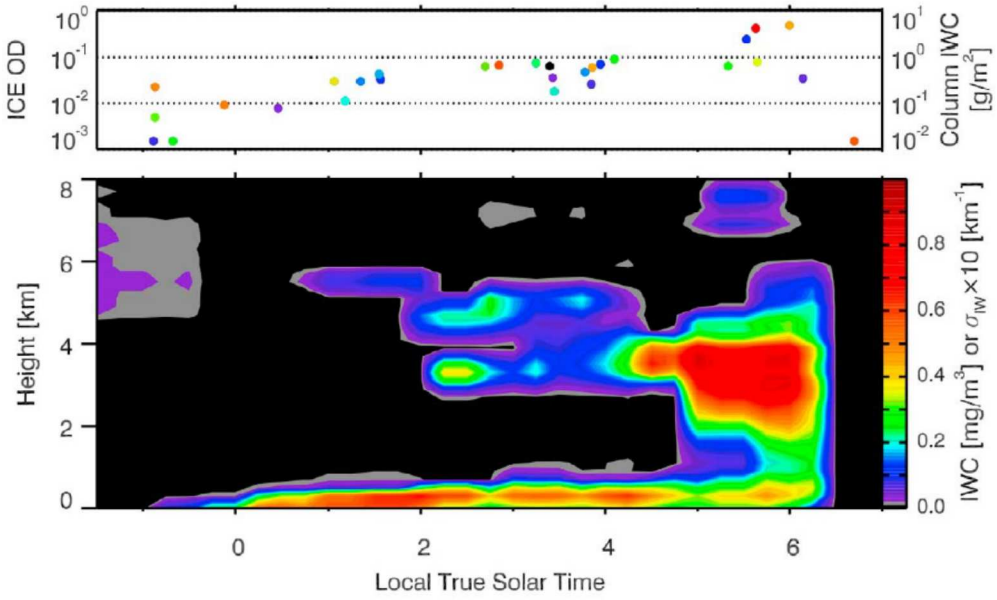

Figure 1.13: From (Dickinson et al., 2010), the top figure represents the integrated water-ice optical depth. The marker colour indicates the sol number with respect to the bottom figure where grey is sol 80 and red is sol 148 (Dickinson et al., 2010). The bottom figure shows the average ice-water content (IWC) as a function of LTST and altitude. The average optical extinction (σ_{WI}) is also shown by the contour. The peak IWC occured between 05:00-06:00 LTST (Dickinson et al., 2010)

Additionally, the SSI can provide images of the surrounding area to investigate atmospheric properties. The SSI is the primary imaging camera for Phoenix with a FOV of $13.8° \times 13.8°$ and image size of 1024×1024 (Moores et al., 2010). Atmospheric movies are produced using the SSI where the mean frame of each movie is subtracted to enhance faint features such as clouds (Moores et al., 2010). Zenith movies (ZM) have a 83.79° elevation, where the zenith point is in every frame, while suprahorizon movies (SHM) are pointed just above the horizon (Moores et al., 2010). Results showed cumulus-like clouds in SHM, but only till midsol where cloud formation diminishes (Moores et al., 2010). An example of clouds at the Phoenix site is shown in Figure 1.14

Figure 1.14: Cumulus-like clouds captured on sol 128 (Francis et al., 2014). This movie spanned 207 s and was enhanced to show thin clouds above the Phoenix landing site (Francis et al., 2014).

1.3 Mars Science Laboratory (MSL)

The Mars Science Laboratory, also known as Curiosity, celebrated its five year anniversary from landing on August 6th 2012. Greatly exceeding the design lifetime of one MY, Curiosity has been studying the local geology and atmosphere at Gale crater. There are four main science objectives to fulfill the overall goal of assessing past and present habitable environments in Gale crater (Vasavada, 2018):

- Assess the biological potential
- Characterize the local geology
- Investigate planetary processes of past habitability through long timescale atmospheric monitoring
- Characterize surface radiation from galactic cosmic radiation, solar proton events and secondary neutrons

Gale crater was chosen for Curiosity's landing site due to its potentially unique geological and atmospheric properties. Spanning 155 km in diameter, it contains a 5.5 km elevation central peak known as Aeolis Mons (Mt. Sharp). Geologically, strata at the base of the mountain contains hydrated materials indicating that Gale could have once held liquid water (Grotzinger et al., 2012). By studying these distinct layers, scientists can understand the past habitability and preservation of organic compounds. Due to Gale's equatorial position on Mars (4.5°S, 137.4°E), the ACB can be studied (Moores et al., 2015b) (Kloos et al., 2016; 2018).

With ten instruments onboard, Curiosity takes a wide variety of scientific measurements. Figure 1.15 illustrates the different instruments. For the scope of this work, the Navigation Camera (Navcam) is the only instrument used and is described in Section 2.1.1.

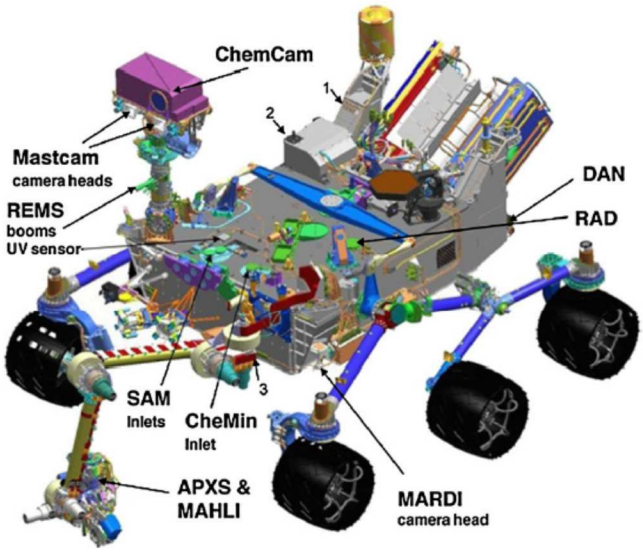

Figure 1.15: The location of the 10 different instruments onboard Curiosity (Grotzinger et al., 2012). For contact science, the Alpha-Particle X-ray Spectrometer (APXS) characterizes rover geological surroundings through x-ray spectroscopy and Mars Hand Lens Imager (MAHLI), located on the arm, takes images to help facilitate mineralogy of nearby rocks. Remote sensing employs the Laser-Induced Remote Sensing for Chemistry and Micro-imaging (ChemCam) to study rock and soil targets through lasers and Mast Camera (Mastcam) located on the mast of the rover and used to image geological targets. Environmental studies use the Dynamic Albedo of Neutrons (DAN) to measure the time decay of active and passive neutrons, Mars Descent Imager (MARDI) at the bottom of the rover to take images before and after landing, Radiation Assessment Detector (RAD) to understand the full spectrum of surface particle radiation and Rover Environmental Monitoring Station (REMS) to measure mesoscale and general circulation. Other instruments include Chemistry and Mineralogy (CheMin) and Sample Analysis at Mars (SAM) part of the MSL Analytical Laboratory to assess past and present habitability (Grotzinger et al., 2012).

Currently, the atmospheric movies taken by the Navcam are used to determine properties of clouds above Gale crater. Their meteorological wind direction and opacity have been previously determined (Francis et al., 2014) (Moores et al., 2015b) (Kloos et al., 2016; 2018). However, their altitude has not been constrained. Unlike Phoenix, Curiosity does not have a lidar that could measure the altitude of these clouds directly as seen by Whiteway et al. (2009). To solve this problem, cloud movement found through the ZMs can be correlated to computer modelled values.

1.4 Mars Atmospheric Models

To better understand atmospheric processes in the Martian atmosphere, Global Climate Models (GCMs) are tailored to Mars. Limited by our current data, numerical models can aid in filling in the blanks that limited resources on Mars cannot answer. When Martian water-ice clouds were discovered to have an effect on migration of water in the atmosphere, numerical models were created to better understand the water cycle on Mars. Richardson and Wilson (2002) used the Mars General Circulation Model (MGCM) to study the Martian water cycle. Several models are used in today's studies including the MGCM developed at Laboratoire de Meteorologie Dynamique (LMD) (Forget et al., 1999) and the Mars Regional Atmospheric Modelling System (MRAMS) developed at the Ames Research Centre (Rafkin et al., 2001).

Numerical climate models were created for Mars to understand vertical distribution of water vapour in the atmosphere for cloud studies (Hess, 1976). These initial models were steady-state with assumptions made for mean particle radius and neglecting particle microphysics (Michelangeli et al., 1993). By expanding these neglections, Michelangeli et al. (1993) developed a one-dimensional time-dependent aerosol model from Toon et al. (1988) that computed nucleation rate and growth by condensation sublimation. At this time, surface and orbital Martian atmospheric data was scarce where Viking orbiter and lander data were only used to confirm results (Michelangeli et al., 1993). Even with this little amount of data, Michelangeli et al. (1993) were able to reproduce optical depths and altitude values of water-ice clouds previously observed by Viking. With the arrival of MGS, more data was available to test and increase accuracy of numerical models.

The NASA Ames MGCM was developed in the 1990s based on an Earth GCM and included radiative

effects from dust and topography seen by the Mariner 9 and Viking missions (Haberle et al., 1993). First discussed by Pollack et al. (1990), this model was used after the Viking missions to study polar processes after more data about the Martian surface became available. The Viking missions showed a difference in composition between the northern and southern polar cap where the north had water-ice at the surface, but the south had carbon dioxide (Pollack et al., 1990). Models ran by Pollack et al. (1990) showed that Martian atmospheric dust has a strong impact on the polar caps where atmospheric advection transports heat into these regions causes an increase in dust optical depth. CO_2 ice clouds were predicted at high altitudes by the model based on elevated dust in the winter polar regions (Pollack et al., 1990). Pressure variations measured by the Viking landing sites were confirmed using this model where variations were large enough that Pollack et al. (1993) argue that the pressure variations should be detected by future spacecraft missions. Haberle et al. (1993) simulated circulation of the Martian atmosphere using the Ames MGCM to show that Mars' circulation is similar to Earth. Hadley and Ferrel cells were observed including a high altitude jet stream, but Mars' circulation differed in variability compared to Earth (Haberle et al., 1993). Haberle et al. (1993) found the most similarities between Mars and Earth circulation at the equinoxes where two symmetric Hadley cells develop in the mid-latitudes of each hemisphere. At the solstices, the two Hadley cells became a cross-equatorial cell covering half the planet (Haberle et al., 1993).

With data from Mariner 9, Viking and MGS, Richardson and Wilson (2002) developed a general circulation model to study the water cycle on Mars. In order to assess water mechanisms in the atmosphere, the seasonal evolution must be studied. The model was able to reproduce vapor maxima as seen in measurements from MAWD and TES, including a peak in cloud activity in the tropics in the aphelion season, agreeing with Clancy et al. (1996). However, the minimal amount of data available from Mars hindered fine tuning of this model (Richardson and Wilson, 2002).

A popular Martian circulation model was developed by Laboratoire de Meteorologie Dynamique (LMD). Originally developed in 1999, it was a combination of previous models to be redesigned as a sophisticated model accounting for all Martian meteorological processes (Forget et al., 1999). With a vertical domain of 80 km, this model allows interaction between the lower and upper atmosphere to be investigated (Forget

et al., 1999). The model was roughly consistent with previous models when below 40 km, but the thermal and dynamic structure above 50 km was difficult to predict without more observations by orbiters at those altitudes (Forget et al., 1999). Forget et al. (2011) fixed several aspects of the model including radiative transfer code and particle size. Used for several studies, the GCM developed by LMD has been used to study the influence of radiatively active clouds (Madeleine et al., 2012), (Navarro et al., 2014). Both cases raise the issue of needing better modelling for cloud formation and evolution based on radiatively effects. In most atmospheric models, it is hard to develop a model that can accurately predict water-ice clouds formation due to limited data from Mars.

Mars atmospheric models are useful for learning about the water cycle, but also about potential landing sites for future missions. Haberle et al. (1997) used the NASA Ames Mars GCM to predict the meteorological environment for the Pathfinder lander site. Predictions were made that Pathfinder would see meteorological conditions similar to what was observed at the Viking 1 landing site (Haberle et al., 1997). This was confirmed by Schofield et al. (1997) that found similar atmospheric structure and weather when compared to Viking. Using the MGCM developed by the Geophysical Fluid dynamics Laboratory (GFDL), Toigo and Richardson (2003) discussed the different range of topography in MER landing sites and its affect on local meteorology. However, model predictions can be inconsistent when there is sparse data on differing topographic sites on Mars where Toigo and Richardson (2003) argue that future landers should have meteorological sensors to increase this data set. For Phoenix, MRAMS was used to predict meteorological conditions (Michaels and Rafkin, 2008). Quiet sol-to-sol weather was predicted as well as a 3-7 km PBL during entry (Michaels and Rafkin, 2008). MRAMS has also been used for Curiosity's landing site, Gale Crater, to understand local meteorology (Pla-Garcia et al., 2016).

The most difficult part of Martian atmospheric models is knowing the uncertainty associated with simulated results. This is hard to define, especially for Mars, because of the sparse meteorological data available. Therefore, parameters calculated through atmospheric models are plausible if they are in the range of expected values based on remote sensing observations. This method is good for parameters that have remote sensing data such as temperature and atmospheric aerosols. For parameters associated with circulation,

such as winds, there is extremely limited data for surface winds and even less above the surface. However, as variables are highly coupled within an atmospheric model, if observed atmospheric variables are correct then circulation parameters are generally good.

To verify Martian atmospheric models, data from temperature and atmospheric tracers are used. Using TES, atmospheric temperature profiles were created using nadir-viewing spectral measurements (Conrath et al., 2000). Using the NASA Ames Mars GCM, profiles developed by Conrath et al. (2000) were in agreement with the modelled results. Earth-based radio occultation experiments are also used to measure the structure of the Martian atmosphere. The Mars Express Radio Science Experiment measured middle atmosphere parameters from the surface to 40 km (Tellmann et al., 2013). This method allows the middle atmosphere to be measured with very high vertical resolution (Tellmann et al., 2013). Another method to measure atmospheric profiles is through incoming surface spacecraft. During entry, descent and landing (EDL), atmospheric density, pressure and temperature can be measured from 100 to ¡10 km (Withers and Smith, 2006). To further verify modelled results, the model can be used to replicate diurnal and seasonal results observed by surface spacecraft. While upgrading the Ames Mars GCM, Haberle et al. (2003) tested the model by attempting to match seasonal and diurnal pressure results. When compared to Viking lander 1 and 2 data, the GCM gave a good fit to diurnal results (Haberle et al., 2003). Using these methods to accurately measure Martian atmospheric properties help verify atmospheric modelling results.

1.4.1 The Mars Regional Atmospheric Modelling System (MRAMS)

The Mars Regional Atmospheric Modelling System (MRAMS) is 5 day mesoscale simulation for Mars. It is based off the Regional Atmospheric Modelling System (RAMS) for Earth that is used to forecast weather and simulate over complex terrain (Rafkin et al., 2001). When inputting radiation parameterization, cloud microphysics are not active meaning MRAMS does not consider radiative clouds (Rafkin et al., 2001). The model outputs parameters during the 3rd sol to allow sufficient time for circulation. The several parameters outputted by MRAMS are described in Table 1.2 (Rafkin et al., 2001).

To verify MRAMS, Rafkin et al. (2001) ran simulations for the Pathfinder landing site. Running for 3

Table 1.2: Parameters outputted by MRAMS.

Parameter name	**Description**	**Unit**
u velocity	East/west component of wind velocity	m/s
v velocity	North/south component of wind velocity	m/s
w velocity	Vertical component of velocity	m/s
temperature	air temperature	K
press	air pressure	Pa

consecutive sols, the domain was 60 km in the horizontal and 22 km in the vertical with the model starting at 05:30 LTST at L_s 142° (Rafkin et al., 2001). Results showed MRAMS underpredicted the maximum temperature, but agreed with minimum temperature. Wind speeds were less than observed, but was accepted by Rafkin et al. (2001) as ASI/MET wind speed data were still under development. MRAMS was able to resolve the general diurnal atmospheric pressure that the Ames GCM could not, but the amplitude of the cycle was smaller than observations (Rafkin et al., 2001).

Michaels et al. (2006) coupled MRAMS to the NASA Ames MGCM cloud microphysics code to aid in modelling water-ice and dust. This new combined model ran for several sols until it stabilized in a diurnal cloud development cycle (Michaels et al., 2006). Simulations were able to reproduce observed cloud locations, orientations and morphology over the Olympus Mons region (Michaels et al., 2006). Mountain-induced circulation appeared to be more significant than previously thought which could inject water and dust above 40 km in altitude (Michaels et al., 2006). By using atmospheric models like MRAMS, we can infer knowledge about the Martian atmosphere by comparing observational values from rovers, such as Curiosity.

2 Method

2.1 Atmospheric Movies

Curiosity has imaged clouds above Gale Crater through atmospheric movies taken every 2-3 sols for the entirety of the mission. Using the Navigation Camera (Navcam), eight consecutive 512×512 pixel images are taken over a span of 235 seconds, where each frame is taken approximately 32 seconds apart. The main difference between the two types of atmospheric movies is their pointing. A zenith movie (ZM) is taken at 85° while a supra-horizon movie (SHM) is taken at 38.5°. Regarding azimuthal direction, this pointing changes depending on the path of the Sun through a MY. To minimize image saturation, azimuth pointing is due South during L_s 0°-190° and due North during L_s 191°-359°. By taking these movies, we can characterize the opacity, angular distance and wind direction of clouds above Gale Crater.

In previous works done by Moores et al. (2015b), Kloos et al. (2016; 2018), cloud activity was monitored and analyzed with the Navcam on Curiosity. The first 360 sols showed extremely faint features in the early morning or late afternoon (Moores et al., 2015b). Moores et al. (2015b) argue that these two peak time periods of activity correspond to the colder part of a sol, making it likely that they are thin water-ice clouds. Extending this data set, Kloos et al. (2016) examined the opacity for first 800 sols, while Kloos et al. (2018) analyzed interannual and diurnal variablility of 2 MYs (L_s 160° in MY 31 to L_s 160° in MY 33). Seasonally, clouds above Gale Crater were observed mainly during the ACB season, another suggestion that these clouds comprise of water-ice. Kloos et al. (2016) measured an average optical depth of 0.02 indicating the cloud's thin nature from small amounts detected by Jakosky and Farmer (1982). Diurnally, Kloos et al. (2018) found higher opacity during the morning than afternoon. Thicker clouds form more favourably in the morning as

atmospheric temperatures are cooler which is expected (Wolff et al., 1999).

One unknown parameter of the ACB above Gale Crater is altitude. At Green Valley, Phoenix was able to discern this property through lidar measurements. During L_s 113°-148°, clouds were observed within the boundary layer (Dickinson et al., 2010). Ice-water optical depth was consistent with values derived from Moores et al. (2010) using the SSI (Dickinson et al., 2010). Using SHMs and ZMs, Moores et al. (2010) found that the diurnal trend peaks at 10:00 LTST which suggests that morning clouds build overnight. This is also seen in Figure 1.13, showing clouds forming overnight when the atmospheric temperatures are the lowest (Dickinson et al., 2010). Unlike the morning, clouds diminished in the afternoon arguing that heating from the surface inhibits cloud formation (Moores et al., 2010).

The difference in location of Phoenix compared to Curiosity makes it difficult to compare results. Solar elevation is a bigger problem at Gale crater versus Green Valley because of the difference in latitude. Gale's equatorial position means the sun is no more than 30.8° away from the zenith point, restricting the time of sol a ZM can be taken (Moores et al., 2010). For Green Valley, the polar latitude means that the sun is always low in the sky, which allows the majority of the sol to be used for imaging. Morphology in atmospheric movies could be different between landing sites due to a 5.5 km mountain (Aeolis Mons) in the center of Gale crater. Orographic condensate clouds are more likely at Gale because of Aeolis Mons (Moores et al., 2015b). Kloos et al. (2018) found gravity waves in atmospheric movies that would be related to a surface features such as Aeolis Mons.

2.1.1 Navigational Camera

The instrument onboard Curiosity that is used to capture atmospheric movies is the Navigation Camera (Navcam). They are build-to-print copies of the Mars Exploration Rover (MER) Navcams where the only difference is a slightly more powerful heater allowing operation in colder ambient temperatures (Maki et al., 2011). If needed, a heater resistor circuit will warm up the electronics to a minimum of -55°C (Maki et al., 2011). A $45° \times 45°$ field of view (FOV) allows more of the sky to be viewed. Compared to a FOV of 13.6° for the SSI on Phoenix, the Navcam can observe a larger portion of the sky at once (Moores et al., 2015b). While

this is useful for observing larger-scale features of clouds above Gale crater, it restricts the Navcam pointing to minimize image saturation from the sun. When taking near-vertical atmospheric movies, a constraint of ± 2.5 hours from local noon is required to ensure the sun is not in the frame.

In total, there are two pairs of Navcams on Curiosity as shown in Figure 2.1. Only one pair is active at a time, where the second is for fault redundancy (Maki et al., 2011). Each Navcam contains a charge-coupled device (CCD) detector that are 1024×2048 pixels. These CCDs operate in frame transfer mode where the 1024×2048 pixeled detector is split into two regions: a 1024×1024 region recording the image and a 1024×1024 region that shifts and stores the image (Maki et al., 2011). For well exposed images, the Signal to Noise Ratio (SNR) is 200:1 (Maki et al., 2011).

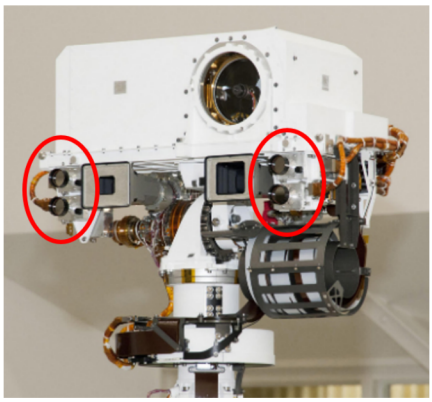

Figure 2.1: The two pair of Navcams on MSL are shown in red. Image credit: NASA/JPL.

The bandpass of the Navcam ranges from 600-850 nm. This is shown in Figure 2.2. The 600-850 nm wavelength is not the best light range to view ice crystals in the atmosphere, but is best for viewing geological features against a red source, like the Martian surface.

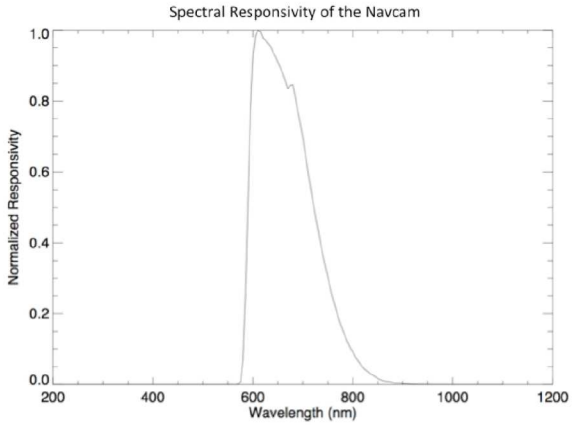

Figure 2.2: Optical bandpass of the Navcam centered at approximately 650 nm (Maki et al., 2011).

2.1.2 Mean-frame Subtraction Technique

The clouds on Mars are naturally thin due to the minimal amount of water present in the atmosphere (Jakosky and Farmer, 1982). Kloos et al. (2016) confirmed this for clouds at Gale crater with an average optical depth of 0.02. To observe thin clouds in atmospheric movies, ZMs are enhanced using the mean-frame subtraction technique. First, an average frame of all eight frames is created then this frame is subtracted from each individual image (Moores et al., 2015b). This isolates a time-variable component, showing clouds. Putting this together as a movie displays the movement of clouds across the frame. An example of a raw versus processed image is shown in Figure 2.3.

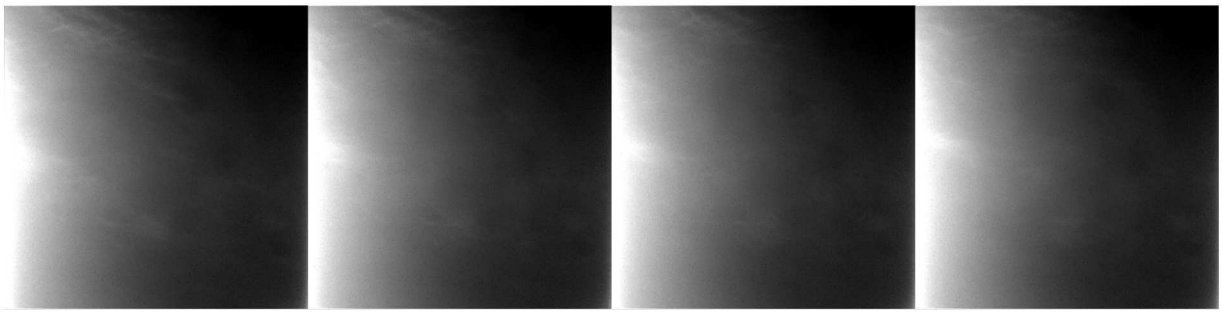

(a) Raw ZM with frames 1, 4, 5, and 8 on Sol 1758 at 06:46 LTST

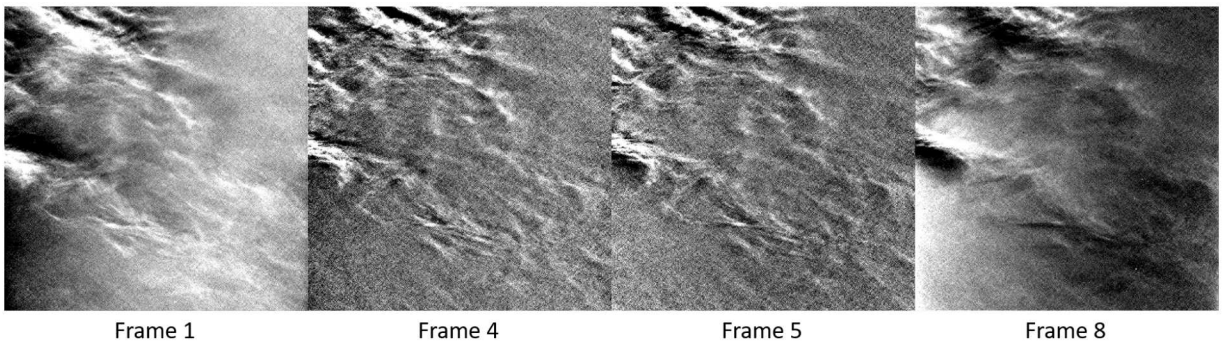

(b) Mean-frame subtracted ZM with frames 1, 4, 5, and 8 on Sol 1758 at 06:46 LTST

Figure 2.3: Comparison between raw and mean-frame subtracted frames. In Figure 2.3a, clouds can be seen faintly in the background. When using this technique, features from overhead clouds become more pronounced as shown in Figure 2.3b. Sol 1758 was a unique case showing wispy clouds at Gale Crater for the first time. This example was taken at L_s 34.5°, which is before the ACB season starts.

Clouds that are seen through atmospheric movies are classified based on a ranking scheme described in Moores et al. (2015b) and shown in Table 2.1.

Table 2.1: Quality rating described by Moores et al. (2015b) to classify features of clouds. A quality ranking of -1 indicates too much saturation from the sun in the atmospheric movie. The majority of movies are a quality ranking of 5 or less as shown in Figure 2.5a.

Quality Ranking	Description
10	No mean frame subtraction necessary to see features
8	Clear features visible upon mean frame subtraction
4	Faint features visible upon mean frame subtraction
0	Featureless frame upon mean frame subtraction
-1	Unusuable frame due to error or proximity to the sun

2.1.3 Supra-Horizon Movie (SHM)

The supra-horizon movie (SHM) is a type of atmospheric movie taken by Curiosity to study clouds above Gale Crater. At the beginning of the mission, the pointing for these movies was aimed just above Aeolis Mons at 38° elevation and 135° azimuth (Moores et al., 2015b). Table 2.2 shows the changes to this observation throughout the mission to today.

Table 2.2: SHM reference from Kloos et al. (2018)

Sol	**# of Frames**	**Length**	**pointing**
0-594	8	91 seconds	134.8°, 38.5°
594-910	4	39 seconds	125.1°, 10°
911-1031	8	266 seconds	134.6°, 43.5°
1032-1258	8	266 seconds	0°, 26.3°
1259-today	8	266 seconds	180°, 26.3°

From sol 911 to today SHMs consist of eight 512x512 with a 26° elevation and azimuth changing between 0° and 180° depending on season (Kloos et al., 2018). The sun's path changes over the course of a MY

depending on season where the sun is in the northern sky during L_s 0°-190° and southern sky during L_s 191°-359°. The atmospheric movies would be pointed south then north respectively. An example of a SHM is shown in Figure 2.4.

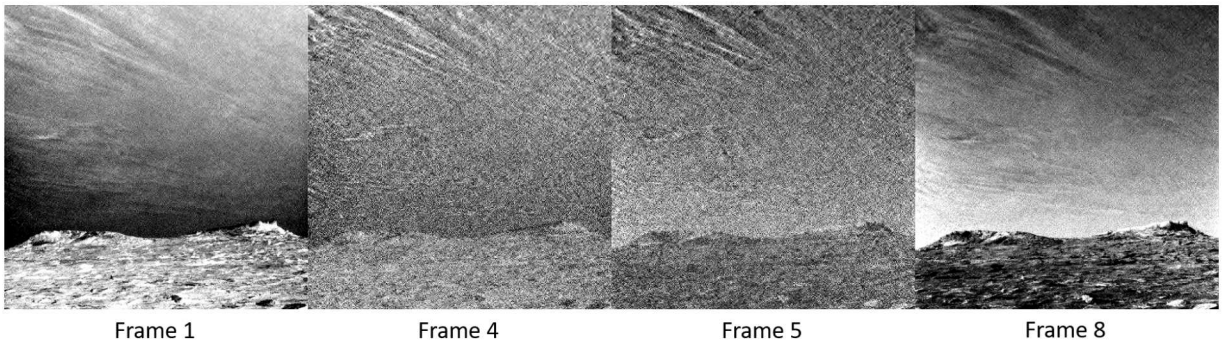

Figure 2.4: A SHM taken on sol 1758 at 06:46 LTST. Frames 1, 4, 5, and 8 show the movement of clouds over the entire eight frames. Wispy water-ice clouds are evident and show streak-like features.

The reasoning behind this type of atmospheric movie stems from the Phoenix mission. Angled above the horizon allows the light to travel the longest path length through the atmosphere showing thin layers close to the surface (Moores et al., 2010). Morphology is also seen more clearly through these movies, allowing the opportunity to search for orographic condensation caused by Aeolis Mons (Kloos et al., 2016). As of June 2018, 492 SHMs have been taken by Curiosity throughout the mission.

2.1.4 Zenith Movie (ZM)

The zenith movie (ZM) is the second type of atmospheric movie taken by Curiosity. They differ from a SHM in that the elevation is 85° with the zenith point in every frame. This high elevation means sun-safety has to be considered. Another factor affecting sun-safety is the Navcam's large 45° ×° 45 FOV. To accommodate this, a ZM cannot be taken ±2.5 hours from 12:00 LTST (Local noon). ZMs are deemed unusable if the sun is in the frame due to saturation (Kloos et al., 2018). ZM data sets have no observations between 10:00 LTST and 14:00 LTST. SHMs do not have this constraint because of their lower elevation angle. An example of a ZM is shown in figure 2.3b.

The vertical pointing enables the shortest path length through the atmosphere, allowing higher altitudes clouds to be observed (Kloos et al., 2016). Wind direction and velocity can be determined through ZMs, however, we cannot find absolute velocity without also knowing the altitude of the clouds. Curiosity cannot directly measure this without a lidar onboard. Section 2.2 explores measuring angular distance and meteorological wind direction while section 2.3 relates these two parameters to infer an altitude for clouds above Gale Crater. As of June 2018, a total of 901 atmospheric movies have been taken with 409 being ZMs. Figure 2.5 shows the timing and quality versus season.

Opacity and wind direction have been determined in previous works by (Kloos et al., 2016; 2018), (Francis et al., 2014), but not altitude. This work will go into depth about using ZMs to find angular distance and wind direction then comparing results from an atmospheric model to estimate an altitude. Only ZMs are used because of their vertical pointing. 118 out of 409 ZMs have been used due to absence of features in the majority of movies according to Figure 2.5c.

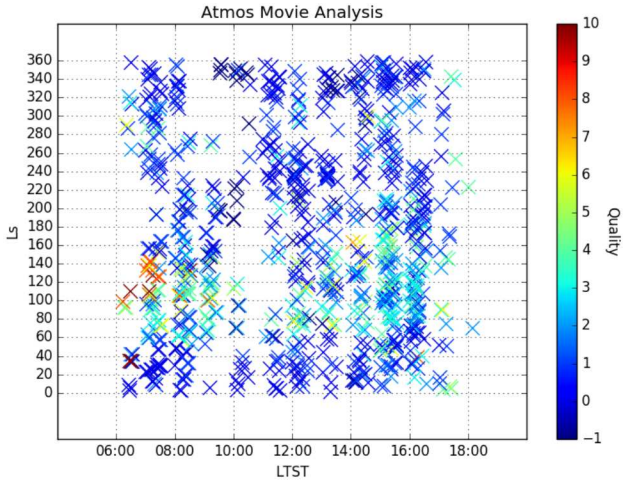

(a) Quality values of all atmospheric movies taken as of June 2018. Movies within the ACB season (L_s 45° to 150°) are generally of a higher quality than other seasons.

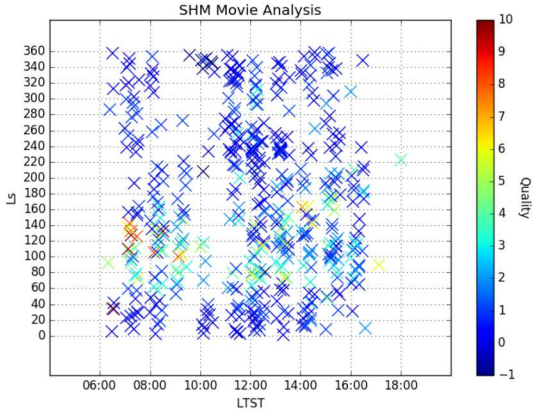

(b) Quality values of all SHMs taken as of June 2018.

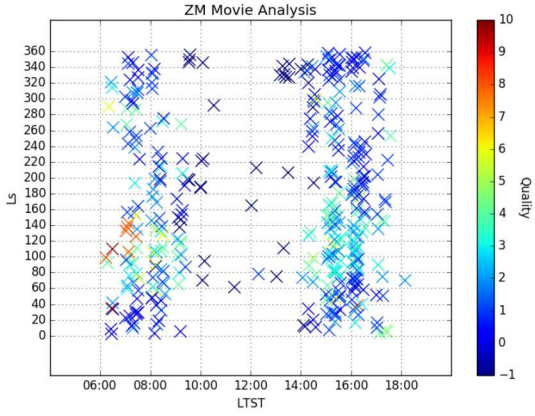

(c) Quality values of all ZMs taken as of June 2018.

Figure 2.5: Graphs showing seasonal and diurnal variability in quality of atmospheric movies. Figure 2.5a shows the quality of all atmospheric movies taken by Curiosity so far in the mission. The ACB is easily definable by higher quality movies between L_s 45° to 150°. Figure 2.5b shows SHM quality and Figure 2.5c shows ZM quality. The time constraint of ±2.5 hours from local noon is evident in Figure 2.5c between 10:00-14:00 LTST.

2.2 Extracting Wind Velocity and Direction

Clouds are identified in ZMs based on movement of features throughout the observation. The short timescale of a ZM means the cloud will keep the same relative shape for the entire movie. This is similar to terrestrial clouds which keep a relative shape for short periods with more varying shapes over longer timescales. If dust was in the frame, movement would be more chaotic. Figure 2.6 illustrates a ZM with dust rather than clouds. As seen in Figure 2.6, the features within the frames have more chaotic movement compared to Figure 2.3b, which would indicate dust.

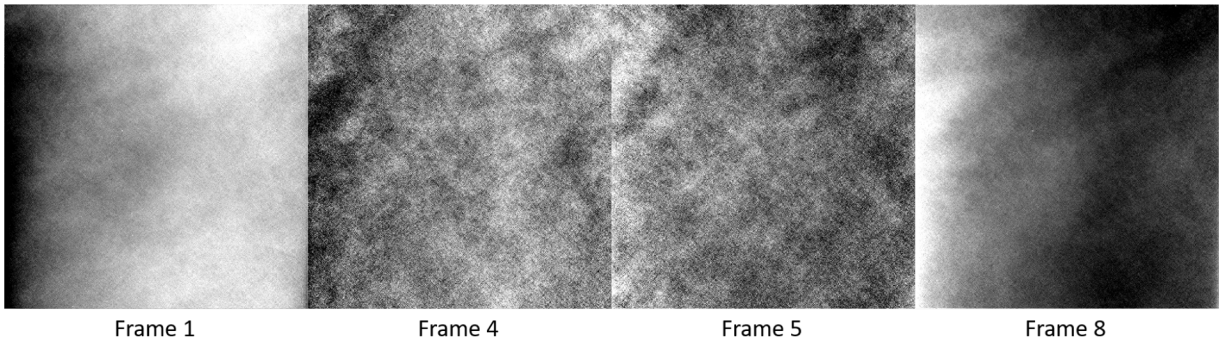

Figure 2.6: Mean-frame subtracted frames on sol 1886 in the early morning (06:29 LTST) showing an example of dust. The chaotic movement compared to cloud, as seen in figure 2.3b, indicates that movement is caused by dust rather than clouds.

The wind velocity and wind direction can be measured through ZMs, however the velocity cannot be directly determined without first knowing the altitude. The distance the clouds travel is calculated through angular resolution of the Navcam. Each ZM is 512×512 pixels and the Navcam FOV is $45° \times 45°$. As shown in Equation 2.1, each pixel corresponds to $0.08789°$ allowing us to find the angle swept by clouds overhead.

$$\frac{FOV}{\#pixels} = \frac{45°}{512} = 0.08789°/pixel \tag{2.1}$$

To reduce error in following features in ZMs, a grid is overlaid where each cell corresponds to 10 pixels. Clouds are followed with respect to the grid for pixel distance. The distance travelled ($d\theta$) over the entire

ZM is the angular distance of the clouds. The meteorological wind direction (φ) is the angle the clouds move with respect to a compass rose and observational azimuth at that season. To minimize sun saturation south-pointing azimuth occurs for L_s 0°-190° while north-pointing occurs otherwise. All ZMs in this study were analyzed by eye. Analyzed sol 1758 is shown in Figure 2.7 with calculated parameters shown in Table 2.3.

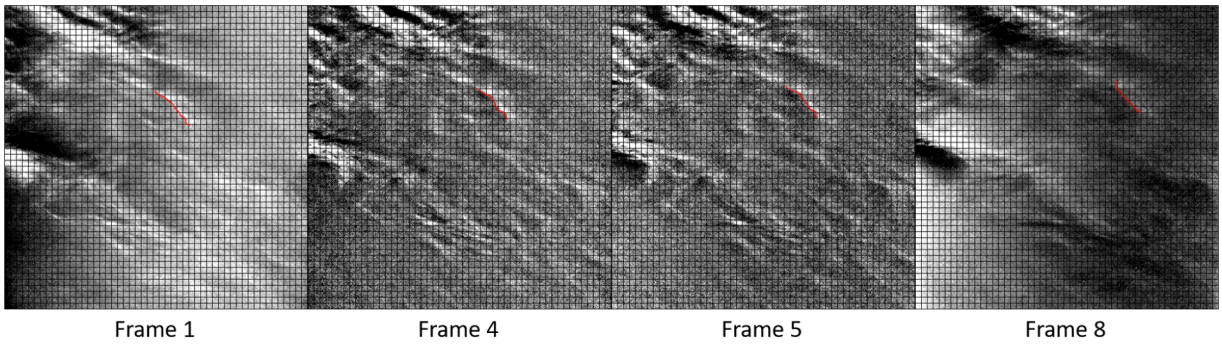

Figure 2.7: A feature that is followed is shown in red. A cloud is identified by the shape consistency through each frame. The angular distance travelled is found through the amount of cells the clouds moved from frames 1 to 8. The meteorological wind direction is found by overlaying a compass rose and following the direction in which clouds moved.

Angular Distance (±2°)	**Meteorological Wind Direction** (±5°)
6.69	66

Table 2.3: Values found for sol 1758 as shown in Figure 2.7. Larger errors are associated with these values because of the manual method of following features. The angular distance error is approximately 2 cells, where a cell is 10 pixels. The meteorological wind direction error was found by the average width of features when compared to ticks on the compass rose.

After applying this method to all ZMs that have clouds, an angular distance and meteorological wind direction data set is created and compared to results from MRAMS.

2.3 Correlating observational values with MRAMS

There is a total of 12 simulations at L_s 30° resolution over a MY, computed by Alexandre Kling at the AMES Research centre. With each simulation running on the Pleiades computer at the Ames Research Centre, 17 processors were used for around 48 hours of run time per simulation. The model is spun-up for three Martian days (sol) and analysis is preformed on the following three sols. As MRAMS is a mesoscale model, it needs an initial condition to start with boundary conditions provided by the NASA Ames Global Circulation model (Ames Mars GCM).

The Ames Mars GCM runs at a resolution of 5° latitude and 6° longitude. It is a fully interactive water cycle with a dust map scenario derived from observations. This dust map scenario guides moving dust in the Ames Mars GCM to assimilate dust opacities. Water columns calculated by the model match well with observations measured by TES and MCS (Kahre et al., 2017).

MRAMS simulations use 4 nested grids with a resolution of 240 km on the mother grid and 8 km for the smaller grid. 18 points are within Gale crater because of its 150 km diameter. This amount of points allows the rim and mounds be resolved allowing regional circulation to be captured. The vertical grid has levels fixed in space, which increase from 30 m at the surface to 2,500 m at the top of the model (50 km) (Rafkin et al., 2001).

The MRAMS outputs used in this project are wind velocity and wind direction. Wind velocity is given in u (east/west), v (north/south) and w (vertical) components. The w component is negligible and thus not used in this study. The wind velocity vector ($\vec{v}$) is calculated by combining u and v components and translated to an angular wind velocity ($d\theta$) as shown in equation 2.2. The meteorological wind direction (φ) is shown in Figure 2.8b.

$$\begin{aligned} \vec{v} &= \sqrt{u^2 + v^2} \\ d\theta &= \tan^{-1}\left(\frac{\vec{v}}{h}\right) \end{aligned} \tag{2.2}$$

Each parameter is outputted every 30 minutes on day three of the five day simulation. Provided in

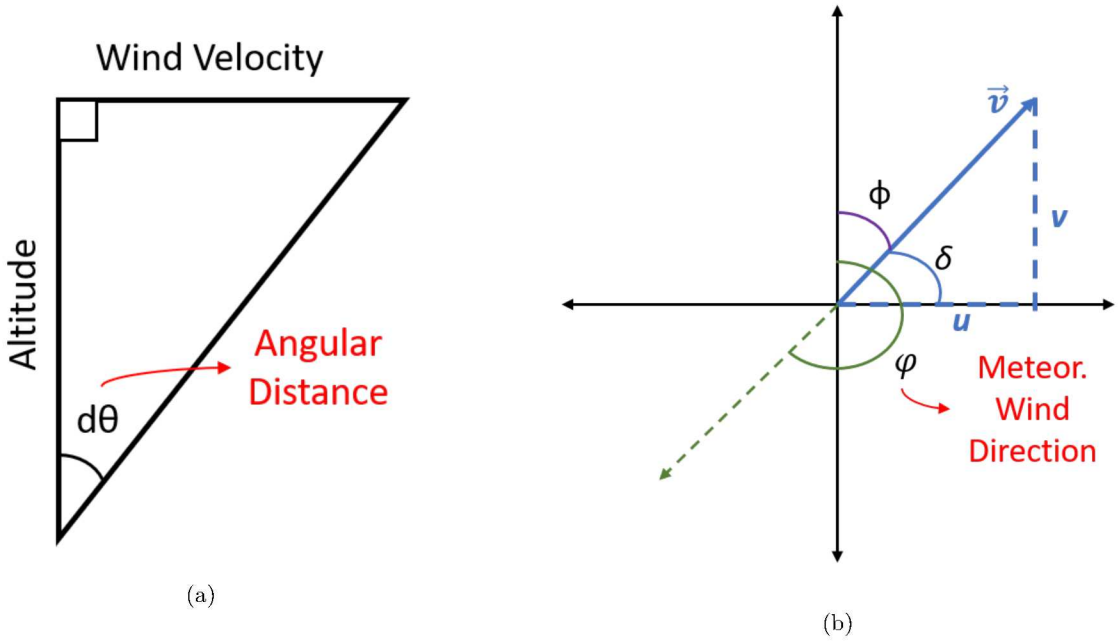

Figure 2.8: Diagrams illustrating trigonometry used to find angular distance and meteorological wind direction.

csv files, they are read in and analyzed with Python. The MRAMS values are interpolated to the time of observation for each ZM through linear interpolation.

Graphs are produced showing how the angular distance and wind direction change with respect to altitude and the ZM observation time. As shown in Figure 2.9, the observational ZM value is compared to the MRAMS data to determine the altitude. A probability formula is used to determine the highest-probable altitude which is discussed in section 2.4.

2.4 Half-Normal Probability Distribution

The half-normal probability distribution is described in Equation 2.3. This probability distribution is a special case of the folded normal distribution where the mean (μ) is zero. Dealing with absolute values, $y = |x|$ is folded in half (Elandt, 1961). This distribution is folded at the mean, in this case 0 (Leone et al., 1961). The variance (σ^2) can be estimated by Equation 2.4 (Tsagris et al., 2014). $\sigma = 0.8$ was found to be

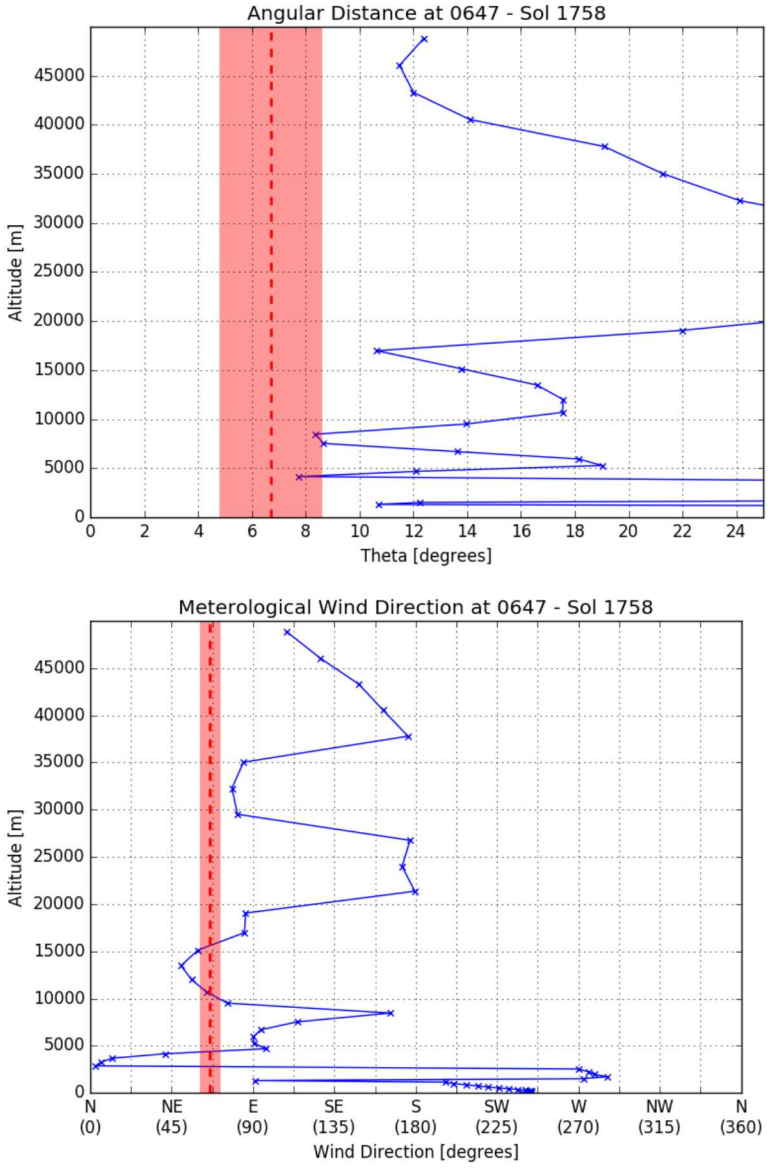

Figure 2.9: The MRAMS data is plotted in blue while the observation value from the ZM is shown by the red dashed line with the red shaded area representing error. At each altitude point, MRAMS has a corresponding angular distance and meteorological wind direction. By comparing the observational value (red dashed line) to the MRAMS plot (blue line), the altitude can be estimated where these two values meet.

the best value based on the most probable value found for probabilities.

$$P(x_i) = \frac{1}{\sigma}\sqrt{\frac{2}{\pi}}\exp\left[-\frac{x_i(z)^2}{2\sigma^2}\right] \tag{2.3}$$

$$\sigma^2 = \frac{1}{n}\sum_{i=1}^{n} x_i(z)^2 \tag{2.4}$$

To use this equation, we must find the difference between the observational value and MRAMS value at each altitude, x_i, as shown in Figure 2.10.

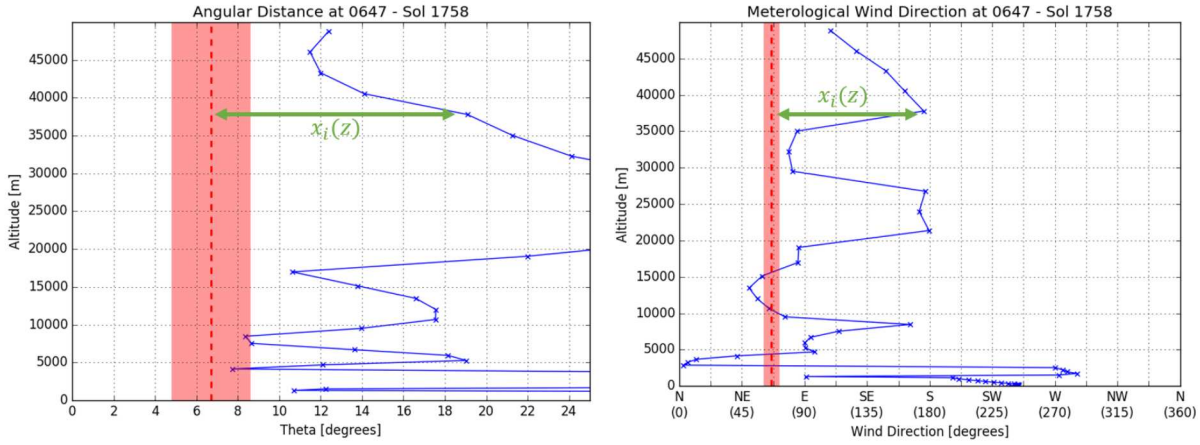

Figure 2.10: Shown in green, the distance between the observational ZM value (red dashed line) and the MRAMS value would be $x_i(z)$ in equation 2.3.

The half-normal probability density equation is applied to the data by first finding the distance ($x_i(z)$)) of each ZM value versus MRAMS value for each altitude point. A loop in set up to go through each altitude point individually and record this distance value. Once $x_i(z)$ is calculated for this ZM example, it is put through the half-normal probability density equation and stored for all the altitude points for this example. Since there are two parameters for this study, angular distance and meteorological wind direction, the half-normal probability density is calculated twice and multiplied together for the total probability (Equation 2.5). If there is more than one ZM for a specific 30 minute MRAMS interval, the probabilities are averaged together. This process is done for each season. Before graphing plots for the probabilities, all the probability

values are normalized for each 30 minute interval. First, the sum of all the individual probabilities is found then each individual value is divided by that sum.

$$P(x_i)_{total} = P(x_i)_{ad} \times P(x_i)_{wd} \tag{2.5}$$

Cloud altitude probability contour plots will be assessed diurnally and seasonally. By looking at how altitude changes diurnally, we can assess how clouds form for the two known peak activity time. Seasonal patterns are analyzed by plotting results over a MY, as shown in Section 3.

3 Results and Discussion

3.1 Diurnal Results

Figures 3.3-3.13 show the results for altitude probability for clouds during a sol and season. These seasons are modelled with MRAMS every 30° L_s. For each set, a histogram of ZM time is shown underneath with altitude (km) on the y-axis. The histogram shows the movie population between the morning and afternoon. All ZMs used in this study are give in tables in Appendix A.

For each season, a graph with pressure (Pa) on the y-axis is given. Pressure on Mars varies on seasonal and diurnal timescales as measured by surface spacecraft. During the Viking missions, surface pressure was measured to look at diurnal and seasonal changes. As shown in Figure 3.1, surface pressure changes significantly on a seasonal timescale.

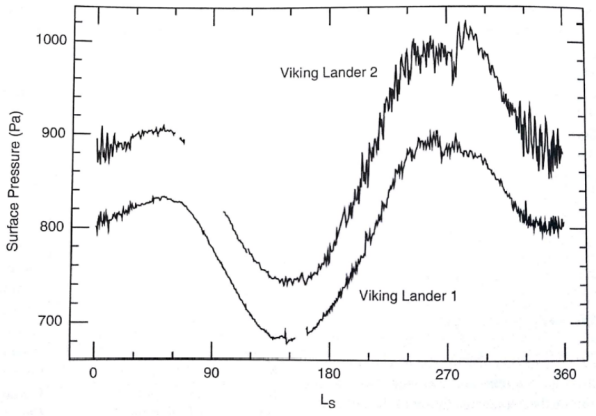

Figure 3.1: The daily average surface pressure recorded by both Viking landers during the first year of operation (Smith et al., 2017).

Several factors cause this seasonal change, including Marss highly elliptical orbit and albedo of the polar cap as measured by models (Paige and Wood, 1992). Another factor that affects pressure is elevation. This is represented by the offset between the two Viking Lander data in Figure 3.1 as the elevation difference between the two landing sites is 1.2 km (Smith et al., 2017). On diurnal time scales, the Rover Environmental Monitoring Station (REMS) on the Mars Science Laboratory (MSL) measured maximum and minimum pressures at 08:00 LTST and 17:00 LTST respectively (Haberle et al., 2014). Sol-to-sol variability is apparent in the secondary maxima and minima as shown in Figure 3.2. These secondary features are observed around 03:00 LTST and 20:00 LTST (Haberle et al., 2014).

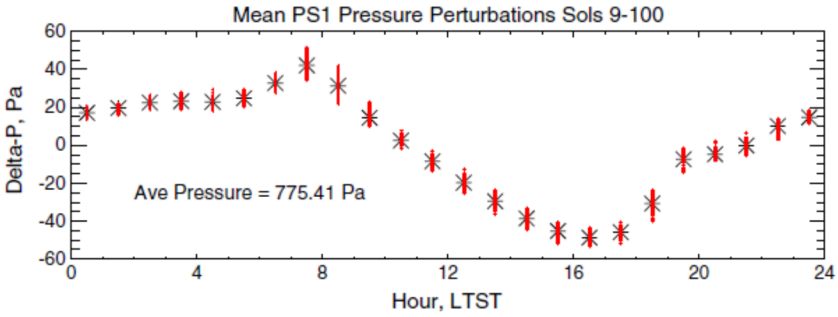

Figure 3.2: Figure by Haberle et al. (2014) showing the average pressure departure from the daily mean. This was measured between sols 9-100, with a maxima at 08:00 LTST and minima at 16:00.

As pressure is a variable calculated by MRAMS, it is factored into our diurnal graphs so we can relate pressure and altitude specifically at Gale crater.

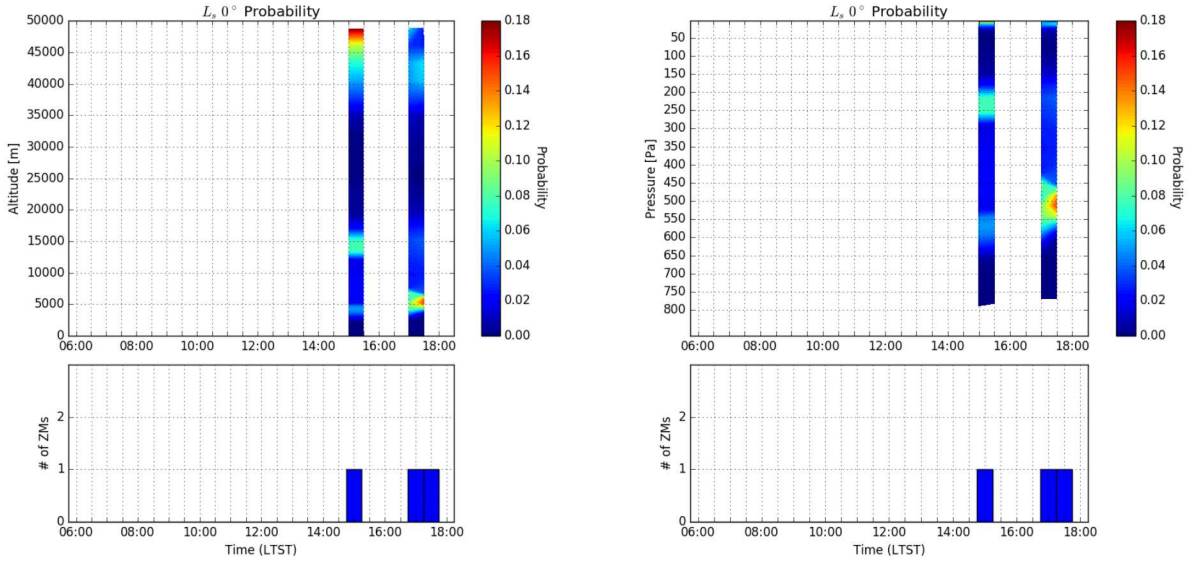

(a) (b)

Figure 3.3: Altitude probability graphs for L_s 0° with a total of 3 movies (15:17, 17:03 and 17:41 LTST). 3.3 has higher chance of clouds at very high altitudes (50 km) or in the lower atmosphere (< 15 km). Low probabilities exist between 20-40 km and below the crater rim (< 3 km). More movies, especially during the morning, will help characterize altitude of clouds during this season.

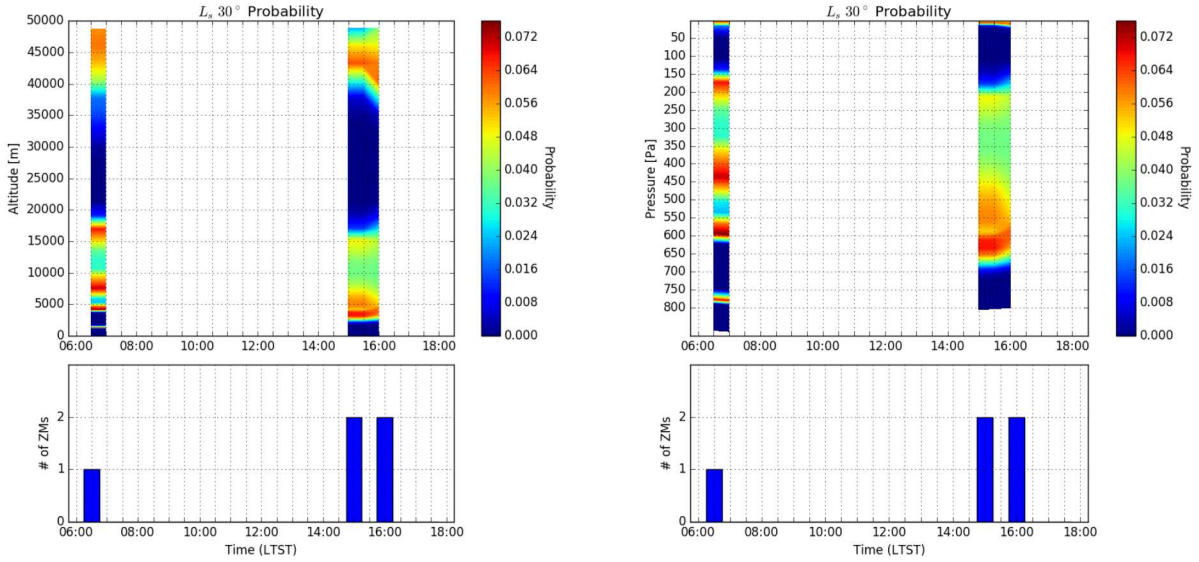

(a) (b)

Figure 3.4: Altitude probability graphs for L_s 30° with a total of 5 movies. The majority of the ZMs were in the afternoon (15:02, 15:17, 16:17, 16:29 LTST), with one in the morning (06:46 LTST). Figure 3.4 shows high probability of clouds in the higher atmosphere (> 40 km) and below 20 km in both morning and afternoon. The low probabilities between 20-40 km was also evident in Figure 3.3 which might indicate a seasonal pattern. More ZMs are needed for this season to increase the reliability of the results. High probability of clouds are predicted below 550 Pa (2 km), which would correspond to the top of crater rim at Gale. This high-probable feature is not in the afternoon results, indicating a diurnal change.

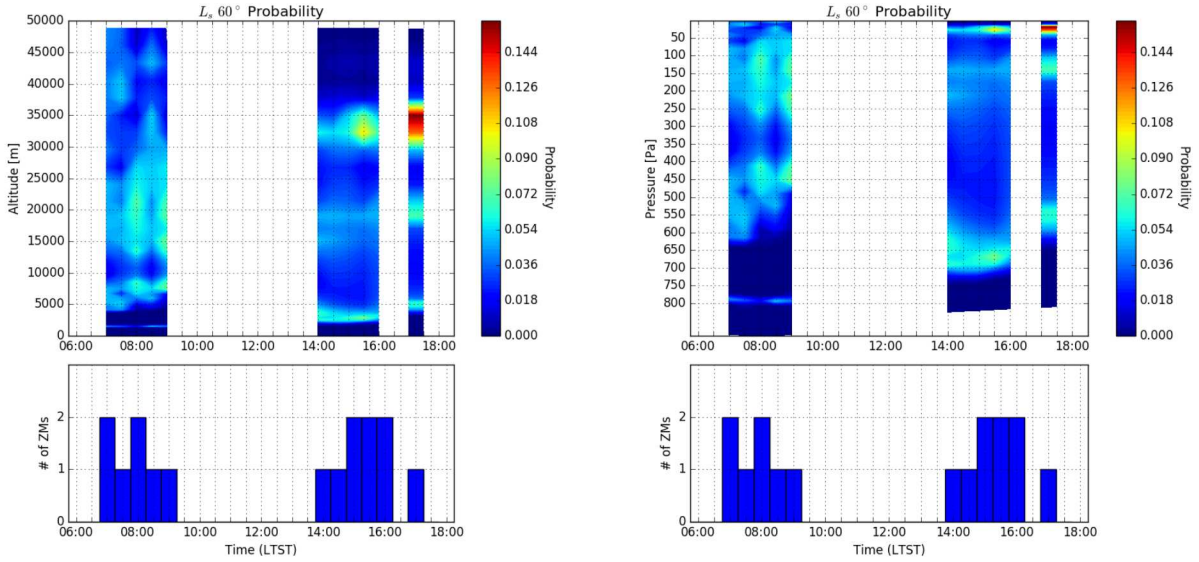

(a) (b)

Figure 3.5: Altitude probability graphs for L_s 60° with 16 movies. This season is during the ACB season, where clouds are more likely to be seen in atmospheric movies, as shown by the higher population of usable movies in this season compared to L_s 0° (Figure 3.3) and 30° (Figure 3.4). The amount of movies is consistent between the morning and afternoon. The morning had 7 ZMs (07:04, 07:08, 07:57, 08:11, 08:28, 08:58, 09:13 LTST) and the afternoon had 9 ZMs (14:07, 14:45, 15:01, 15:06, 15:39, 15:51, 16:04, 16:22, 17:28 LTST). Figure 3.5 show several high-probable areas in the morning, but is limited to below 40 km in the afternoon. This indicates that clouds could form throughout the atmosphere up to 50 km, possibly due to the cooler temperatures overnight during aphelion. Another consistent feature between seasons is the low altitude band at the crater rim, only in the morning movies. Lastly, the low probabilities that were seen between 20-40 km in Figure 3.3, and 3.4 are not evident during this season.

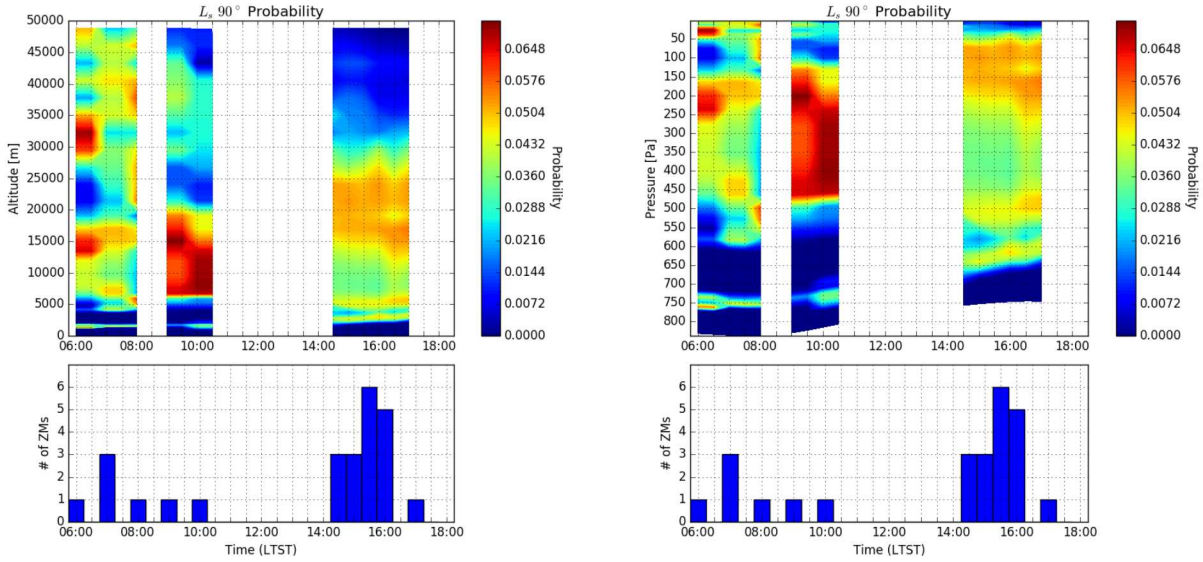

(a) (b)

Figure 3.6: Altitude probability graphs for L_s 90° with 26 movies (7 in the morning and 19 in the afternoon).

Figure 3.6 shows several high-probable areas throughout the morning, similar to Figure 3.5 indicating a possible ACB seasonal pattern. The low altitude band above the crater rim is seen in the morning and afternoon. One morning movie (10:16 LTST) was considered unusable due to saturation from the sun, but was analyzed due to clouds being visible in the frame. This allows a glimpse into the altitude behaviour of cloud towards mid-sol, where clouds are less likely (Kloos et al., 2018). This late morning movie shows high probabilities between 10-15 km with low probabilities at higher altitudes. This band is located just above the PBL where higher altitude clouds could have been burned off by increasing atmospheric temperatures. Afternoon results show higher probabilities for clouds from 15-25 km, with low probabilities $>$ 30 km. Low probabilities at these high altitudes could be caused by warmer atmospheric temperatures, with CCN influencing clouds more towards the surface.

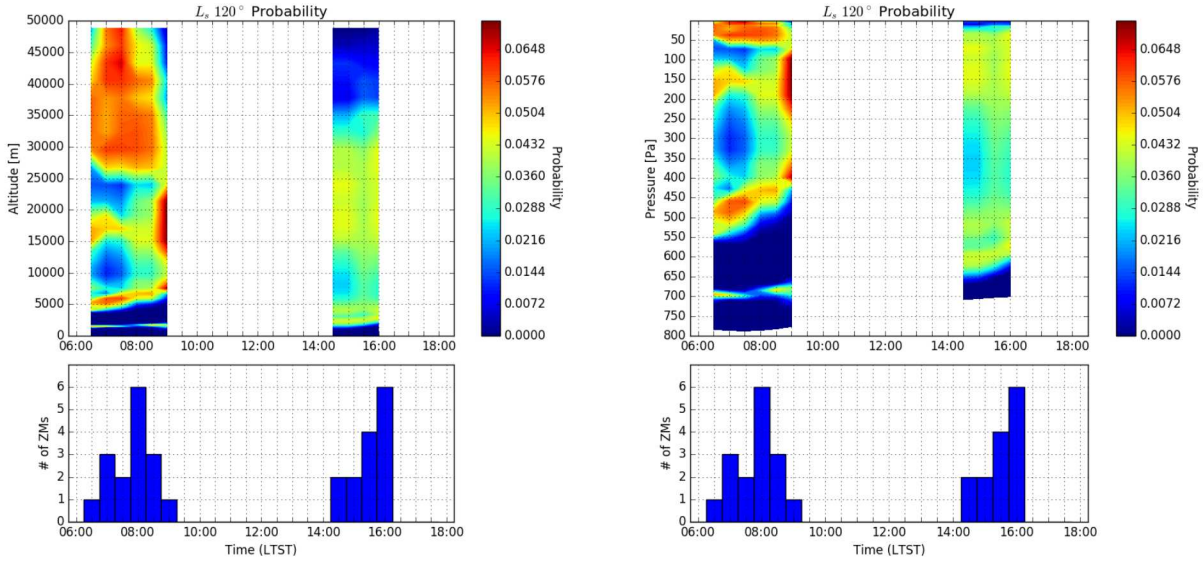

(a) (b)

Figure 3.7: Altitude probability graphs for L_s 120°, with 30 movies (16 in the morning and 14 in the afternoon). This season has the largest population of ZMs, especially in the morning, due to an increase in acquisition during the latest ACB season in early 2018. In Figure 3.7, morning results show high probability for clouds at both high and low altitude clouds, consistent with results from other ACB results (Figures 3.5, 3.6). Another reoccuring pattern is high-probable clouds just above the crater rim in the morning. Afternoon results in Figure 3.7 have consistent probability for clouds between 3-35 km, but show low probabilities outside this range. A wide range of probabilities makes it more difficult to determine cloud heights.

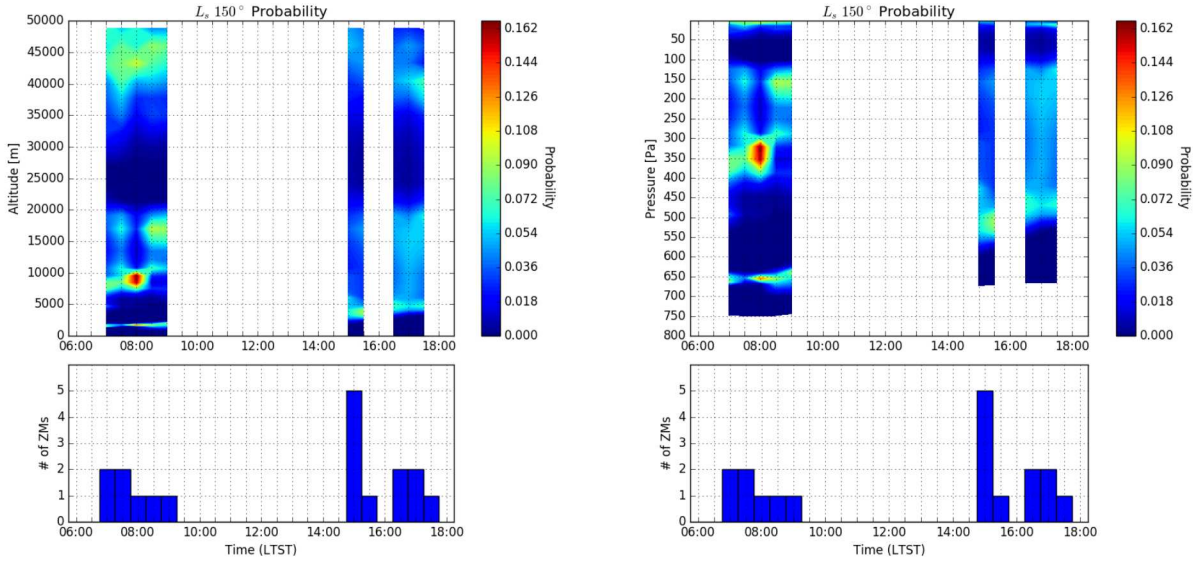

(a) (b)

Figure 3.8: Altitude probability graphs for L_s 150° with a total of 18 split between 7 morning movies and 11 afternoon movies. This is the last simulation for the ACB season, before it transitions into the dusty season where less clouds are seen in ZMs. Figure 3.8 shows three altitude ranges in the morning that have high probabilities: 3 km, 7-20km and 40-50 km. Outside of these ranges (4-7 km, 20-40 km) show low probabilities. This is different than the other ACB seasons that showed consistent probabilities throughout the whole atmosphere. The low probabilities between 20-40 km were evident in L_s 0° and L_s 30° results, before the ACB started. This low probable feature in the morning, could be a seasonal pattern. Low probabilities between 20-40 km is also shown in the afternoon results, with high probabilities similar to morning results.

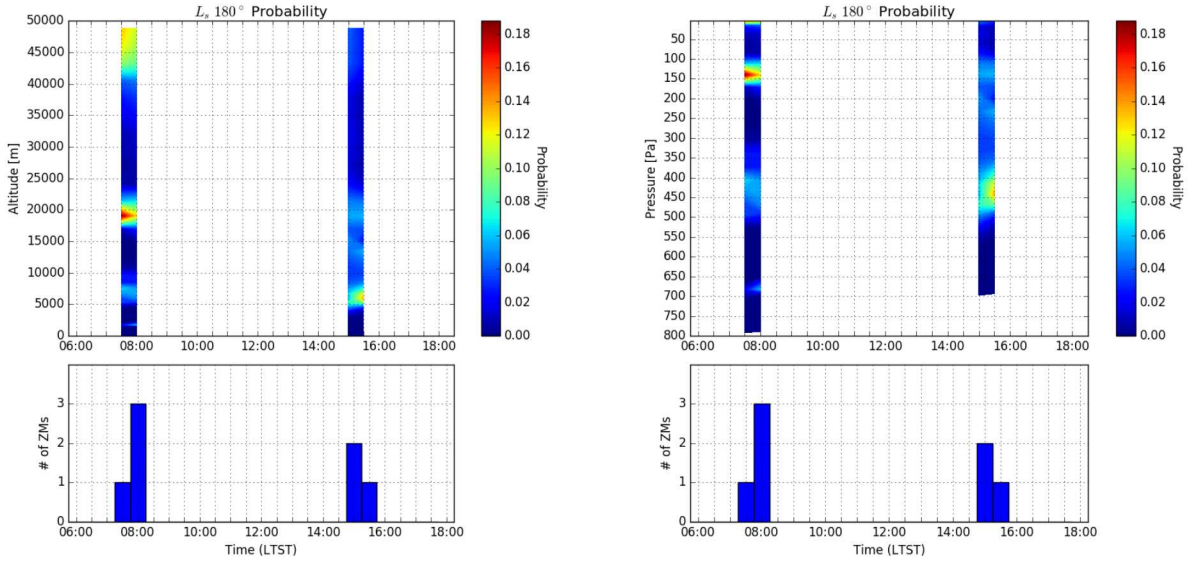

(a) (b)

Figure 3.9: Altitude probability graphs for L_s 180° with only 7 movies analyzed for this season. With the ACB season done, clouds are not as common in the Martian atmosphere (Smith, 2004). The morning had 4 ZMs (07:42, 08:13, 08:16, 08:29 LTST) and the afternoon had 3 ZMs (15:16, 15:22, 15:44 LTST). Figure 3.9 only shows 19 km and 45-50 km as possible altitudes for clouds in the morning. For the afternoon, clouds are predicted within the PBL, around 6 km. Not many high-probable altitudes indicates that clouds may not be that probable in this season. The high-probable region above the crater rim in morning results is not as probable in this season. Getting more ZMs during this season would help expand this data set to improve our probability confidence.

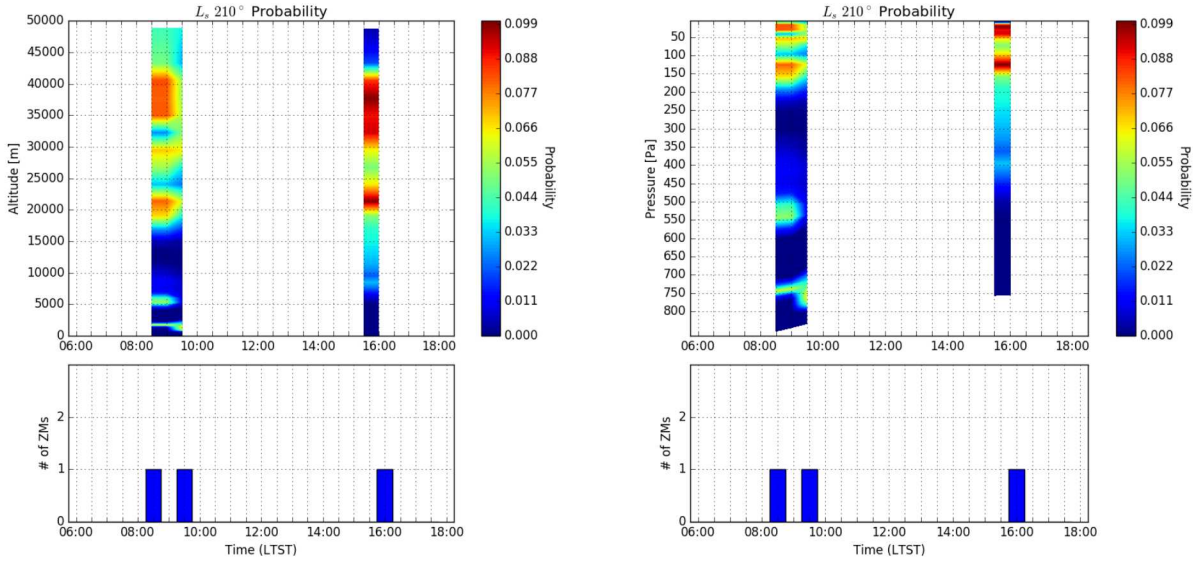

(a) (b)

Figure 3.10: Altitude probability graphs for L_s 210° with a total of 3 movies, 2 in the morning (08:43, 09:32 LTST) and 1 in the afternoon (16:17 LTST). Figure 3.10 shows little diurnal change between the morning and afternoon. Both peak times have high-probable altitudes between 20-40 km, which is opposite to other seasons that had this altitude range as low probability. The crater rim high-probable region is identifiable in the morning. More ZMs are needed to increase our confidence in this season due to the low ZM population.

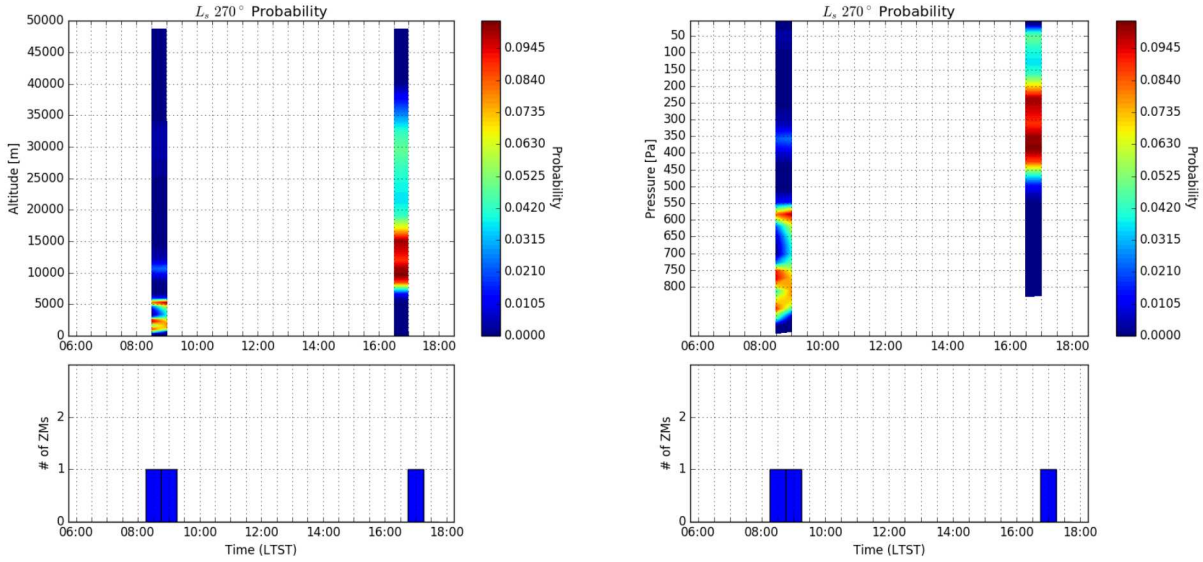

(a) (b)

Figure 3.11: Altitude probability graphs for L_s 270°, with 2 morning movies (08:50, 09:25 LTST) and 1 afternoon movie (17:11 LTST) totalling 3 movies. The only high-probable region in the morning for this season is below 5 km, just above the crater rim. Afternoon results shows clouds are most probable between 10-15 km, just above the PBL. More ZMs would increase the population and confidence in these results.

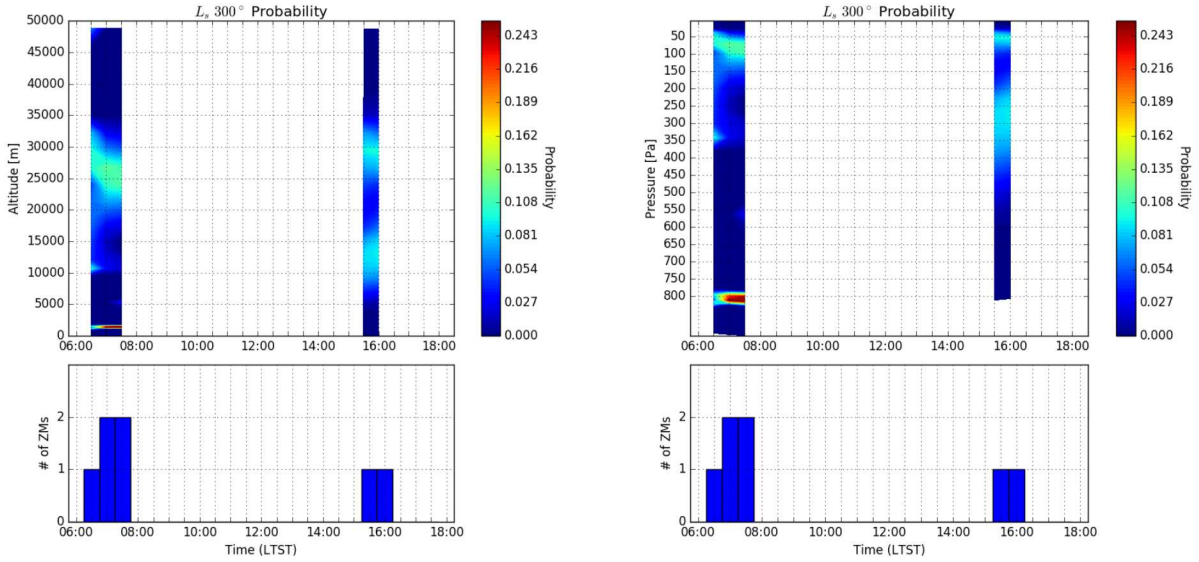

(a) (b)

Figure 3.12: Altitude probability graphs for L_s 300° with a total of 7 movies ranged 5 in the morning (06:36, 07:01, 07:09, 07:31, 07:52 LTST) and 2 in the afternoon (15:40, 16:01 LTST). Figure 3.12 show clouds most likely at the crater rim, in the morning. The afternoon shows probability in the middle atmosphere (30 km) or above the PBL (12 km), but not as probable as the morning values at the crater rim. This season is within the dust season on Mars, where clouds are not as prevalent (Smith, 2004). More clouds were analyzed during the morning compared to the afternoon which may indicate when clouds are more common in this season.

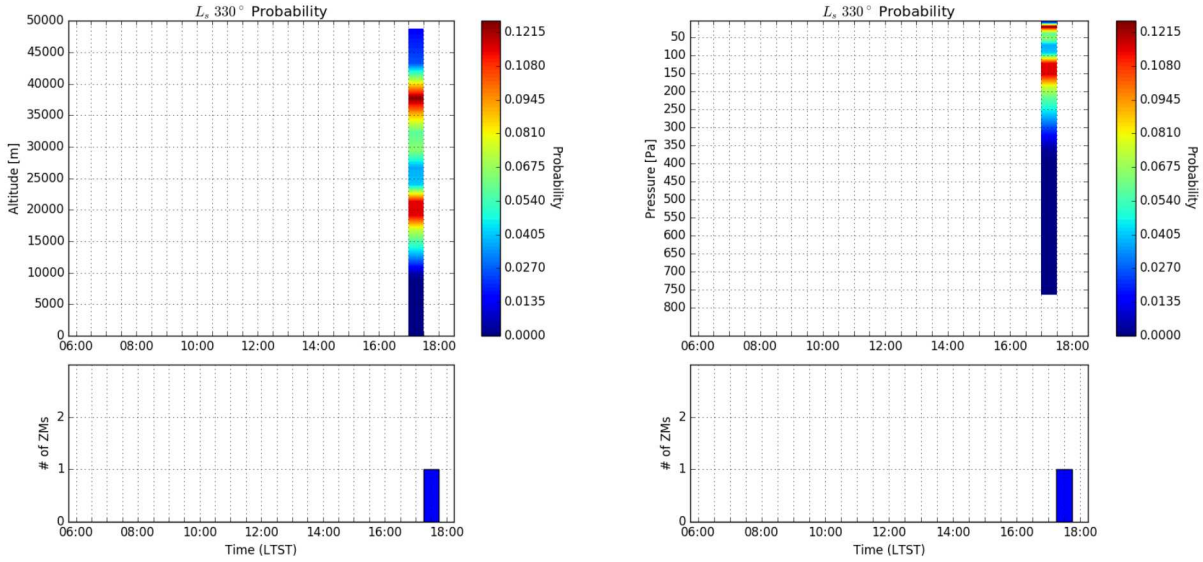

(a) (b)

Figure 3.13: Altitude probability graphs for L_s 330°, with one movie at 17:55 LTST. This season has a low population of movies with clouds because this is the dust season. The late afternoon shows clouds most likely to be at 20km and 38km. No clouds within the PBL or above the crater rim are probable in this season. More movies during this season, especially in the morning, would help show the true nature of clouds and their diurnal patterns.

Diurnally, cloud activity peaked in the morning and afternoon according to our histograms and Figure 2.5a. Additionally, there is a peak in the histograms between 15:00 and 16:30 indicating better movies during this time of sol. However, the majority of atmospheric movies are taken near 16:00 LTST which could account for this peak of movies seen in the histograms. (Kloos et al., 2018). Another reasoning for this peak stems from Tamppari et al. (2003) who argued that an afternoon peak in cloud activity is from uplifted dust from the surface as the atmospheric temperature increases throughout a sol. With the dust acting as Cloud Condensation Nuclei (CCN), clouds would form from water-ice nucleating onto the dust particle (Tamppari et al., 2003). During the morning peak, trends showed that cloud activity decreased towards midsol, which also is confirmed by our histograms. Atmospheric movies taken at Gale Crater ((Moores et al., 2015b), (Kloos et al., 2016; 2018)) show a decrease in cloud activity during midsol. Warmer temperatures would cause the clouds to dissipate from morning to midsol. Clouds in the morning are expected and were originally viewed through Hubble Space Telescope observations by Wolff et al. (1999).

A pattern in the contour plots are low probabilities between 20-40 km in Figures 3.3, 3.4, 3.8 and 3.9. This indicates that clouds would either form close to the surface or high in the atmosphere. However, the small number of movies outside the ACB season makes it difficult to select between these two hypotheses. The majority of clouds seen in atmospheric movies are taken during the ACB season, which is evident in our histograms. Figure 3.14 shows contour plots for the ACB season (L_s 60°, 90°, 120° and 150°) which will be the focus of this section.

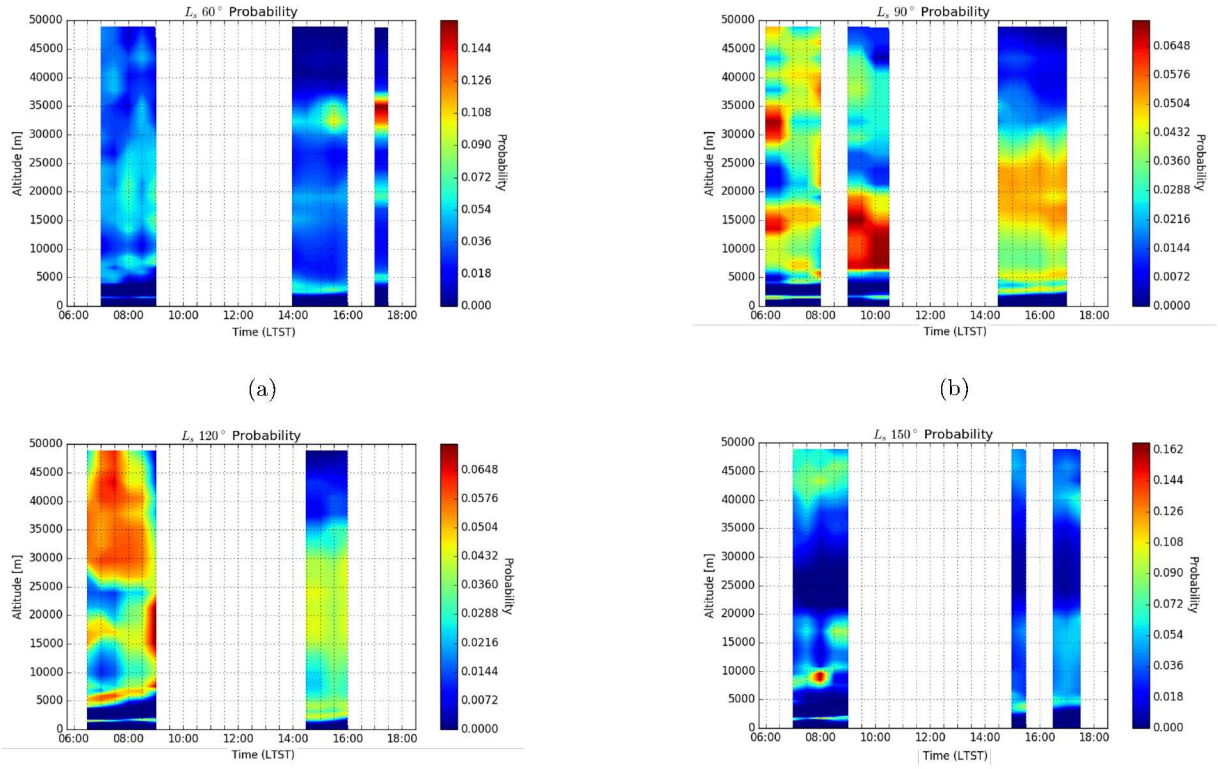

Figure 3.14: Altitude probability graphs for clouds during the ACB Season (L_s 60°, 90°, 120°, 150°). Every season in the morning shows multiple high probabilities throughout the atmosphere. Figures 3.14a, 3.14b and 3.14c show low probabilities above 35 kms in the afternoon but not Figure 3.14d. Instead, Figure 3.14d exhibits low probabilities between 20-40 km as seen in other seasons outside the ACB. The ACB at Gale Crater appears near L_s 45° and disappears around L_s 150° (Kloos et al., 2016). Each simulated season has movies $\pm L_s$ 15°, which places movies in L_s 150° outside the ACB. This may explain why Figure 3.14d shows similar patterns to simulations outside the ACB season. In every Figure, high probability exists just above the crater rim in both morning and afternoon results. Clouds most likely form here because of CCN getting into the lower atmosphere, allowing water-ice to nucleate, forming clouds (Tamppari et al., 2003).

During the ACB season (Figure 3.14) high altitude clouds (>35 km) are more probable in the morning when compared to the afternoon. The cooler atmospheric temperatures overnight could cause clouds to form

at higher altitudes. Towards the later part of the ACB season, low probabilities between 20-40 kms start forming. If clouds do exist at these altitudes, this indicates that mid-altitude clouds are not as common during the end of the ACB season. As noted in Tamppari et al. (2003), water-ice clouds diminish between L_s 140°-170° meaning a possible transition between the Northern to Southern dominant Hadley cell. During the aphelion season, general circulation models predicted a cross-equatorial Hadley cell in the Martian atmosphere (Haberle et al., 1993). First mentioned by Clancy et al. (1996), water-ice clouds are expected to form in the ascending branch of the Hadley cell and are responsible for the movement of water between the northern and southern hemispheres during aphelion. With the transition of the Hadley cells, this absence in the early and later part of the ACB could be evidence of this. When investigating seasons on either side of the ACB season, both L_s 30° and 180° show low probabilities between 20-40 kms, an indication that it could be due to the Hadley cell splitting into two relatively weak cells (Zurek, 1992). Evident in Figure 3.15, equinox shows two weak Hadley cells, while solstice shows one strong Hadley cell (Jakosky and Haberle, 1992). Martian solstice occurs at L_s 90° and 270°, during the two major seasons on Mars.

Another notable feature is a high-probable band under 5 km in the morning. The crater rim of Gale crater averages 2-3 kms from the bottom of the crater (Moores et al., 2015a). Clouds above the crater rim are expected because more dust is kicked into the atmosphere which then act as CCN. The more dust in the atmosphere, the easier clouds would form through nuceleation. As shown in Figure 3.16 from Moores et al. (2015b), night-time MRAMS simulations show air flowing down the north rim that encounters cold, stable air and is forced to jump up over the crater at altitudes between 3-5 km. This nighttime air flow rarely makes it to the crater floor, indicating a relatively dry crater as any water vapour that is forced into this hydraulic jump and flows over the crater (Moores et al., 2015b). Low altitude morning clouds could be explained by this jump.

Curiosity's location on Mars is along the edge of the dichotomy boundary. This boundary is the topographic division between the northern lowlands and southern highlands (Tanaka et al., 1992). The southern hemisphere is covered 60% by craters or lava flows that occurred early in Martian history (Tanaka et al., 1992). The northern hemisphere is considered newer compared to the southern hemisphere because of its

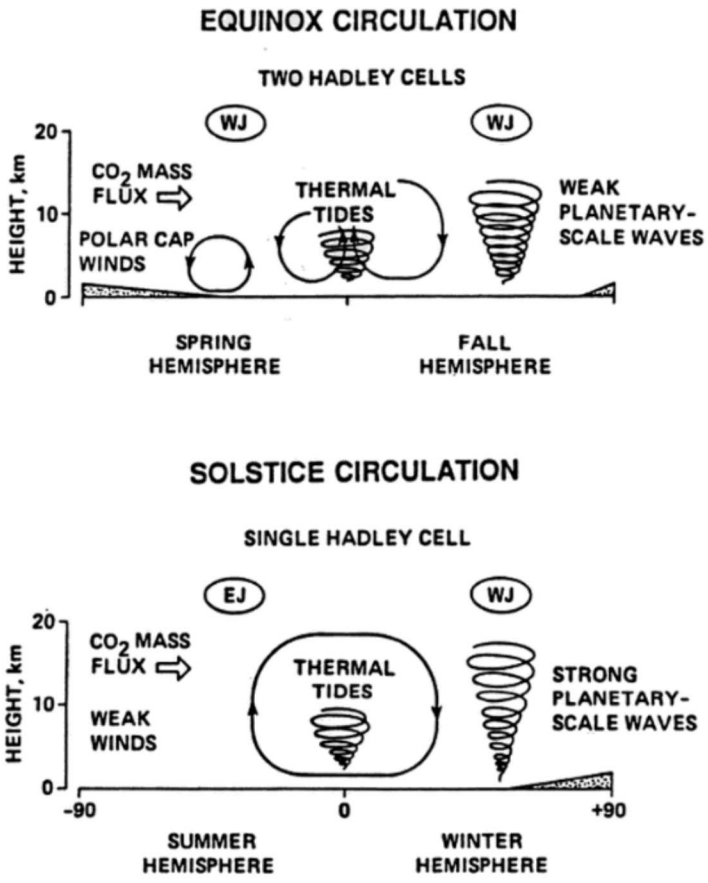

Figure 3.15: Diagram showing the difference in Hadley cell circulation over Mars' orbit (Jakosky and Haberle, 1992). The upper Figure shows two Hadley cells that formed during equinox while the lower Figure shows a single cross-equatorial Hadley during solstice.

smoothness and lack of craters (Tanaka et al., 1992). Gale crater is located within the highland-lowland boundary that is a large, irregular circle between the nothern lowland and southern highland (Tanaka et al., 1992), (Tyler and Barnes, 2013). Mesoscale modelling of circulation by Tyler and Barnes (2013) shows the dichotomy boundary playing an important role within Gale crater. Curiosity's location on the northern side of the crater allows shielding by Aeolis Mons against the strong convective flow from the south (Tyler and Barnes, 2013). Observed by Vasavada et al. (2012), Moores et al. (2015a), and Moore et al. (2016) a suppressed planetary boundary layer ranges from 1-2 kms in the crater while outside the crater, the PBL

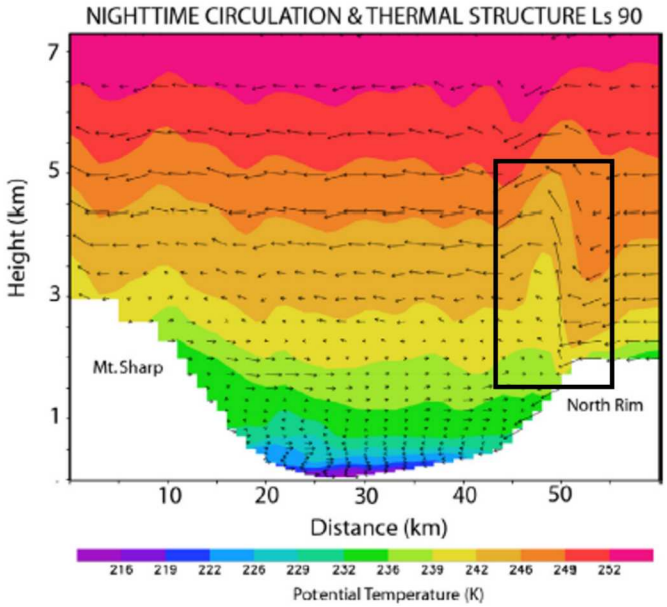

Figure 3.16: MRAMS simulations showing night-time circulation results over Gale crater. A hydraulic jump is seen at the North Rim when air flow enters from the northern rim. Unable to reach the crater floor due to dense air, it rises and flows across the crater rim carrying water or dust (Moores et al., 2015b). Therefore, Gale crater should be dry and if clouds form, they are most likely to be above crater circulation (Moores et al., 2015b).

ranges 8-10 kms. Clouds would be expected to form within these two layers. This is evident in Haberle et al. (2014) where evening pressure oscillations are caused by gravity waves where the horizontal wavelength is between 1.5-9.0 kms. This would be between the crater rim and PBL. To better support this, Clancy et al. (1996) measured low-altitude water vapour saturation during the ACB. Figure 3.14 shows high-probable altitudes at both ranges for all of the ACB modelled seasons.

By viewing our results over an entire MY, we can identify any trends that occur seasonally. Clouds on Mars are represented by two peak times, morning and afternoon. They will be analyzed individually. For each season, all probability values corresponding to each peak time will be averaged.

3.2 Seasonal Results

Figures 3.17-3.18 show average results over an entire MY for each season and corresponding histograms. Each histogram shows the total number of movies versus analyzed movies for that season. The ACB is noticeable in the histogram which shows higher analyzed ZMs. L_s 240° is an example of a season that had no movies with clouds distinguishable enough to be analyzed. The two peak times of Martian clouds are represented in figures 3.17-3.18 to find any diurnal changes over a MY. Morning ZMs are defined as any movie before 12:00 LTST and afternoon ZMs are any movie after 12:00 LTST.

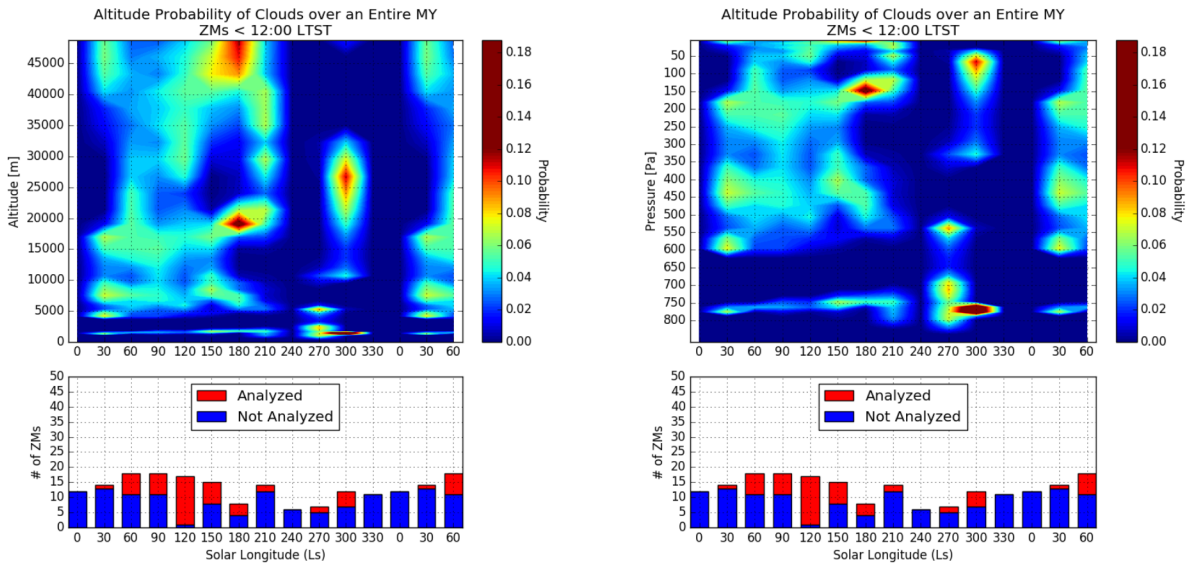

(a) (b)

Figure 3.17: Altitude probability graphs for morning ZMs over an entire MY. Each season that has multiple movies is averaged for ZMs with an observation time before 12:00 LTST. High altitude clouds are most probable in the morning, except for later seasons in the MY, possibly due to dust storms that frequent these seasons. A high-probable band at the crater rim (2-3 km) is evident in every season. The low probability between 20-40 km is evident in L_s 0°, 30°, 150°, 180°, 270°-330°. Advocating for more ZMs outside the ACB season would increase the reliability of those results.

As noted in section 3.1, Figure 3.17 shows a high-probable band just above the crater rim. This is evident in all seasons with analyzed ZMs. Clouds below the PBL are also evident in all seasons. During the later part of the MY, Figure 3.17 shows lower probability for high-altitude clouds in the morning. The absence of clouds between 20-40 km is also seen as compared to our diurnal results. This absence is evident outside of the ACB season and during seasons where Hadley cells transition from one cross-equatorial cell to two weak cells. During L_s 0°-30°, Mars approaches aphelion causing the ACB to form. During 150°-180°, the ACB has dissipated and the next seasonal phase is a dusty, cloud-free atmosphere (Smith, 2004). During perihelion, the atmosphere warms and more dust is circulated. High altitude clouds during L_s 210° will be examined to determine which altitudes are most-probable. L_s 210° is a unique season showing high-probable clouds through most of the Martian atmosphere, except between 5-10 kms. This would correspond to below the PBL which was more probable for every other season. This season could perhaps produce clouds at higher altitudes because circulation at lower altitudes is occurring during the start of dust-storm season.

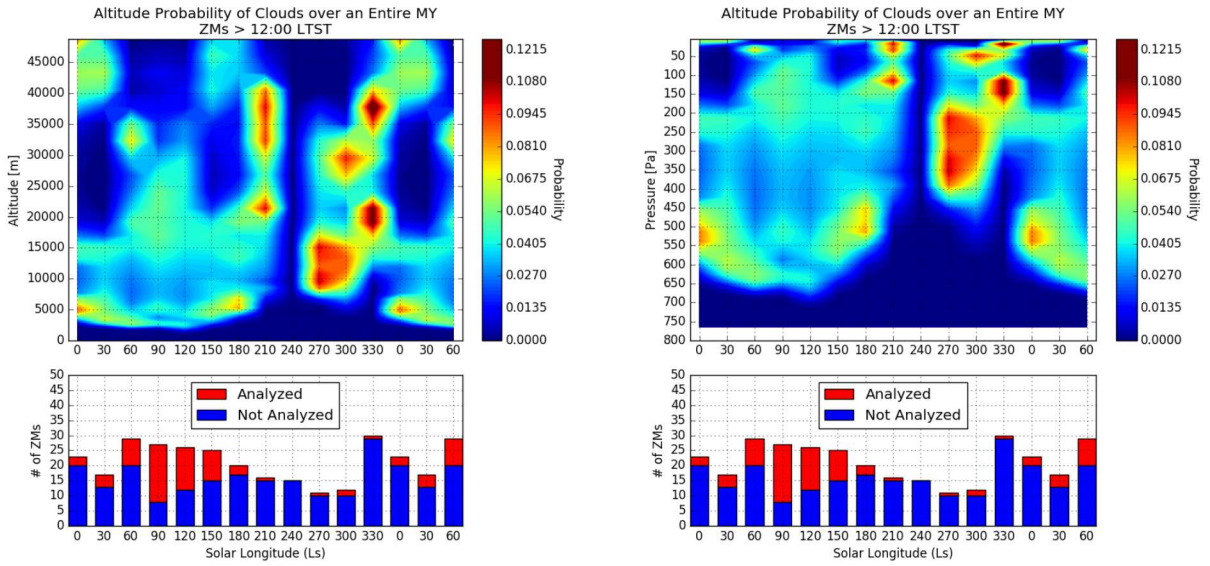

(a) (b)

Figure 3.18: Altitude probability graphs for afternoon ZMs over an entire MY. Each season that has multiple movies is averaged for ZMs with an observation time after 12:00 LTST. Low altitude clouds, between the crater rim and PBL are evident in all seasons except later in the MY L_s 210°-330°. During the ACB season, a high-probable band exists between 15-30 km, with low probabilities for altitudes higher than 37 km. Low probabilities between 20-40 km are visible for L_s 0°-30°, 150°-180° which are seasons in Figure 3.17 that also show this low probability pattern for morning results. According to simulated results, clouds are less likely to form at altitudes between 20-40 km during L_s 0°-30°, 150°-180° in both the morning and afternoon.

Diurnally, afternoon ZMs do not show high-probable values for high altitude clouds when compared to morning ZMs. Figure 3.18 shows a strong feature 15-30 km above the surface in the ACB season. This high-probable feature could be related to the movement of water-ice from the northern pole to the southern pole during aphelion as seen through TES observations (Smith, 2004). Figure 1.3 shows the highest amount of ice during the ACB season. This is also confirmed through a 3D Martian General Circulation Model (MGCM) by Montmessin et al. (2004), that showed the migration of water vapor from the North pole to the South occurring in the ACB season. Gale Crater is near the equator (4.5° S) where the water vapour column has higher abundances as it travels towards the south during aphelion.

This mid-altitude high-probable feature could be represented by thermal tides that have been observed in the middle atmosphere. Thermal tides are global oscillations in wind, pressure and temperature that create temporal variability in the atmosphere (**?**). A Sun-synchronous diurnal tide for Mars was hypothesized by Lee et al. (2009). Comparing spectral analysis from MCS retrievals and a MGCM showed dramatic differences between night and day temperatures (Lee et al., 2009). This difference drives large amplitude oscillations within the atmosphere and causes daily varying pressures and winds (Lee et al., 2009). By using radio occultation measurements by the Mars Global Surveyor (MGS) and Mars General Circulation Model (MGCM) simulations, Hinson and Wilson (2004) found thermal tides that coupled to cloud formation. Cloud formation is correlated to temperature where water-ice condenses when water vapor partial pressure is greater than the saturation pressure (Heavens et al., 2010). Lower atmospheric temperatures cause their formation. As shown in Figure 3.19, temperature deviations by thermal tides are seen to change diurnally. Corresponding to the MRAMS altitude range, negative temperature deviations are seen in the lower and upper atmosphere in the morning, but mid-altitude in the afternoon. When comparing to our ACB results, higher altitude clouds are more probable in the morning than in the afternoon. This theory could explain this change in altitude between the morning and afternoon.

Additionally, Figure 3.20 shows the diurnal temperature structure where the lower temperatures would indicate higher chance of cloud formation. Each line shows several low temperature points, similar to the several high-probable regions in our morning results (Figure 3.17). For the afternoon, the lowest temperature

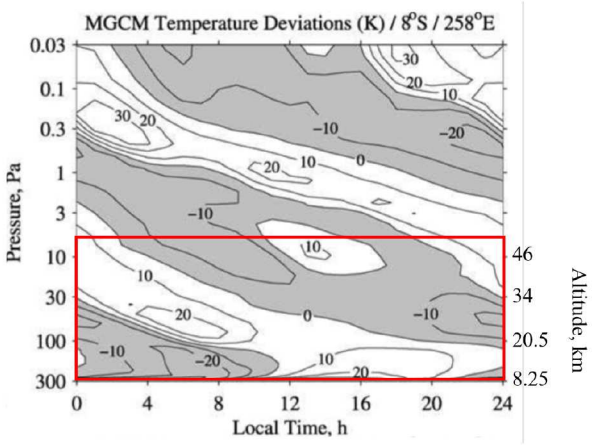

Figure 3.19: Diurnal temperature deviations caused by thermal tides at 04:00 simulated by the MGCM (Hinson and Wilson, 2004). Each contour level is 10 K where a darker shade indicates negative values. The simulation was located at 8°S, 258°E. The range of altitudes corresponding to MRAMS is shown in the red box with altitude values put on the diagram.

is found at a single altitude, around 20 km. In Figure 3.18, a high-probable band exists at similar altitudes during the ACB. The difference in altitudes between the morning and afternoon figures (3.17, 3.18) can be explain through thermal tides where water-ice condenses near minimum temperatures corresponding to the anti-nodes of the diurnal tide (Heavens et al., 2010).

During the ACB season, afternoon clouds are confined to altitudes below 35 kms. However, the morning resulted in more high-probable clouds above 35 kms. This diurnal difference could be another indication that thermal tides are present. Several high-probable areas are located below the PBL, as expected. Interestingly, during the dusty seasons (L_s 210°-330°) the low altitude high-probable areas were located above 10 kms and not within the PBL. Circulation within the PBL and Gale crater during dust-storm season could be the reasoning for this. Any clouds that do form during this time would be confined to higher altitudes.

Due to high uncertainties from models, our results need to be confirmed. Section 3.3 discusses using limb measurements by the Mars Climate Sounder (MCS). By plotting the water-ice extinction, the altitude of clouds can be determined. However, MCS is limited to altitudes above 10 kms and afternoon measurements.

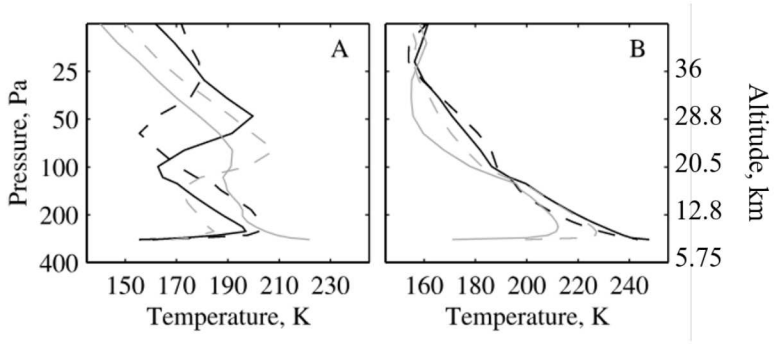

Figure 3.20: Diurnal thermal structure simulated by the MGCM at the same location as Figure 3.19. *A* demonstrates night-time simulations while *B* demonstrates afternoon simulations. For *A*, the dashed black line corresponds to 01:00, solid black 04:00, dashed grey 07:00 and solid grey 10:00. For *B*, dashed black corresponds to 13:00, solid black 16:00, dashed grey 19:00 and solid grey 22:00.

Section 3.4 correlates wind velocity between two atmospheric movies to determine the exact altitude of clouds above Gale crater. Shadows moving across Aeolis Mons can be used to find their velocity using geographical referencing. By pairing with a ZM, comparison to the angular wind velocity provides altitude. Using this method will aid in testing MRAMS.

3.3 Mars Climate Sounder (MCS) Results

Atmospheric models produce high uncertainties as we are still exploring our planetary neighbour. Therefore, options must be explored to help confirm probability results from MRAMS. This includes using data from the Mars Climate Sounder (MCS) onboard the Mars Reconnaissance Orbiter (MRO).

Launched on the Mars Reconnaissance Orbiter (MRO) in 2005, the Mars Climate Sounder (MCS) is an infrared radiometer used to characterize the Martian atmosphere. MCS continuously measures the atmosphere using limb and nadir viewing (McCleese et al., 2007). The limb of a planet is defined as the edge of the atmosphere and nadir measurements are made directly below the spacecraft. Limb measurements have a 5 km vertical resolution and 200 km horizontal resolution, sacrificing horizontal resolution but obtain the best vertical resolution (McCleese et al., 2007).

Consisting of two telescopes with a 4.3° FOV, measurements are made in nine spectral bands as shown in Table 3.1. Telescope A corresponds to channel numbers A1-A6 which measure in the visible and mid-IR while Telescope B corresponds to channel numbers B1-B3 that measure in the far-infrared (McCleese et al., 2007). Three different viewing directions are used to observe the atmosphere in the limb; the surface at nadir for four seconds then forward limb for 16 seconds and lastly the space above the forward limb for four seconds (McCleese et al., 2007). The viewing of space above the limb is used for calibration while the nadir view is used to improve retrievals of near-surface atmospheric properties because of its higher horizontal resolution (McCleese et al., 2007). This three-step observation is done every 34 seconds to have an atmospheric profile every 110 km (1.86° latitude).

In a Sun-synchronous orbit, MCS passes at 03:00/15:00 LTST and does "off-track" observations that can range ±2 hours from the nominal orbit (Kleinböhl et al., 2017). Kleinböhl et al. (2017) apply a two-dimensional radiative transfer scheme to temperature, dust and water ice opacity retrievals from MCS. Kleinböhl et al. (2017) assume spherical symmetry and the temperature or aerosol content is the same within that atmospheric layer. The "off-track" observations, as shown in Figure 3.21, describe observation geometries used to improve accuracy of the retrievals. However, if a measurement is an on-planet view, the two-dimensional radiative transfer scheme is unavailable. This is due to temperatures differing on opposite sides of the tangent point in the limb path (Kleinböhl et al., 2017). The radiative transfer equation can be found by assuming the Source function is represented by a homogeneous surface brightness temperature, which was modified into the code (Kleinböhl et al., 2017).

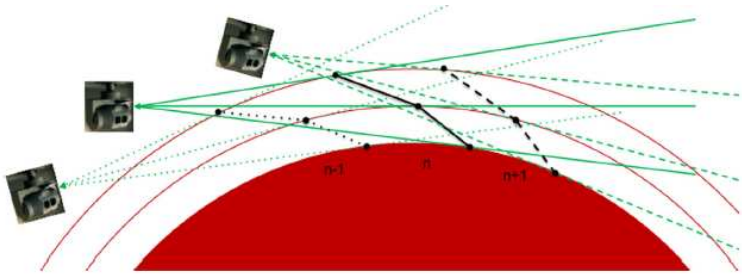

Figure 3.21: Diagram showing the three consecutive limb views by MCS. The red circles around the planet indicate layers of the atmosphere. Dotted, solid and dashed lines show limb paths for measurements n-1, n and n+1 (Kleinböhl et al., 2017). Black lines show atmospheric profiles measured during limb measurements.

The 202 profiles used in this study range between 13:00 and 17:00 LTST and were provided by Scott Guzewich at the Goddard Research Centre. The large horizontal resolution means that the profiles corresponding to Gale Crater are located between $-6.3°$S to $-3.8°$S and 135°E to 140°E (Guzewich et al., 2017). All retrievals used the two-dimensional radiative transfer algorithm as described in (Kleinböhl et al., 2017).

A constraint of limb observations by MCS is the inability to measure ice extinction below 10 kms. This poses a problem when confirming results as it will not be possible to confirm any of results that show clouds within the crater or PBL that is evident in Figures 3.17 and 3.18. Due to its sun-synchronous orbit, limb

Table 3.1: Table showing the nine different channels measured by MCS. For cloud retrievals, channels B1-B3 would be used (McCleese et al., 2007).

Telescope/ Channel Number	**Band Pass** $\mathbf{cm^{-1}}$	**Band Center** μ**m**	**Measurement Function**
A1	595-615	16.5	Temperature (20-40 km)
A2	615-645	15.9	Temperature (40-80 km) Pressure
A3	635-665	15.4	Temperature (40-80 km) Pressure
A4	820-870	11.8	dust and condensate extinction (0-80 km)
A5	400-500	22.2	Temperature (0-20 km) dust and condensate extinction (0-80 km)
A6	3300-33000	1.65	Polar radiative balance
B1	290-340	31.7	Temperature (0-20 km) dust and condensate extinction (0-80 km)
B2	220-260	41.7	Water Vapour (0-40 km) dust and condensate extinction (0-80 km)
B3	230-245	42.1	Water Vapour (0-40 km) dust and condensate extinction (0-80 km)

measurements at Gale Crater are only in the afternoon. Afternoon results shown in Figure 3.18 will be compared to confirm high-probable altitudes.

By averaging all MCS profiles by season and plotting similar to our probability graphs, we can compare if any high-probable afternoon altitudes match measured values. This will be able to exclude results where MCS does not see clouds. Figure 3.22a represents ice-extinction MCS profiles and 3.22b shows our afternoon probability results originally shown in Figure 3.18.

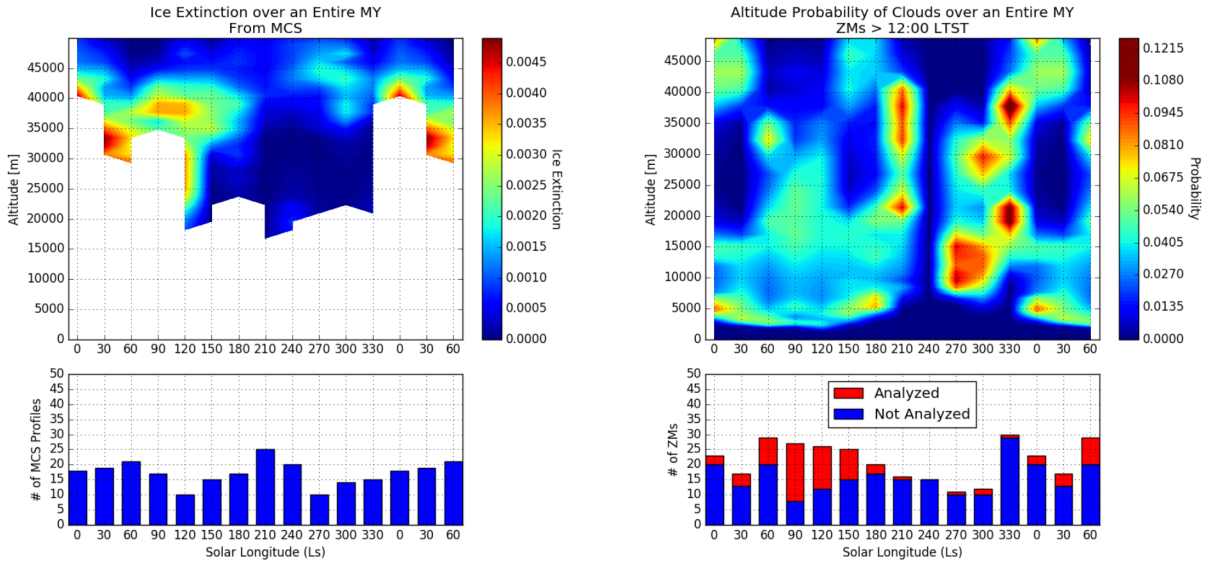

(a) (b)

Figure 3.22: MCS data (Figure 3.22a) will be compared to MRAMS afternoon results (Figure 3.22b) to try to exclude probabilities that may not be representative of actual cloud. MCS profiles provide the ice-extinction throughout the atmosphere above Gale crater which shows the altitudes of clouds. For L_s 210°, Figure 3.22a does not show any ice-extinction in the middle atmosphere, but Figure 3.22b shows high probability of clouds at 22 km and 30-40 km. The probabilities in Figure 3.22b would be eliminated from that season because of no clouds seen at the same altitudes by MCS in Figure 3.22a. Results from MCS agreed with MRAMS for the ACB season where ice-extinction was observed between 20-40 kms.

The ACB season has high-probable altitudes in the same region as MCS, between 20-35 kms. This is in

agreement with results seen by Lee et al. (2009), Heavens et al. (2010; 2011). High altitude clouds at 40 kms are measured for both L_s 0° and 30° which is in agreement with our results. For altitudes above 45 km, MCS profiles only show L_s 270° and 300°. Figure 3.18 does not show clouds above 45 kms for L_s 270° and 300°, but instead at L_s 30°, 150° and 180°. These high-probable altitudes can be excluded because of the mismatch for clouds above 45 km between Figure 3.22b and 3.22b.

Limited amount of water-ice were measured by MCS between L_s 210° and 330°. This agrees with Smith (2004) where minimal cloud cover is seen in the tropics during the perihelion season. Clouds are more likely to form above the PBL according to Figure 3.22b if we exclude any high-probable values above 20 kms as seen by MCS. However, the limited amount of analyzed movies in this season poses a problem comparing results. Not enough of a sample is available to be conclusive in our comparison. Capturing more clouds during this season would increase confidence.

Lastly, a similarity is the absence of water-ice between 20-35 kms between L_s 150° and 180°. This absence of clouds was first commented on in the previous section which is confirmed in the MCS results.

Unfortunately, we cannot confirm our morning results and altitudes lower than 10 kms due to MCS constraints. To determine exact altitudes of clouds over Gale crater, shadows moving over Aeolis Mons is compared to clouds seen in ZMs overhead as explored in Section 3.4.

3.4 Shadows over Aeolis Mons

To better constrain the altitude of clouds over Gale Crater, a dust-devil movie is repurposed for viewing shadows moving across Aeolis Mons. Pointing eastwards using the Navcam, this observation looks for dust-devils at the base of Aeolis Mons including shadows that were recently captured moving across the mountain. Several types of dust-devil movies exist that can capture these shadows and their descriptions is shown in Table 3.2. The name of a dust-devil movie used for this analysis is a Cloud Height Movie (CHM). An example of a CHM is shown in Figue 3.23.

Table 3.2: Description of the different type of dust-devil movies associated with CHMs. The 15set observation has a long (more frames) and short (less frames) version. Another difference is the frame size, where 15set_short gets a larger FOV, but shorter number of frames. 21frame movies were easier to obtain because of their shorter timespan.

Observation Name	**# of Frames**	**Duration**	**Frame Size** (pixel)
15set_long	30	30 minutes	128×512
15set_short	15	30 minutes	256×1024
21frame	5	5 minutes	256×1024

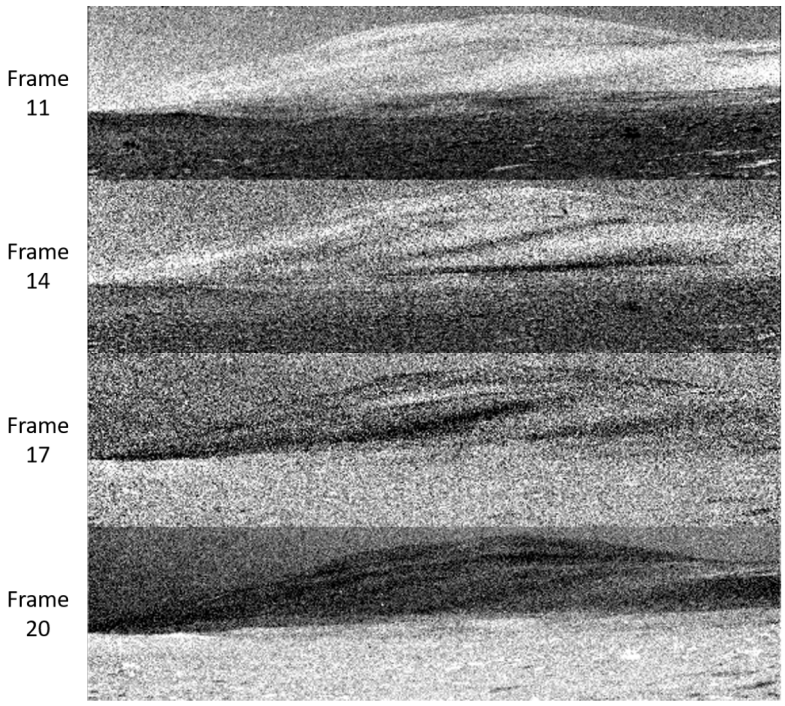

Figure 3.23: Shadows visible moving across Aeolis Mons for the first time on sol 1787. This movie was taken starting at 15:07 LTST for a 30 minute duration pointing eastward at 103.1° azimuth. Dark streaks identified as shadows from clouds are seen between frames 11-20 out of 30 frames. This is paired with a ZM (Figure 3.27) that observes the same clouds directly above the rover.

Pairing a ZM with this observation allows a comparison between angular wind velocity from the ZM and absolute velocity from the CHM. Similar processing as ZMs, the CHM is followed by eye and marked where the shadow starts and ends. Figure 3.24 shows an example of a shadow that was followed in the sol 1787 CHM. A Matlab code, supplied by Casey Moore at York University, measures distances from the rover through a detailed elevation map known as a Digital Terrain Model (DTM) and is used to create an outline of Aeolis Mons (Figure 3.25). Horizontal and vertical distance can be found by overlaying the outline over Figure 3.24.

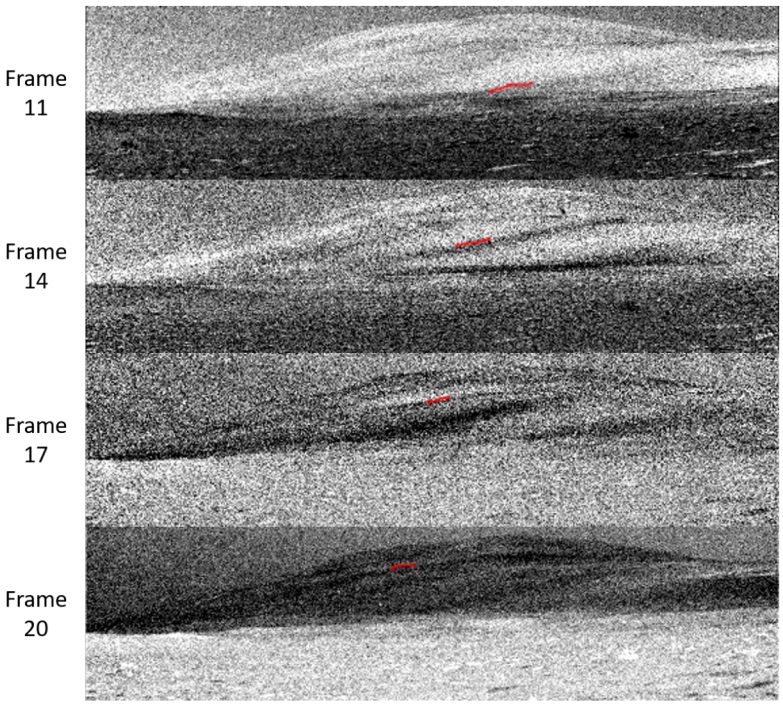

Figure 3.24: Shown in red lines, the shadow is marked moving across the mountain between frames 11 and 20. The distance the shadows move can be estimated through geo-referencing to calculate the absolute wind velocity of the clouds causing the shadows.

Corresponding to 64 pixels, Aeolis Mons is used in reference to determine pixel location of shadows in Figure 3.25. Black lines in Figure 3.25 are the shadow locations as seen by Frame 11 and 20 in Figure 3.24. The pixel difference between the start and end of the appeared shadow is used with the approximate height

of Aeolis Mons (5.5 km) to find the vertical distance. The horizontal distance would be the distance the clouds move. Figure 3.26 sets up the problem with trigonometry. Assumptions include Aeolis Mons being a perfect triangle and the sun being directly overhead. Section 5 discusses how this work will be expanded to accurately measure the altitude of clouds. Increasing our CHM population will also help refine results.

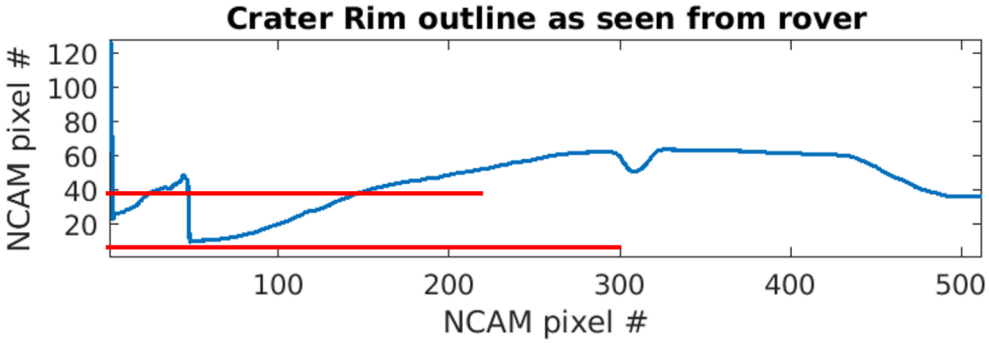

Figure 3.25: Aeolis Mons outline produced by Matlab code used to look at the crater rim outline. The red lines show the location of the beginning (lower) and end (upper) location of the shadows found by overlaying a marked CHM (Figure 3.24). In this example, the pixel difference is 32 pixels $\pm$ 5 pixels.

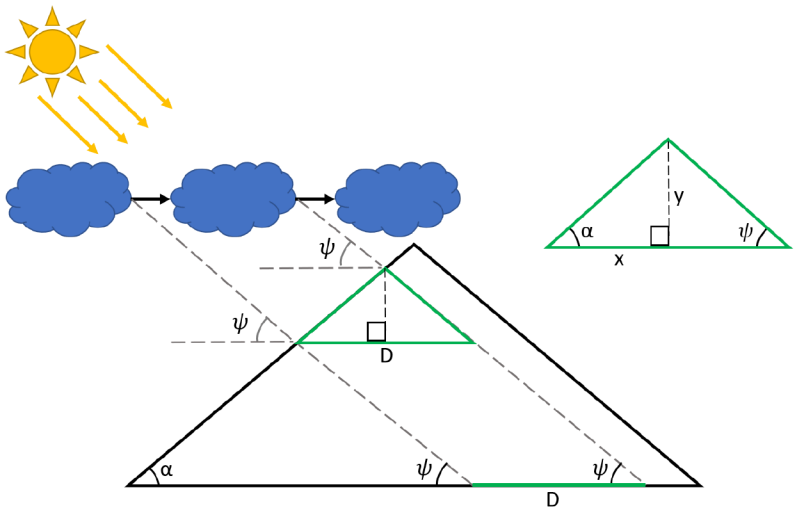

Figure 3.26: Diagram showing the analysis for absolute velocity from CHMs. The distance the clouds move (D) is calculated using the green triangle and Equation 3.1. Solar elevation (ψ) is provided with each CHM and used for angle calculation. Based on cloud movement, x is the horizontal distance and y is the vertical distance. y is calculated by the height of Aeolis Mons (5.5 km) and the number of pixels the clouds moved as shown in Figure 3.25. x is solved using Equation 3.2 where α is the slope angle of the mountain, calculated by estimating the base of the mountain through an elevation map. With a total estimated base width of 32 km, α is solved with Equation 3.3. Plugging these values into Equation 3.1, the absolute velocity is calculated by dividing D and the duration of frames that showed the shadows.

$$D = x + \frac{y}{tan(\psi)} \tag{3.1}$$

$$x = \frac{y}{tan(\alpha)} \tag{3.2}$$

$$\alpha = atan\left(\frac{5.5km}{16km}\right) = 18.97^{\circ} = 0.331rad \tag{3.3}$$

Table 3.3 show results from the calculation into the absolute velocity of overhead clouds seen through shadows across Aeolis Mons. Both vertical and horizontal distances are provided. Absolute velocity in

meters per second is calculated by dividing the horizontal distance by the duration between frames showing the shadows. The angular wind velocity is found through the same method described in Section 2 and divided by the total length of the ZM for a unit of degrees per seconds. The marked ZM showing a cloud feature followed is shown in Figure 3.27. An altitude is calculated with trigonometry as shown in Figure 3.28.

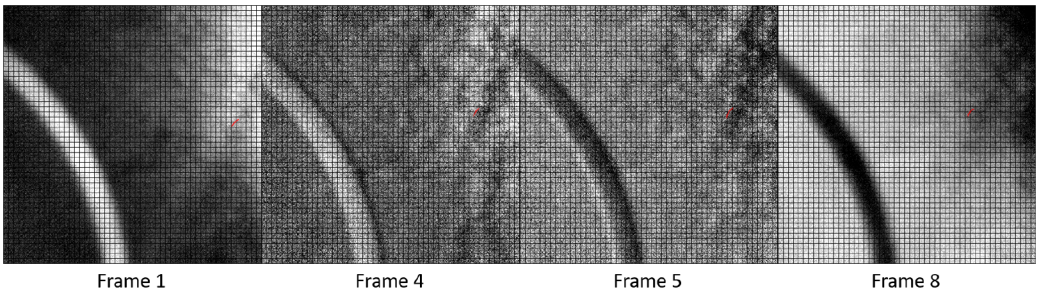

Figure 3.27: Mean-subtracted grid frames 1,4,5,8 for sol 1787. This ZM was taken after the CHM, where clouds seen in these frames are assumed to be the same causing the shadows on Aeolis Mons in Figure 3.23. Marked by a red line, a feature is followed to determine angular distance.

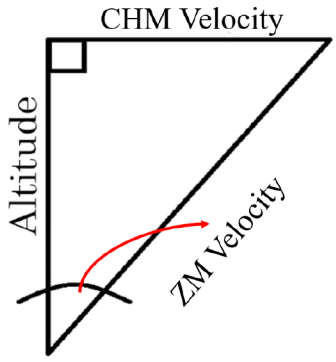

Figure 3.28: A diagram showing the trigonometry used to solve for the altitude of clouds seen in a CHM and paired ZM. The CHM velocity corresponds to the absolute velocity while the ZM velocity is the angular velocity. The altitude is calculated through Equation 3.4.

$$\begin{aligned} \text{Alt.} &= (\text{CHM vel.})/(tan(\text{ZM vel.})) \\ &= (\text{Absolute vel.})/(tan(\text{Angular vel.})) \end{aligned} \tag{3.4}$$

Table 3.3: Values found for shadows moving across Aeolis Mons in CHMs. Figure 3.26 outline how the vertical distance (y) and horizontal distance (x) were found. The altitude of clouds seen in the ZM and through shadows in the CHM is calculated by trigonometry shown in Figure 3.28. Errors are calculated based on average errors for each example. Error in absolute velocity takes into account the pixel difference error (± 5 pixels). For angular velocity, the error found for angular distance (± 2°) is divided by the average ZM length (230 s). Altitude error takes into account both absolute and angular velocity errors. The MRAMS probability shows the percentage the model predicts clouds at the altitude found from the CHM analysis.

Sol	L_s	y **(m)**	x **(m)**	**Solar Elevation** (°)	**Absolute Velocity (± 5 m/s)**	**Angular Velocity (± 0.009 °/s)**	**Altitude (± 3.5 km)**	**MRAMS Probability** (%)
1787	48°	2750	8306	34.06	21.33	0.029	40.9	30
1878	89°	515.6	1557	45.18	41.40	0.068	34.8	47
1959	127°	1375	4153	46.79	42.87	0.047	52.1	N/A
1976	135°	1289.1	3893	11.94	39.49	0.038	59.8	N/A
1980	137°	1718.8	5191	18.69	27.54	0.051	30.7	19
1980	137°	1804.7	5450	16.52	24.91	0.051	27.8	14
1990	142°	1804.7	5450	40.72	20.23	0.070	16.5	46

The altitudes in Table 3.3 are compared to probability graphs for individual sols simulated by MRAMS for the same time of sol as shown in Figures 3.29-3.32. If the red box lines up with high probability from MRAMS, the reliability of the model increases as it matches with approximate observed values. The centre of the box is the calculated altitude with ± 3500 km error in altitude and ± 0.025 (2.5%) error in probability. For sol 1959 and 1976, there is no MRAMS probability graph to compare as the altitude measured is outside of the 0-50 km altitude range of MRAMS. The altitudes calculated in this section are also compared to the MRAMS afternoon probability results and shown in Figure 3.33.

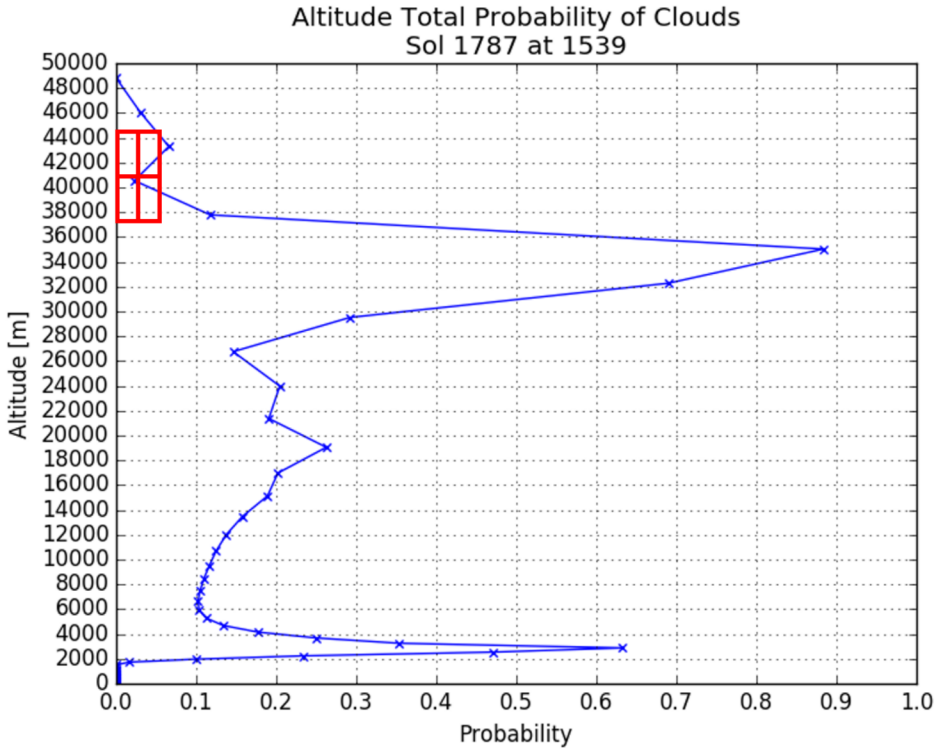

Figure 3.29: Altitude probability graph for sol 1787. The red box shows the location of the altitude calculate through a CHM on the same sol and time. The MRAMS probability at this altitude is below 10%, predicting low probabilities of clouds. The highest probability for this example is predicted at 35 km and 3 km, not matching with the calculated 40.9 km from Table 3.3.

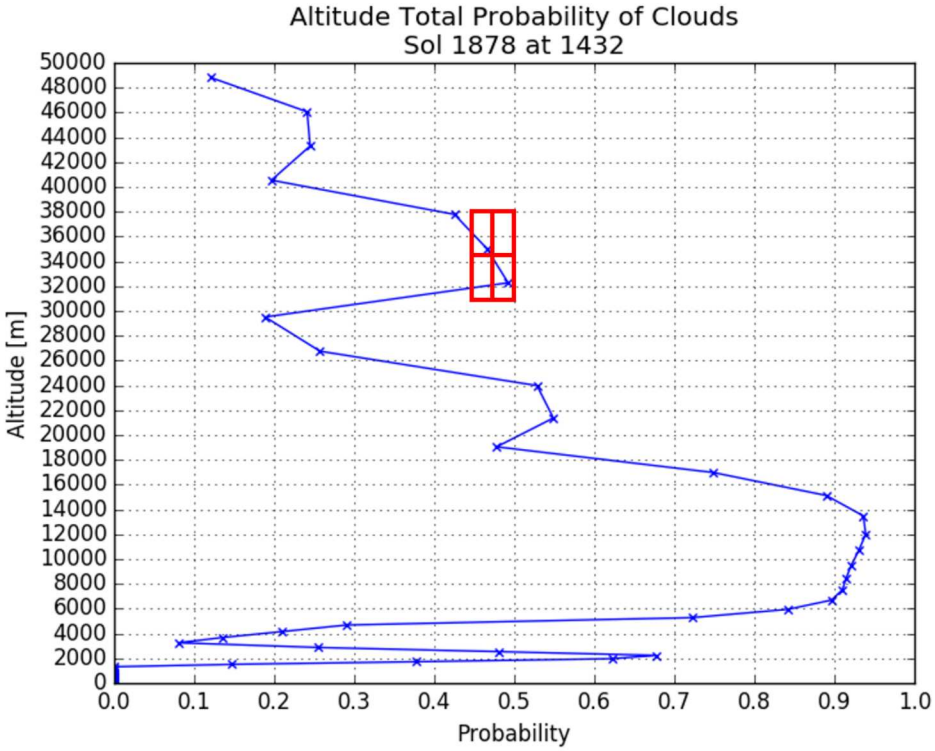

Figure 3.30: Altitude probability graph for sol 1878. The altitude calculated for sol 1878 is 34.8 km. MRAMS predicts 47% chance of clouds at that altitude. The highest probabilities for this sol exist between 6-16 km.

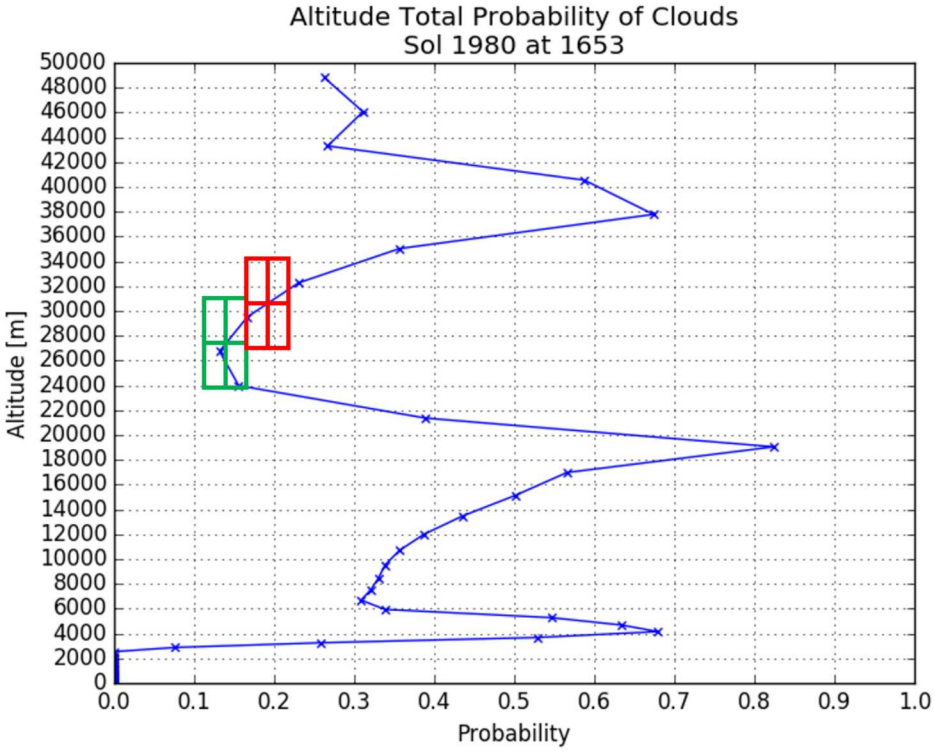

Figure 3.31: Altitude probability graph for sol 1980, with two separately measured shadows. The red box shows the first altitude (30.7 km) and the green box shows the second altitude (27.8 km). These altitudes are both below 20%, indicating that the model may not be accurate as predicted. More examples are needed to grow a larger population with this data set and accurately compare cloud altitudes to MRAMS probabilities. This sol has 80% chance of clouds at 19 km and 70% chance at 38 km and 4 km.

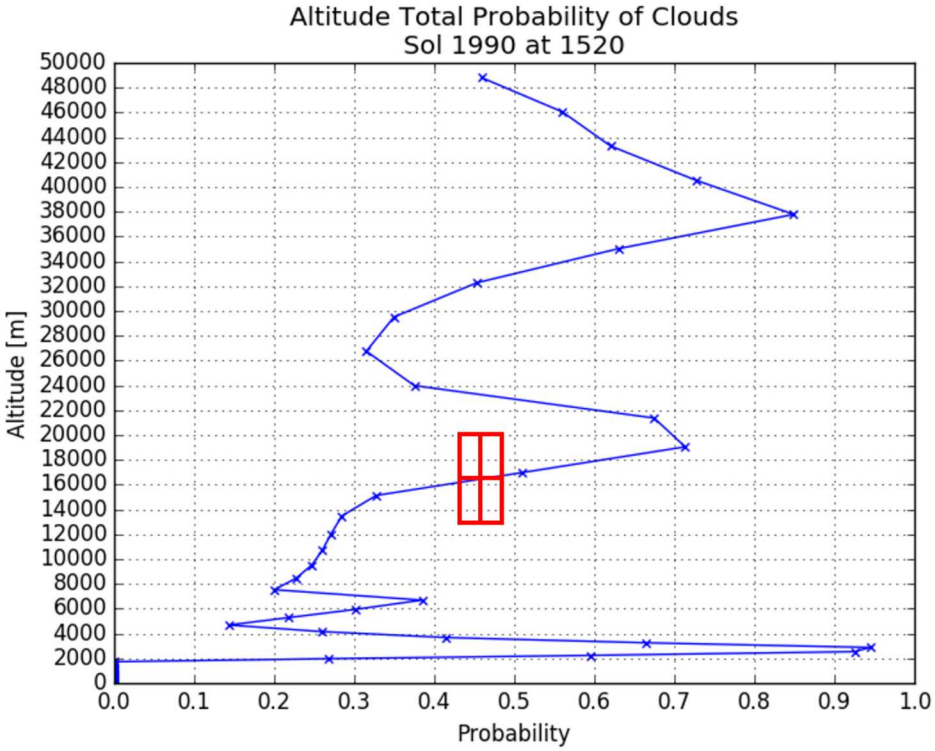

Figure 3.32: Altitude probability graph for sol 1990 with a calculated altitude at 16.5 km. This altitude corresponds to a probability of 46%. The highest probabilities for this sol are 3 km, 19 km and 38 km.

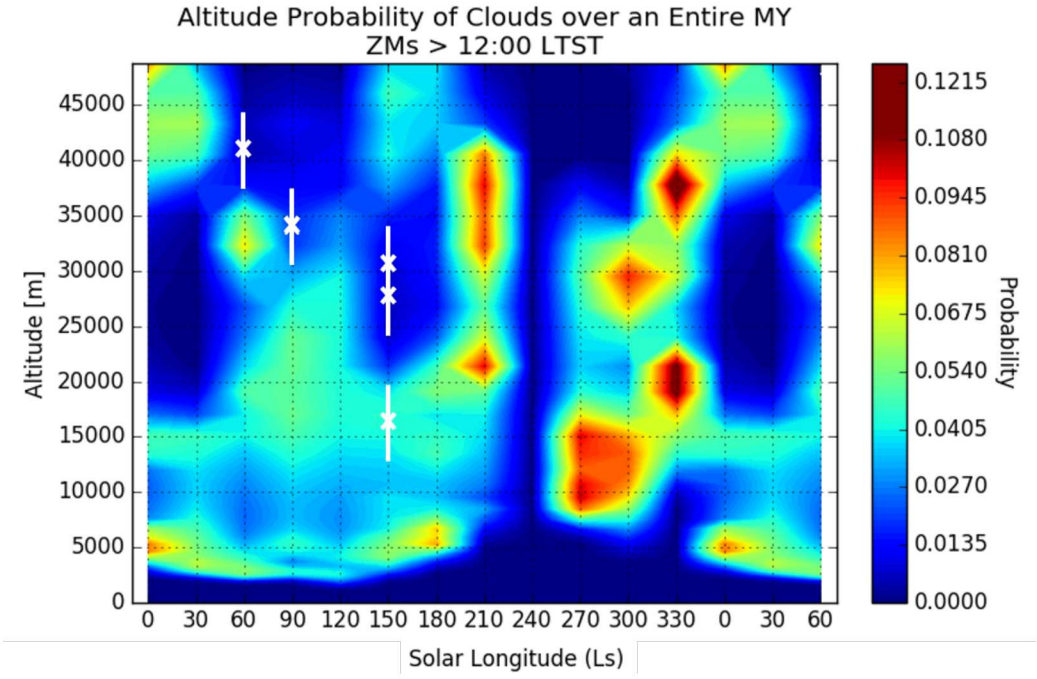

Figure 3.33: The altitudes calculated through shadow movement across Aeolis Mons (Table 3.3) is compared to afternoon probability results shown originally in Figure 3.18. The majority of the altitudes calculated do not match up with high probability altitudes predicted through MRAMS simulations. For L_s 120°, the altitudes calculated were higher than the 50 km altitude domain of MRAMS.

Altitudes calculated through analysis of CHMs had a wide range throughout the atmosphere, with some higher than the MRAMS altitude range. Higher altitude clouds were measured for earlier seasons compared to later as shown in Table 3.3. In diurnal and seasonal MRAMS results, clouds were predicted below the PBL, however, this was not consistent with calculated altitudes. Sol 1959 and 1976 are unable to be confirmed with MRAMS probabilities as their altitudes were measured above the maximum MRAMS altitude (50 km). All examples only agreed with probabilities lower than 50%. This may indicate model inconsistencies and more of a population would help compare model results and reliability. It could be argued that MRAMS does not represent high enough altitudes. With two CHM analysis (sol 1959 and 1976) showing altitudes above the MRAMS domain (50 km). Acquiring more CHMs in the next ACB will help with our analysis of clouds above Gale crater. Morning probabilities are unable to be confirmed through other methods because both MCS profiles and CHMs are taken in the afternoon.

4 Conclusions

Altitudes of clouds above Gale crater have been estimated through correlation between observed values from atmospheric movies taken by Curiosity and modelled values calculated by the atmospheric model MRAMS. By following features in Zenith Movies (ZMs), an angular distance is found through the pixel size and Navcam FOV which is compared to wind velocities calculated by MRAMS. The half-normal probability distribution is used to determine the probability of cloud altitudes. Diurnal and yearly results can be assessed for any patterns.

Diurnal results showed a difference in altitudes between morning and afternoon results. Higher altitude clouds are more probable in the morning rather than the afternoon which could be caused by cooler temperatures overnight. Morning probabilities showed high probability of clouds at altitudes under 5 km, corresponding to the crater rim. Clouds are expected at this altitude as dust is more likely to act as Cloud Condensation Nuclei (CCN) and form clouds (Tamppari et al., 2003). Within the Planetary Boundary Layer (PBL), at 10 km, is also expected to yield high probability of clouds. This is evident in both morning and afternoon results. Low probabilities between 20-40 km are noticed in several seasons indicating that either high altitudes or low altitudes are more probable. More ZMs during the morning in seasons outside the ACB season would the conclusion of these results.

Morning seasonal results show higher altitude clouds in early MY seasons while lower altitudes are more probable in later MY seasons. Low probabilities between 20-40 km seen in diurnal results are also shown during L_s 150°-180°, 240°-30°, during dustier seasons. High probability at the crater rim, between 2-3 km, is seen in every season. Clouds under the PBL are also common in the morning. The ACB season shows

multiple altitudes that are most probable for clouds. Advocating for more morning ZMs throughout the MY would help increase the credibility of this data.

During the afternoon, seasonal results show high probability for low altitude clouds during the ACB season, but not for seasons during the dust season. Clouds are expected to form closer to the surface during the afternoon because warmer temperatures kick dust into the atmosphere acting as CCN (Tamppari et al., 2003). However, during the dust seasons (L_s 210°-330°) no clouds are expected below the PBL (10 km), which is unexpected. Low amount of movies analyzed in these seasons might also explain this, where more afternoon ZMs should be advocated to better constrain the results. The ACB season shows most probable altitudes for clouds at the crater rim, under the PBL and between 15-30 km. No clouds are probable higher than 35 km during the ACB season. The high probable altitude between 15-30 km may be explained through thermal tides, observed in the middle atmosphere through model simulations (Hinson and Wilson, 2004). The temperature changes between the morning and afternoon can cause a thermal tide that affect the pressure and winds (Lee et al., 2009). The middle atmosphere high probability between 15-30 km in the afternoon could be evident of this thermal tide.

To verify our altitude probabilities, observational data from the Mars Climate Sounder (MCS) onboard Mars Reconnaissance Orbiter (MRO) is used. Limb measurements using MCS characterizes the altitude above geographical features to measure the ice and water extinction. This allows clouds to be viewed from 10 km to the upper atmosphere. Using this method hinders being able to validate the model for altitudes below 10 km. Water-ice extinction from MCS matched the high probable altitudes seen during the ACB season between 10-35 kms. High altitude clouds are more frequently seen by MCS during the ACB season. During the dusty season, small amounts of ice-extinction is measured indicating low probabilities of clouds. This eliminates L_s 210° high probabilities seen between 20-40 kms which is not seen by MCS.

Promising results are seen in the analysis of cloud heights calculated from shadows seen in a Cloud Height Movie (CHM) pointed towards Aeolis Mons in the afternoon. Shadows moving across the mountain in Gale crater allows an absolute velocity to be calculated from geo-referencing. With a ZM paired with a CHM, the same analysis done in this work can be applied to calculate angular wind velocity. The absolute and angular

velocities are compared to determine the altitude of clouds at that particular time of sol and season. With 6 pairs, altitudes calculated ranged, but showed no clouds below the PBL at 10 km. Collecting more CHMs during the ACB season will increase confidence in results.

Moving forward, this analysis will continue as more ZMs with clouds are discovered throughout the continued mission. Advocating for CHMs, especially during the ACB season, will allow the altitude to be determined without an atmospheric model. MRAMS is tested by using both CHMs and MCS profiles to compare to contour probability plots that quantify the altitude of clouds through direct measurements. This makes CHMs valuable and should be analyzed further to reduce error in results. The majority of probability results from MRAMS match up with expected diurnal and seasonal observational and simulated results (Tamppari et al., 2003), (Smith, 2004), (Hinson and Wilson, 2004), (Kloos et al., 2016; 2018).

Several aspects of the results found using an atmospheric model help point towards reasonable results. The model, MRAMS, is a well cited model and has been used for landing assessments for Phoenix (Michaels and Rafkin, 2008), MSL (Vasavada et al., 2012) and Mars 2020 (Pla-García and Rafkin, 2015). MRAMS is coupled to the Ames Mars GCM, which is another respected model in the planetary science community. The results predicted in this research shows high probabilities for altitudes that are expected. The crater rim and PBL are examples where clouds are expected and where these results predict. The diurnal plots showing high clouds in the morning could be due to colder atmospheric temperatures, while the lower altitude clouds in the afternoon are from dust becoming CCN as they are kicked into the atmosphere midsol. These results are explainable based on current Martian atmospheric knowledge, however, by expanding the cadence of CHMs during aphelion season, we will be able to pinpont the altitude of clouds above Gale crater.

The results in this work are significant to the scientific community as it allows a more in depth look into the behaviour of water throughout a Martian Year. High probabilities exist in the middle atmosphere during the ACB season, which may be analogous to thermal tides. The clouds may also be associated with lower altitudes at the PBL or crater rim which could indicate crater circulation causing clouds. These results compared to the CHMs are highly useful and provides the best answer to the altitude of Martian clouds above Gale crater.

5 Future Work

The altitude of clouds on Mars can be estimated through correlation between observational and modelled values. This work can be improved by advocating for more atmospheric movies, especially during the morning and outside the ACB, and further analysis into Cloud Height Movies (CHMs) that observe shadows moving across Aeolis Mons. Clouds on Mars are not solely at Gale crater, where observations from different landing sites can aid in finding any geological patterns to cloud formation and altitudes across Mars.

An important addition to this work is adding more data from atmospheric movies taken at Gale crater, including CHMs during the Aphelion season. Atmospheric movies will continue to be taken every 2-3 sols according to cadence while Curiosity remains operational. By advocating for ZMs during the morning and outside the ACB will help fill in blanks in histograms. If any clouds are captured within the frames, they will attempted to be analyzed and added to the data set. Increasing our population, especially outside the ACB season, will help shape the contour plots to increase confidence in results. Once the ACB season starts again, ZM and CHM cadence will increase to take advantage of clouds being in the frames during this season.

A missing piece to the puzzle for this work is evaluating the altitude of clouds between the ± 2.5 hours from local noon constraint from the ZMs. SHMs do not have this constraint because of their lower elevation and do capture clouds within this constraint. By understanding how to incorporate SHMS into this work would prove valuable for studying diurnal changes.

To better study clouds on Mars, a lidar on any future missions would be very useful. Just this one instrument would be able to determine cloud altitude without correlating values with an atmospheric model. With an altitude found through lidar and atmospheric movies, an atmospheric model can be used to test

the reliability of the model, including any microphysics. The MRAMS simulation used in this study did not incorporate any microphysics due to the high uncertainties. The exploration of Mars is still ongoing, where questions still need to be answered including how dust and water vapour interact in the Martian atmosphere. Terrestrial models still struggle with this for Earth even though the atmospheric data set is easier to access compared to Mars. Therefore, any ways we can to try to improve Martian atmospheric models is useful.

To verify our method of estimating altitude with ZMs, we can use Phoenix data with the same observation. If a lidar measurement accompanied this atmospheric movie, it could provide the exact altitude of clouds overhead. Even without a direct lidar measurement, clouds were previously observed within the PBL (Whiteway et al., 2009), which could be used to test model results. If MRAMS could be used to model conditions at Green Valley, the comparison to Phoenix lidar measurements could help verify MRAMS results. Other methods of verifying altitude through our procedure is testing with known Terrestrial cloud data. Using the lidar on York University campus, an experiment could be set up to take an ZM and lidar measurement simultaneously to measure the accuracy of our procedure with ZMs taken by MSL.

Curiosity is not the only spacecraft to be on the Martian surface collecting scientific data. Besides Phoenix, Opportunity both used atmospheric images to classify the atmosphere, including cloud activity. These data sets can be used to aid our understanding on Martian water-ice clouds by evaluating differences between landing sites. By assessing how clouds are in different regions across Mars, patterns could develop describing cloud formation in a MY and geographical location. With Insight and Mars 2020 upcoming, these surface spacecraft can also help develop the current timeline of clouds in the Martian atmosphere. The landing site for Mars 2020 is not definite, but could provide another location on Mars to analyze cloud activity. Insight is planned to land on Mars before the end of 2018, at a location just north of Gale Crater. This location provides an opportunity to understand circulation and cloud activity from outside the crater. The hypothesis of a dry crater would mean that clouds seen at Gale Crater most likely come from outside the crater as low water content in the crater would inhibit cloud formation. By viewing cloud activity near the crater, we can assess if this hypothesis is correct.

Bibliography

Bell, J. F., Squyres, S. W., Herkenhoff, K. E., Maki, J. N., Arneson, H. M., Brown, D., Collins, S. A., Dingizian, A., Elliot, S. T., Hagerott, E. C., Hayes, A. G., Johnson, M. J., Johnson, J. R., Joseph, J., Kinch, K., Lemmon, M. T., Morris, R. V., Scherr, L., Schwochert, M., Shepard, M. K., Smith, G. H., Sohl-Dickstein, J. N., Sullivan, R. J., Sullivan, W. T., and Wadsworth, M. (2003). Mars Exploration Rover Athena Panoramic Camera (Pancam) investigation. *Journal of Geophysical Research (Planets)*, 108:8063.

Benson, J. L., Bonev, B. P., James, P. B., Shan, K. J., Cantor, B. A., and Caplinger, M. A. (2003). The seasonal behavior of water ice clouds in the Tharsis and Valles Marineris regions of Mars: Mars Orbiter Camera Observations. *Icarus* , 165:34–52.

Christensen, P. R., Mehall, G. L., Silverman, S. H., Anwar, S., Cannon, G., Gorelick, N., Kheen, R., Tourville, T., Bates, D., Ferry, S., Fortuna, T., Jeffryes, J., O'Donnell, W., Peralta, R., Wolverton, T., Blaney, D., Denise, R., Rademacher, J., Morris, R. V., and Squyres, S. (2003). Miniature Thermal Emission Spectrometer for the Mars Exploration Rovers. *Journal of Geophysical Research (Planets)*, 108:8064.

Clancy, R. T., Grossman, A. W., Wolff, M. J., James, P. B., Rudy, D. J., Billawala, Y. N., Sandor, B. J., Lee, S. W., and Muhleman, D. O. (1996). Water Vapor Saturation at Low Altitudes around Mars Aphelion: A Key to Mars Climate? *Icarus* , 122:36–62.

Clancy, R. T., Sandor, B. J., Wolff, M. J., Christensen, P. R., Smith, M. D., Pearl, J. C., Conrath, B. J., and Wilson, R. J. (2000). An intercomparison of ground-based millimeter, MGS TES, and Viking atmospheric

temperature measurements: Seasonal and interannual variability of temperatures and dust loading in the global Mars atmosphere. *Journal of Geophysical Research*, 105:9553–9572.

Colaprete, A., Toon, O. B., and Magalhães, J. A. (1999). Cloud formation under Mars Pathfinder conditions. *Journal of Geophysical Research*, 104:9043–9054.

Conrath, B. J., Pearl, J. C., Smith, M. D., Maguire, W. C., Christensen, P. R., Dason, S., and Kaelberer, M. S. (2000). Mars Global Surveyor Thermal Emission Spectrometer (TES) observations: Atmospheric temperatures during aerobraking and science phasing. *Journal of Geophysical Research*, 105:9509–9520.

Dickinson, C., Whiteway, J. A., Komguem, L., Moores, J. E., and Lemmon, M. T. (2010). Lidar measurements of clouds in the planetary boundary layer on Mars. *Geophysical Research Letters*, 37:L18203.

Elandt, R. C. (1961). The Folded Normal Distribution: Two Methods of Estimating Parameters from Moments. *Technometrics*, 3:L18203.

Forget, F., Hourdin, F., Fournier, R., Hourdin, C., Talagrand, O., Collins, M., Lewis, S. R., Read, P. L., and Huot, J.-P. (1999). Improved general circulation models of the Martian atmosphere from the surface to above 80 km. *Journal of Geophysical Research*, 104:24155–24176.

Forget, F., Millour, E., Madeleine, J. B., Colaitis, A., Spiga, A., Montabone, L., Hourdin, F., Lefèvre, F., Montmessin, F., Gonzalez-Galindo, F., Lopez-Valverde, M. A., Lewis, S. R., Read, P. R., and Mulholland, D. (2011). Back to The Basics: Improving the Prediction of Temperature, Pressure and Winds in the LMD General Circulation Model. In *Mars Atmosphere: Modelling and observation*, pages 64–67.

Francis, R., Moores, J., McIsaac, K., Choi, D., and Osinski, G. (2014). Observations of wind direction by automated analysis of images from Mars and the MSL rover. *Acta Astronautica*, 94:776–783.

Golombek, M. P., Bridges, N. T., Moore, H. J., Murchie, S. L., Murphy, J. R., Parker, T. J., Rieder, R., Rivellini, T. P., Schofield, J. T., Seiff, A., Singer, R. B., Smith, P. H., Soderblom, L. A., Spencer, D. A., Stoker, C. R., Sullivan, R., Thomas, N., Thurman, S. W., Tomasko, M. G., Vaughan, R. M., Wänke,

H., Ward, A. W., and Wilson, G. R. (1999). Overview of the Mars Pathfinder Mission: Launch through landing, surface operations, data sets, and science results. *Journal of Geophysical Research*, 104:8523–8554.

Grotzinger, J. P., Crisp, J., Vasavada, A. R., Anderson, R. C., Baker, C. J., Barry, R., Blake, D. F., Conrad, P., Edgett, K. S., Ferdowski, B., Gellert, R., Gilbert, J. B., Golombek, M., Gómez-Elvira, J., Hassler, D. M., Jandura, L., Litvak, M., Mahaffy, P., Maki, J., Meyer, M., Malin, M. C., Mitrofanov, I., Simmonds, J. J., Vaniman, D., Welch, R. V., and Wiens, R. C. (2012). Mars Science Laboratory Mission and Science Investigation. *Space Sci. Rev.* , 170:5–56.

Guzewich, S. D., Newman, C. E., Smith, M. D., Moores, J. E., Smith, C. L., Moore, C., Richardson, M. I., Kass, D., Kleinböhl, A., Mischna, M., Martín-Torres, F. J., Zorzano- Mier, M. P., and Battalio, M. (2017). The Vertical Dust Profile Over Gale Crater, Mars. *Journal of Geophysical Research (Planets)*, 122:2779–2792.

Haberle, R. M. (1986). The climate of Mars. *Scientific American*, 254:54–62.

Haberle, R. M., Barnes, J. R., Murphy, J. R., Joshi, M. M., and Schaeffer, J. (1997). Meteorological predictions for the Mars Pathfinder lander. *Journal of Geophysical Research*, 102:13301–13312.

Haberle, R. M., Gómez-Elvira, J., Torre Juárez, M., Harri, A.-M., Hollingsworth, J. L., Kahanpää, H., Kahre, M. A., Lemmon, M., Martín-Torres, F. J., Mischna, M., Moores, J. E., Newman, C., Rafkin, S. C. R., Rennó, N., Richardson, M. I., Rodríguez-Manfredi, J. A., Vasavada, A. R., and Zorzano-Mier, M.-P. (2014). Preliminary interpretation of the REMS pressure data from the first 100 sols of the MSL mission. *Journal of Geophysical Research (Planets)*, 119:440–453.

Haberle, R. M., Hollingsworth, J. L., Colaprete, A., Bridger, A., McKay, C., Murphy, J., and Freedman, R. (2003). The NASA/Ames Mars General Circulation Model: Model Improvements and Comparison with Observations.

Haberle, R. M., Pollack, J. B., Barnes, J. R., Zurek, R. W., Leovy, C. B., Murphy, J. R., Lee, H., and Schaeffer, J. (1993). Mars atmospheric dynamics as simulated by the NASA Ames General Circulation Model. 1. The zonal-mean circulation. *Journal of Geophysical Research*, 98:3093–3123.

Heavens, N. G., Benson, J. L., Kass, D. M., Kleinböhl, A., Abdou, W. A., McCleese, D. J., Richardson, M. I., Schofield, J. T., Shirley, J. H., and Wolkenberg, P. M. (2010). Water ice clouds over the Martian tropics during northern summer. *Geophysical Research Letters*, 37:L18202.

Heavens, N. G., McCleese, D. J., Richardson, M. I., Kass, D. M., Kleinböhl, A., and Schofield, J. T. (2011). Structure and dynamics of the Martian lower and middle atmosphere as observed by the Mars Climate Sounder: 2. Implications of the thermal structure and aerosol distributions for the mean meridional circulation. *Journal of Geophysical Research (Planets)*, 116:E01010.

Hess, S. L. (1976). The Vertical Distribution of Water Vapor in the Atmosphere of Mars. *Icarus* , 28:269–278.

Hinson, D. P. and Wilson, R. J. (2004). Temperature inversions, thermal tides, and water ice clouds in the Martian tropics. *Journal of Geophysical Research (Planets)*, 109:E01002.

Jakosky, B. M. and Farmer, C. B. (1982). The seasonal and global behavior of water vapor in the Mars atmosphere - Complete global results of the Viking atmospheric water detector experiment. *J. Geophys. Res.* , 87:2999–3019.

Jakosky, B. M. and Haberle, R. M. (1992). *The seasonal behavior of water on Mars*, pages 969–1016.

Kahre, M. A., Haberle, R. M., Hollingsworth, J. L., Montmessin, F., Brecht, A. S., Urata, R., Klassen, D. R., and Wolff, M. J. (2017). Updates on Modeling the Water Cycle with the NASA Ames Mars Global Climate Model. In *The Mars Atmosphere: Modelling and observation*, page 3209.

Kleinböhl, A., Friedson, A. J., and Schofield, J. T. (2017). Two-dimensional radiative transfer for the retrieval of limb emission measurements in the martian atmosphere. *Journal of Quantitative Spectroscopy and Radiative Transfer*, 187:511–522.

Kloos, J. L., Moores, J. E., Lemmon, M., Kass, D., Francis, R., de la Torre Juárez, M., Zorzano, M.-P., and Martín-Torres, F. J. (2016). The first Martian year of cloud activity from Mars Science Laboratory (sol 0-800). *Advances in Space Research*, 57:1223–1240.

Kloos, J. L., Moores, J. E., Whiteway, J. A., and Aggarwal, M. (2018). Interannual and Diurnal Variability in Water Ice Clouds Observed from MSL Over Two Martian Years. *Journal of Geophysical Research (Planets)*, 123:233–245.

Laboratoire de Meteorologie Dynamique (2008). Martian Seasons and Solar Longitude. Available at: http://www-mars.lmd.jussieu.fr/mars/time/solar_longitude.html.

Lee, C., Lawson, W. G., Richardson, M. I., Heavens, N. G., Kleinböhl, A., Banfield, D., McCleese, D. J., Zurek, R., Kass, D., Schofield, J. T., Leovy, C. B., Taylor, F. W., and Toigo, A. D. (2009). Thermal tides in the Martian middle atmosphere as seen by the Mars Climate Sounder. *Journal of Geophysical Research (Planets)*, 114:E03005.

Lemmon, M. (2018). Clouds, Sunrises and Sunsets on Mars - Mars Pathfinder. Available at: https://mars.nasa.gov/MPF/science/clouds.html.

Lemmon, M. T., Wolff, M. J., Bell, III, J. F., Smith, M. D., Cantor, B. A., and Smith, P. H. (2015). Dust aerosol, clouds, and the atmospheric optical depth record over 5 Mars years of the Mars Exploration Rover mission. *Icarus* , 251:96–111.

Lemmon, M. T., Wolff, M. J., Smith, M. D., Clancy, R. T., Banfield, D., Landis, G. A., Ghosh, A., Smith, P. H., Spanovich, N., Whitney, B., Whelley, P., Greeley, R., Thompson, S., Bell, J. F., and Squyres, S. W. (2004). Atmospheric Imaging Results from the Mars Exploration Rovers: Spirit and Opportunity. *Science*, 306:1753–1756.

Leone, F. C., Nelson, L. S., and Nottingham, R. B. (1961). The Folded Normal Distribution. *Technometrics*, 3:L18203.

Madeleine, J. B., Forget, F., Millour, E., Navarro, T., and Spiga, A. (2012). The influence of radiatively active water ice clouds on the Martian climate. *Geophysical Research Letters*, 39:L23202.

Maki, J. N., Bell, J. F., Herkenhoff, K. E., Squyres, S. W., Kiely, A., Klimesh, M., Schwochert, M., Litwin, T., Willson, R., Johnson, A., Maimone, M., Baumgartner, E., Collins, A., Wadsworth, M., Elliot, S. T., Dingizian, A., Brown, D., Hagerott, E. C., Scherr, L., Deen, R., Alexander, D., and Lorre, J. (2003). Mars Exploration Rover Engineering Cameras. *Journal of Geophysical Research (Planets)*, 108:8071.

Maki, J. N., Thiessen, D., Pourangi, A., Kobzeff, P., Scherr, L., Elliott, T., Dingizian, A., and St. Ange, B. (2011). The Mars Science Laboratory (MSL) Navigation Cameras (Navcams). In *Lunar and Planetary Science Conference*, volume 42, page 2738.

Maltagliati, L., Montmessin, F., Fedorova, A., Korablev, O., Forget, F., and Bertaux, J. L. (2011). Evidence of Water Vapor in Excess of Saturation in the Atmosphere of Mars. *Science*, 333:1868.

Martínez, G. M., Newman, C. N., De Vicente-Retortillo, A., Fischer, E., Renno, N. O., Richardson, M. I., Fairén, A. G., Genzer, M., Guzewich, S. D., Haberle, R. M., Harri, A. M., Kemppinen, O., Lemmon, M. T., Smith, M. D., de la Torre-Juárez, M., and Vasavada, A. R. (2017). The Modern Near-Surface Martian Climate: A Review of In-situ Meteorological Data from Viking to Curiosity. *Space Sci. Rev.* , 212:295–338.

McCleese, D. J., Schofield, J. T., Taylor, F. W., Calcutt, S. B., Foote, M. C., Kass, D. M., Leovy, C. B., Paige, D. A., Read, P. L., and Zurek, R. W. (2007). Mars Climate Sounder: An investigation of thermal and water vapor structure, dust and condensate distributions in the atmosphere, and energy balance of the polar regions. *Journal of Geophysical Research (Planets)*, 112:E05S06.

Michaels, T. I., Colaprete, A., and Rafkin, S. C. R. (2006). Significant vertical water transport by mountain-induced circulations on Mars. *Geophysical Research Letters*, 33:L16201.

Michaels, T. I. and Rafkin, S. C. R. (2008). Meteorological predictions for candidate 2007 Phoenix Mars

Lander sites using the Mars Regional Atmospheric Modeling System (MRAMS). *Journal of Geophysical Research (Planets)*, 113:E00A07.

Michelangeli, D. V., Toon, O. B., Haberle, R. M., and Pollack, J. B. (1993). Numerical Simulations of the Formation and Evolution of Water Ice Clouds in the Martian Atmosphere. *Icarus* , 102:261–285.

Montmessin, F., Forget, F., Rannou, P., Cabane, M., and Haberle, R. M. (2004). Origin and role of water ice clouds in the Martian water cycle as inferred from a general circulation model. *Journal of Geophysical Research (Planets)*, 109:E10004.

Moore, C. A., Moores, J. E., Lemmon, M. T., Rafkin, S. C. R., Francis, R., Pla- García, J., Haberle, R. M., Zorzano, M.-P., Martín-Torres, F. J., and Burton, J. R. (2016). A full martian year of line-of-sight extinction within Gale Crater, Mars as acquired by the MSL Navcam through sol 900. *Icarus* , 264:102–108.

Moores, J. E., Lemmon, M. T., Kahanpää, H., Rafkin, S. C. R., Francis, R., Pla- Garcia, J., Bean, K., Haberle, R., Newman, C., Mischna, M., Vasavada, A. R., de la Torre Juárez, M., Rennó, N., Bell, J., Calef, F., Cantor, B., Mcconnochie, T. H., Harri, A.-M., Genzer, M., Wong, M. H., Smith, M. D., Martín-Torres, F. J., Zorzano, M.-P., Kemppinen, O., and McCullough, E. (2015a). Observational evidence of a suppressed planetary boundary layer in northern Gale Crater, Mars as seen by the Navcam instrument onboard the Mars Science Laboratory rover. *Icarus* , 249:129–142.

Moores, J. E., Lemmon, M. T., Rafkin, S. C. R., Francis, R., Pla-Garcia, J., de la Torre Juárez, M., Bean, K., Kass, D., Haberle, R., Newman, C., Mischna, M., Vasavada, A., Rennó, N., Bell, J., Calef, F., Cantor, B., Mcconnochie, T. H., Harri, A.-M., Genzer, M., Wong, M., Smith, M. D., Javier Martín-Torres, F., Zorzano, M.-P., Kemppinen, O., and McCullough, E. (2015b). Atmospheric movies acquired at the Mars Science Laboratory landing site: Cloud morphology, frequency and significance to the Gale Crater water cycle and Phoenix mission results. *Advances in Space Research*, 55:2217–2238.

Moores, J. E., Lemmon, M. T., Smith, P. H., Komguem, L., and Whiteway, J. A. (2010). Atmospheric

dynamics at the Phoenix landing site as seen by the Surface Stereo Imager. *Journal of Geophysical Research (Planets)*, 115:E00E08.

NASA/JPL-Caltech (2004). Clouds over 'Endurance' on Sol 290. Available at: https://mars.nasa.gov/mer/gallery/press/opportunity/20041213a.html.

Navarro, T., Madeleine, J. B., Forget, F., Spiga, A., Millour, E., Montmessin, F., and Määttänen, A. (2014). Global climate modeling of the Martian water cycle with improved microphysics and radiatively active water ice clouds. *Journal of Geophysical Research (Planets)*, 119:1479–1495.

Paige, D. A. and Wood, S. E. (1992). Modeling the Martian seasonal CO2 cycle 2. Interannual variability. *Icarus* , 99:15–27.

Peale, S. J. (1973). Water and the Martian W Cloud. *Icarus* , 18:497–501.

Pearl, J. C., Smith, M. D., Conrath, B. J., Bandfield, J. L., and Christensen, P. R. (2001). Observations of Martian ice clouds by the Mars Global Surveyor Thermal Emission Spectrometer: The first Martian year. *J. Geophys. Res.* , 106:12325–12338.

Pla-García, J. and Rafkin, S. C. R. (2015). Meteorological predictions for Mars 2020 Exploration Rover high-priority landing sites throug MRAMS Mesoscale Modeling. In *EGU General Assembly Conference Abstracts*, volume 17, page 12605.

Pla-Garcia, J., Rafkin, S. C. R., Kahre, M., Gomez-Elvira, J., Hamilton, V. E., Navarro, S., Torres, J., Marín, M., and Vasavada, A. R. (2016). The meteorology of Gale crater as determined from rover environmental monitoring station observations and numerical modeling. Part I: Comparison of model simulations with observations. *Icarus* , 280:103–113.

Pollack, J. B., Haberle, R. M., Murphy, J. R., Schaeffer, J., and Lee, H. (1993). Simulations of the general circulation of the Martian atmosphere. 2. Seasonal pressure variations. *Journal of Geophysical Research*, 98:3149–3181.

Pollack, J. B., Haberle, R. M., Schaeffer, J., and Lee, H. (1990). Simulations of the general circulation of the Martian atmosphere. 1. Polar processes. *Journal of Geophysical Research*, 95:1447–1473.

Rafkin, S. C. R., Haberle, R. M., and Michaels, T. I. (2001). The Mars Regional Atmospheric Modeling System: Model Description and Selected Simulations. *Icarus* , 151:228–256.

Richardson, M. I. and Wilson, R. J. (2002). Investigation of the nature and stability of the Martian seasonal water cycle with a general circulation model. *Journal of Geophysical Research (Planets)*, 107:5031.

Sagan, C., Veverka, J., and Gierasch, P. (1971). Observational Consequences of Martian Wind Regimes. *Icarus* , 15:253–278.

Schofield, J. T., Barnes, J. R., Crisp, D., Haberle, R. M., Larsen, S., Magalhaes, J. A., Murphy, J. R., Seiff, A., and Wilson, G. (1997). The Mars Pathfinder Atmospheric Structure Investigation/Meteorology. *Science*, 278:1752.

Smith, M. D. (2004). Interannual variability in TES atmospheric observations of Mars during 1999-2003. *Icarus* , 167:148–165.

Smith, M. D., Bougher, S. W., Encrenaz, T., Forget, F., and Kleinböhl, A. (2017). *Thermal Structure and Composition*, pages 20–41.

Smith, M. D., Wolff, M. J., Spanovich, N., Ghosh, A., Banfield, D., Christensen, P. R., Landis, G. A., and Squyres, S. W. (2006). One Martian year of atmospheric observations using MER Mini-TES. *Journal of Geophysical Research (Planets)*, 111:E12S13.

Smith, P. H., Bell, J. F., I., Bridges, N. T., Britt, D. T., Gaddis, L., Greeley, R., Keller, H. U., Herkenhoff, K. E., Jaumann, R., Johnson, J. R., Kirk, R. L., Lemmon, M., Maki, J. N., Malin, M. C., Murchie, S. L., Oberst, J., Parker, T. J., Reid, R. J., Sablotny, R., Soderblom, L. A., Stoker, C., Sullivan, R., Thomas, N., Tomasko, M. G., Ward, W., and Wegryn, E. (1997). Results from the Mars Pathfinder Camera. *Science*, 278:1758.

Smith, P. H., Tamppari, L., Arvidson, R. E., Bass, D., Blaney, D., Boynton, W., Carswell, A., Catling, D., Clark, B., Duck, T., DeJong, E., Fisher, D., Goetz, W., Gunnlaugsson, P., Hecht, M., Hipkin, V., Hoffman, J., Hviid, S., Keller, H., Kounaves, S., Lange, C. F., Lemmon, M., Madsen, M., Malin, M., Markiewicz, W., Marshall, J., McKay, C., Mellon, M., Michelangeli, D., Ming, D., Morris, R., Renno, N., Pike, W. T., Staufer, U., Stoker, C., Taylor, P., Whiteway, J., Young, S., and Zent, A. (2008). Introduction to special section on the Phoenix Mission: Landing Site Characterization Experiments, Mission Overviews, and Expected Science. *Journal of Geophysical Research (Planets)*, 113:E00A18.

Smith, P. H., Tamppari, L. K., Arvidson, R. E., Bass, D., Blaney, D., Boynton, W. V., Carswell, A., Catling, D. C., Clark, B. C., Duck, T., DeJong, E., Fisher, D., Goetz, W., Gunnlaugsson, H. P., Hecht, M. H., Hipkin, V., Hoffman, J., Hviid, S. F., Keller, H. U., Kounaves, S. P., Lange, C. F., Lemmon, M. T., Madsen, M. B., Markiewicz, W. J., Marshall, J., McKay, C. P., Mellon, M. T., Ming, D. W., Morris, R. V., Pike, W. T., Renno, N., Staufer, U., Stoker, C., Taylor, P., Whiteway, J. A., and Zent, A. P. (2009). H_2O at the Phoenix Landing Site. *Science*, 325:58.

Smith, S. A. and Smith, B. A. (1972). Diurnal and seasonal behavior of discrete white clouds on Mars. *Icarus* , 16:509–521.

Squyres, S. W., Arvidson, R. E., Baumgartner, E. T., Bell, J. F., Christensen, P. R., Gorevan, S., Herkenhoff, K. E., Klingelhöfer, G., Madsen, M. B., Morris, R. V., Rieder, R., and Romero, R. A. (2003). Athena Mars rover science investigation. *Journal of Geophysical Research (Planets)*, 108:8062.

Tamppari, L. K., Zurek, R. W., and Paige, D. A. (2003). Viking-era diurnal water-ice clouds. *Journal of Geophysical Research (Planets)*, 108:5073.

Tanaka, K. L., Scott, D. H., and Greeley, R. (1992). *Global stratigraphy.*, pages 345–382.

Tellmann, S., PäTzold, M., HäUsler, B., Hinson, D. P., and Tyler, G. L. (2013). The structure of Mars lower atmosphere from Mars Express Radio Science (MaRS) occultation measurements. *Journal of Geophysical Research (Planets)*, 118:306–320.

Toigo, A. D. and Richardson, M. I. (2003). Meteorology of proposed Mars Exploration Rover landing sites. *Journal of Geophysical Research (Planets)*, 108:8092.

Toon, O. B., Turco, R. P., Westphal, D., Malone, R., and Liu, M. S. (1988). A multidimensional model for aerosols - Description of computational analogs. *Journal of Atmospheric Sciences*, 45:2123–2143.

Tsagris, M., Beneki, C., and Hassani, H. (2014). On the Folded Normal Distribution. *Mathematics*, 2:L18203.

Tyler, D., J. and Barnes, J. R. (2013). Mesoscale Modeling of the Circulation in the Gale Crater Region: An Investigation into the Complex Forcing of Convective Boundary Layer Depths. *International Journal of Mars Science and Exploration*, 8:58–77.

Vasavada, A. R. (2018). MSL Science Corner - Science Goals. Available at: https://msl-scicorner.jpl.nasa.gov/ScienceGoals/.

Vasavada, A. R., Chen, A., Barnes, J. R., Burkhart, P. D., Cantor, B. A., Dwyer- Cianciolo, A. M., Fergason, R. L., Hinson, D. P., Justh, H. L., Kass, D. M., Lewis, S. R., Mischna, M. A., Murphy, J. R., Rafkin, S. C. R., Tyler, D., and Withers, P. G. (2012). Assessment of Environments for Mars Science Laboratory Entry, Descent, and Surface Operations. *Space Sci. Rev.* , 170:793–835.

Wang, H. and Ingersoll, A. P. (2002). Martian clouds observed by Mars Global Surveyor Mars Orbiter Camera. *Journal of Geophysical Research (Planets)*, 107:5078.

Whiteway, J., Daly, M., Carswell, A., Duck, T., Dickinson, C., Komguem, L., and Cook, C. (2008). Lidar on the Phoenix mission to Mars. *Journal of Geophysical Research (Planets)*, 113:E00A08.

Whiteway, J. A., Komguem, L., Dickinson, C., Cook, C., Illnicki, M., Seabrook, J., Popovici, V., Duck, T. J., Davy, R., Taylor, P. A., Pathak, J., Fisher, D., Carswell, A. I., Daly, M., Hipkin, V., Zent, A. P., Hecht, M. H., Wood, S. E., Tamppari, L. K., Renno, N., Moores, J. E., Lemmon, M. T., Daerden, F., and Smith, P. H. (2009). Mars Water-Ice Clouds and Precipitation. *Science*, 325:68.

Williams, D. R. (2016). Mars fact sheet - mars and earth comparison. Available at: https://nssdc.gsfc.nasa.gov/planetary/factsheet/marsfact.html.

Withers, P. and Smith, M. D. (2006). Atmospheric entry profiles from the Mars Exploration Rovers Spirit and Opportunity. *Icarus* , 185:133–142.

Wolff, M. J., James, P. B., Todd Clancy, R., and Lee, S. W. (1999). Hubble Space Telescope observations of the Martian aphelion cloud belt prior to the Pathfinder mission: Seasonal and interannual variations. *J. Geophys. Res.* , 104:9027–9042.

Wolff, M. J., Smith, M. D., Clancy, R. T., Spanovich, N., Whitney, B. A., Lemmon, M. T., Bandfield, J. L., Banfield, D., Ghosh, A., Landis, G., Christensen, P. R., Bell, J. F., and Squyres, S. W. (2006). Constraints on dust aerosols from the Mars Exploration Rovers using MGS overflights and Mini-TES. *Journal of Geophysical Research (Planets)*, 111:E12S17.

Zurek, R. W. (1992). *Comparative aspects of the climate of Mars: an introduction to the current atmosphere.*, pages 799–817.

Appendix A: ZM Values per Season

Table 1: ZM Values for L_s 0°.

L_s	**Sol**	**Time (LTST)**	**Angular Distance**	**Meteorological Wind Direction**
6.80°	363	17:41	6.32°	285°
7.47°	1033	15:17	3.62°	10°
9.71°	1706	17:03	8.96°	260°

Table 2: ZM Values for L_s 30°.

L_s	**Sol**	**Time (LTST)**	**Angular Distance**	**Meteorological Wind Direction**
16.59°	1720	16:17	5.56°	244°
27.62°	1743	15:02	3.54°	49°
34.51°	1758	06:46	6.69°	66°
38.49°	429	16:29	6.15°	89°
44.91°	443	15:17	5.29°	265°

Table 3: ZM Values for L_s 60°.

L_s	**Sol**	**Time (LTST)**	**Angular Distance**	**Meteorological Wind Direction**
45.58°	1113	16:04	10.25°	232°
45.75°	1782	15:01	7.69°	300°
48.05°	1787	15:39	6.72°	288°
50.62°	1124	17:28	6.82°	255°
52.92°	1798	08:28	7.09°	81°
56.78°	1138	08:58	9.47°	22°
59.65°	1813	07:08	12.60°	37°
61.92°	1818	08:11	8.10°	49°
63.05°	1152	07:04	11.83°	234°
63.85°	1822	15:06	10.30°	100°
65.08°	1825	09:13	9.00°	40°
68.14°	1163	14:45	9.65°	122°
72.46°	504	16:22	7.67°	79°
72.68°	1842	07:57	14.60°	213°
73.70°	1844	14:07	7.55°	80°
73.80°	507	15:51	4.91°	95°

Table 4: ZM Values for L_s 90°.

L_s	**Sol**	**Time (LTST)**	**Angular Distance**	**Meteorological Wind Direction**
75.81°	1849	07:17	12.09°	65°
76.23°	1181	15:57	9.18°	107°
76.50°	513	14:57	5.35°	78°
79.89°	1858	09:16	9.91°	74°
80.27°	1190	15:40	14.60°	74°
81.62°	1193	15:43	10.26°	79°
81.80°	1862	15:33	8.83°	87°
81.91°	525	15:27	8.10°	140°
83.21°	528	15:36	7.46°	136°
83.62°	1866	16:30	11.56°	79°
89.01°	1878	14:32	15.35°	73°
89.12°	541	16:26	6.21°	134°
89.61°	1211	08:22	9.67°	264°
89.96°	1880	17:08	11.02°	85°
91.57°	1215	16:15	10.02°	127°
91.86°	1216	07:29	11.82°	319°
93.22°	550	16:10	5.12°	150°
94.49°	1890	16:06	8.40°	52°
94.64°	1222	10:16	14.63°	32°
94.94°	1891	15:59	8.40°	85°
96.32°	1894	16:23	15.04°	83°
97.21°	1896	15:05	7.15°	50°
98.22°	561	15:24	14.10°	121°
98.66°	562	14:51	5.59°	135°
98.88°	1900	06:23	19.78°	232°
100.54°	1235	07:22	11.43°	93°

Table 5: ZM Values for L_s 120°.

L_s	**Sol**	**Time (LTST)**	**Angular Distance**	**Meteorological Wind Direction**
105.38°	1914	08:12	9.24°	244°
105.51°	1914	15:09	10.29°	71°
105.65°	1246	08:24	10.99°	122°
106.29°	1916	07:13	10.25°	243°
106.46°	1916	16:14	12.15°	77°
107.25°	1918	08:44	8.96°	244°
107.39°	1918	15:50	10.02°	110°
108.17°	1920	08:17	10.69°	258°
108.33°	1920	16:17	15.84°	84°
110.02°	1924	06:49	13.45°	231°
111.25°	1258	07:46	12.43°	353°
113.03°	1930	16:27	11.90°	87°
113.10°	593	16:26	4.59°	108°
116.21°	1937	09:17	7.56°	44°
117.28°	1939	15:22	13.19°	89°
117.84°	603	15:44	4.33°	342°
121.74°	1278	08:29	7.77°	228°
122.09°	1949	15:35	11.26°	42°
122.17°	612	16:07	4.33°	200°
124.03°	1953	15:57	18.90°	67°
125.81°	1957	07:43	9.14°	235°
126.93°	1959	14:31	10.56°	93°
127.30°	1960	08:51	8.66°	26°
127.56°	1292	07:20	8.49°	293°
130.99°	630	14:39	5.78°	100°
132.53°	1302	08:46	10.99°	307°
132.68°	1302	16:16	9.51°	125°
132.70°	1971	07:03	9.40°	310°
134.52°	1306	08:20	11.01°	332°
134.52°	1306	08:20	9.77°	79°

Table 6: ZM Values for L_s 150°.

L_s	**Sol**	**Time (LTST)**	**Angular Distance**	**Meteorological Wind Direction**
135.22°	1976	07:47	9.05°	62°
135.41°	1976	17:08	9.05°	62°
136.17°	1309	15:22	9.83°	154°
137.42°	1980	16:53	12.24°	251°
137.55°	1312	09:21	6.21°	7°
137.72°	1981	07:08	7.09°	290°
138.56°	1314	08:50	5.35°	9°
142.31°	1990	07:14	9.27°	260°
142.48°	1990	15:20	15.84°	214°
143.52°	1992	15:54	7.92°	266°
144.89°	1326	17:38	11.20°	208°
145.94°	1997	08:05	4.39°	319°
146.66°	1998	17:23	10.02°	192°
147.77°	663	16:38	4.59°	167°
150.89°	669	15:21	3.17°	227°
151.44°	670	15:27	3.52°	271°
151.95°	671	15:06	3.17°	306°
152.76°	2010	07:43	1.81°	280°

Table 7: ZM Values for L_s 180°.

L_s	**Sol**	**Time (LTST)**	**Angular Distance**	**Meteorological Wind Direction**
165.71°	1365	15:16	2.81°	264 °
168.26°	701	15:44	3.35°	241°
168.89°	1371	08:30	5.32°	122°
176.24°	1384	08:13	4.85°	22°
185.53°	1400	08:16	6.86°	48°
193.24°	1413	07:42	2.20°	32°

Table 8: ZM Values for L_s 210°.

L_s	**Sol**	**Time (LTST)**	**Angular Distance**	**Meteorological Wind Direction**
198.30°	1421	16:17	4.54°	100°
205.50°	1433	09:32	8.00°	135°
209.83°	1440	08:43	8.21°	199°

Table 9: ZM Values for L_s 240°. No movies within this season had clouds with strong enough features to analyze.

L_s	**Sol**	**Time (LTST)**	**Angular Distance**	**Meteorological Wind Direction**

Table 10: ZM Values for L_s 270°.

L_s	**Sol**	**Time (LTST)**	**Angular Distance**	**Meteorological Wind Direction**
268.07°	193	09:25	10.12°	5°
271.30°	198	08:50	11.46°	4°
280.07°	880	17:11	8.83°	276°

Table 11: ZM Values for L_s 300°.

L_s	**Sol**	**Time (LTST)**	**Angular Distance**	**Meteorological Wind Direction**
286.40°	1559	06:36	21.26°	86°
287.50°	892	07:09	11.12°	247°
290.30°	1565	07:31	9.67°	90°
295.19°	904	15:40	7.47°	297°
299.57°	1580	07:01	10.69°	192°
307.90°	925	07:52	8.9°	297°
309.29°	927	16:01	7.48°	228°

Table 12: ZM Values for L_s 330°.

L_s	**Sol**	**Time (LTST)**	**Angular Distance**	**Meteorological Wind Direction**
339.00°	310	17:55	4.05°	328°